Deliverable 2.19: Model abstraction techniques for assessing the chemical evolution at the disposal cell scale and applications for sensitivity and uncertainty

Work Package 2

The project leading to this application has received funding from the European Union’s Horizon 2020 research and innovation programme under grant agreement No 847593.

http://www.ejp-eurad.eu/

Document information

Project Acronym	**EURAD**
Project Title	**European Joint Programme on Radioactive Waste Management**
Project Type	**European Joint Programme (EJP)**
EC grant agreement No.	**847593**
Project starting / end date	**1st June 2019 – 30 May 2024**
Work Package No.	**2**
Work Package Title	**Assessment of Chemical Evolution of ILW and HLW Disposal Cells**
Work Package Acronym	**ACED**
Deliverable No.	**2.19**
Deliverable Title	**Report on comparison of model abstraction results**
Lead Beneficiary	**UFZ**
Contractual Delivery Date	**1 February 2023**
Actual Delivery Date	**18 March 2024**
Type	**Report**
Dissemination level	**PU**
Authors	**Javier Samper (ENRESA- UDC), Alba Mon (UDC), Luis Montenegro (UDC), Laurent De Windt (Mines Paris), Joan Govaerts (SCK), Eric Laloy (SCK), Diederik Jacques (SCK), Dalia Grigaliuniene (LEI), Povilas Balcius (LEI), Povilas Poskas (LEI), Haibing Shao (UFZ), Falko Vehling (UFZ), Yushan Gu (VTT)**

To be cited as:

Samper, J., A. Mon, L. Montenegro, L. De Windt, J. Govaerts, E. Laloy, D. Jacques, D. Grigaliuniene, P. Balcius, P. Poskas, H. Shao, F. Vehling, Y. Gu (2024): Report on comparison of model abstraction results. Final version as of 18.03.2024 of deliverable D2.19 of the HORIZON 2020 project EURAD. EC Grant agreement no: 847593.)

Disclaimer

Acknowledgement

This document is a deliverable of the European Joint Programme on Radioactive Waste Management (EURAD). EURAD has received funding from the European Union's Horizon 2020 research and innovation programme under grant agreement No 847593.

Status of deliverable		
	By	Date
Delivered (Lead Beneficiary)	J. Samper (UDC) / H. Shao (UFZ)	2023-12-01
Verified (WP Leader)	D. Jacques (SCK CEN)	2023-12-10
Revised	J. Samper (UDC) / H. Shao (UFZ)	2024-01-23
Reviewed (Reviewers)	J.C.L. Meeussen	2024-02-01
Revised	J. Samper (UDC) / H. Shao (UFZ)	2024-20-20
Verified (WP Leader)	D. Jacques (SCK CEN)	2024-20-26
Approved (PMO)		
Submitted to EC (Coordinator)	Andra (Coordinator)	19/03/2024

Executive Summary

Conditioned waste forms and packages are considered in ACED and include a vitrified waste form for High Level Waste (HLW) and a cementitious waste form for Intermediated Level Waste (ILW). Disposal of these waste forms in a geological disposal facility hosted in either crystalline or sedimentary rock types are investigated. Both rock types are porous materials and the chemical composition of their pore waters may induce mineral changes in the engineered barrier system. The evolved pore waters from the engineered system chemically affect the host rock locally. A systematic understanding of the chemical evolution from the waste form up till the host rock can be used for a robust assessment of the impact of these processes.

HLW disposal cell in granite:

Model abstraction methods have included: 1) Hierarchy of models (porosity feedback effect); 2) Delimited input domain (corrosion rate depending on temperature and saturation index; and reduced geochemical system) and; 3) Reduced numerical accuracy (mesh discretization and convergence tolerances). The computed results are very sensitive to the porosity feedback effect. The porosity reaches the threshold porosity in the canister due to the precipitation of the corrosion products. Pore clogging prevents further precipitation and decreases solute diffusion coefficient. This in turn leads to sharp decrease of ISG (International Simple Glass) dissolution. The corrosion rate increases with increasing temperature and decreases with increasing pH and concentration of dissolved iron. A 80% volume fraction of Fe(s) remains uncorroded after 50,000 years when the corrosion rate assumed to depend on saturation index. The precipitation of corrosion products such as magnetite and siderite for variable corrosion rate is smaller than the precipitation for a constant corrosion rate. A simulation run was performed in which smectite dissolution was neglected by considering smectite as an unreactive mineral phase to reduce the geochemical system. The general trends of the computed concentrations of dissolved, exchanged and sorbed species and mineral volume fractions are generally like the base case. A simulation run was performed with a grid not refined near the interfaces. The general behaviour of the numerical results with the less refined mesh are like those of the base case. However, it is important to point out that with the refined mesh used in the base case: (1) The gradient results at the interfaces are better represented; and (2) The computing time increases almost 2 times. Computed results for the convergence tolerances of $\varepsilon = 10^{-3}$ and 10^{-6} follow the same trend. However, considering the large tolerance could provide a lower fidelity solution, especially at the interface where there are the larger mineral precipitation/dissolution. On the other hand, the CPU time increases when the convergence tolerance decreases.

Additional sensitivity runs were performed to study the sensitivity of the predictions to the silica saturation threshold and to the earlier canister failure with a shorter duration of Period II. A decrease in the silica saturation threshold leads to a decrease in glass dissolution rate. but it does not affect the computed pH. Shortening the duration of Period II from 25,000 years to 10,000 years has a significant impact in the ISG glass dissolution front after 50,000 years. The volume fraction of the precipitated corrosion products in the sensitivity run with an earlier canister failure and a shorter duration of Period II is smaller than in the base run because ISG glass dissolution causes greenalite precipitation instead of magnetite and siderite precipitation.

A metamodel has been developed for a simple geochemical system representative of the interactions of steel/bentonite and precipitation of corrosion products. The geochemical system includes 3 primary dissolved species (Fe^{2+}, H^+ and O_2(aq)), two aqueous complexes (OH^- and H_2aq) and a mineral (magnetite). The range of the total Fe concentrations was estimated from the canister corrosion in 50,000 years. A set of 5000 data were sampled with a Latin Hyper Cube (LHC) sequence for three variables. Then, batch simulations were performed with CORE^{2D}v5 for the 5000 combinations data of the total Fe, H and O_2. The following output data were obtained: 1) Aqueous primary concentrations: Fe^{2+}, H^+, O_2(aq); 2) Aqueous secondary concentrations: OH^-, H_2(aq); 3) Magnetite; 4) pH and 5) Eh. Gaussian Processes (GP) approach was adopted by UDC. 2500 data were used to train the metamodel and 2500 data were used to validate the metamodel. The metamodel is based on Gaussian Processes and Random Forests for defining two groups corresponding to high pH values (pH > 9) and lower pH values (pH ≤ 9). The metamodel provides excellent results for most of the output variables. Working with log for concentrations of H, OH and O_2 improves significantly the results for H and O_2, but leads to worse results for OH. When the metamodel is trained by working with concentrations of dissolved Fe, the validation results show some cases (617 out of 5000) with negative concentrations. On the other hand, when the metamodel is trained by working with the logarithm of the concentrations of dissolved Fe, the predicted validation concentrations are always positive, but the metrics of the validation are slightly worse. The accuracy of the metamodel is significantly improved for pH and by defining two groups, one for pH ≤ 9 and another for pH > 9.

HLW disposal cell in clay:

Reactive transport modelling with HYTEC was developed to assess of the chemical evolution of the full system including the “vitrified waste – steel overpack – concrete buffer – clay host rock”. Full water saturation and isothermal condition at 25°C were considered. Sensitivity analysis were performed in complement to the base cases of Deliverable D217. HYTEC led to a similar sequence of chemical alteration of the cementitious buffer as in the other cases without cracks but cracking might significantly decrease the buffer lifetime. On the other hand, there was a clear possibility of clogging at the cement/clay interface as well as in the steel overpack by the formation of corrosion products, that should increase the buffer lifetime.

ILW disposal cell in clay:

In this study we found that the difference of the drum model, which is introduced and studied in D2.16, in comparison with this drum model here, leads to significant differences in gas generation rates for the first 50 years. The increased amount of fast degrading cellulose, increases the methane and CO_2 production rate, but as the cement carbonation reaction consumes the CO_2 and releases water, the water is then available for further degradation of organics. As the fast corroding metal waste inside of the drum is missing in this study, the overall net water consumption rate is much lower leading to lower but more constant gas net generation rate of the first 500 years. The single container study in D2.16 has a higher gas generation rate with a sharp drop after 50 years when available water has been consumed.

The presented gallery scale simulation is one of the first having a detailed resolution of the drum characteristics. This allows a more precisely simulation of the gas pressure evolution and its consequences on the repository safety function. Additionally, the impact of changes of different material parameters is interest to find parameters leading to a minimization of the gas pressure peak. In this study the simulation time does not cover the increase of hydrogen generation of the metal containers due to pH decrease by the ASR reaction. This will happen under saturated conditions after around 1000 years and could potentially lead to a new gas pressure maximum. This study shows that it is unlikely that CO_2 migrates towards the metal containers if there are no fractures in the mortar. Therefore, it is unlikely that cement carbonation leads to a significant drop in pH in the metal containers and increase in corrosion rates. However, this has to be studied/confirmed in additional simulations including a 1000+ years simulation time. The model setup here could be further improved by increasing the model size and the mesh resolution especially at the drums and at the transition areas of materials with large properties changes. Additionally, the function for calculating the steel corrosion rate will be replaced by a continuous function in dependence of pH.

ILW disposal cell in granite:

Abstracted models were developed to assess potential chemical evolution of barrier material in the intermediate level waste disposal cell constructed in granitic host rock. The model abstraction included homogenization of the waste zone, simplified geometry, reduced dimensionality and numerical accuracy. In addition, three sensitivity cases with respect to the representation of the waste zone, system layout and groundwater flow regime were analysed. It was found that the main degradation phenomenon in the cementitious material is the dissolution of portlandite, which is followed by the leaching of the C-S-H phases and the formation of calcite. The degradation rate strongly depends on the conceptual model and boundary conditions. 2D model can better represent the analysed system as it allows to identify non-homogenous propagation of the high pH front and component transport. A sensitivity case, where the waste zone was considered as an empty space filled with the pore water of the vault backfill mortar, demonstrated that the degradation kinetics in this case is faster compared to the reference case where backfill mortar was placed in the waste zone. Due to clogging of the pores, in about 20,000 years, the porosity of the area close to the border was approaching 0 and no space was available for transporting the solution. The sensitivity case for investigations of the system layout effect considered the disposal cell concept based on the ILW repository in Olkiluoto, Finland. This system exhibited similar behavior to the reference case, however, the degradation of cementitious materials extended further into the waste zone due to differences in the backfill material. Analysis of the water flow rate effect on chemical evolution in the disposal cell in granite was performed assuming no flow conditions allowing only transfer by diffusion. The modelling results indicated that the groundwater flow rate could significantly affect the chemical evolution in the analysed disposal cell.

Next, it was investigated if a reactive transport simulation of the ILW-granite system could be accelerated by replacing the geochemical solver in the reactive transport code by a surrogate model or emulator, for a model based on the abstracted models described here above. Results for a cement system [C,Ca,Si,O,H] show for the first time that DNN can substantially speed up reactive transport simulation in cement systems while accurately capturing both dissolution (portlandite and CSH) and precipitation (calcite). Although these were based on simplified geochemical models of the granite-cement porous materials, decalcification and carbonation fronts were in accordance with the 1D models using a more complete geochemical model. Preliminary results for the complex cement system [C,Ca,Si,Al,Cl,K,Na,Mg,S,O,H] might show the limits of offline training of black-box surrogate geochemical models for accelerating RT simulation in cement systems. This highlights the importance of deriving high-quality training samples.

Table of content

List of figures

List of Tables

Glossary

ASR	Alkaline-Silica-Reactions
CPU	Central Processing Unit
CASH	Calcium aluminium silicate hydrate
CSH	Calcium silicate hydrate
DNN	Deep neural network
EDZ	Excavation Damaged Zone
FE	Finite element
FEBEX	Full-scale Engineered Barriers Experiment
FFN	Feedforward network
GP	Gaussian Processes
HLW	High level waste
ILW	Intermediate Level Waste
ISG	International Simple Glass
kNN	k-nearest neighbor
LHC	Latin Hyper Cube
MC	Monte Carlo
ML	Machine learning
MLP	Multilayer perceptron
NN	Neural networks
OGS	OpenGeoSys
PINNs	Physics-informed neural networks
PFE	Porosity feedback effect
SRG	Spanish Reference Granitic
ReLU	Rectified linear unit
REV	Representative elementary volume
RT	Reactive transport
SIA	Sequential iteration approach

1. Introduction

Task 4.2 consists of developing and evaluating robust and manageable models in order to efficiently represent complex and coupled processes at the disposal cell scale. Model abstraction methodologies represent the complex interacting processes with more simple descriptions such as geometrical simplification, process simplification of equilibrium or kinetic processes, and look-up tables. An important element in model abstraction is that the simplified models are still able to simulate the key features of chemical evolution of a disposal cell as predicted by the complex model. This allows for quantitative predictions of the chemical evolution as boundary conditions for radionuclide release/mobility and estimation of durability of barriers with less complex and computational demanding models applicable for other geometries, for optimization, or for sensitivity calculations. Different levels of model abstraction (ranging from “as realistic or detailed as possible” to “as simple as possible”) have been evaluated. The benefits and limitations of the resulting models should be described in order to assess the added-value of complex modelling in a safety case.

The main milestones of Task 4.2 have included:

1) Identification of key macroscale and up-scaling processes for which the methods are applied (model outputs).
2) Description of abstraction and simplification methods.
3) Integration of abstraction and simplification methods into models.
4) Demonstration of simulation results with abstracted models.
5) Update of the methods and models based on inputs from ACED Tasks 2 and 3.
6) Update of simulation results with abstracted models.

The abstracted models developed in Task 4.2 have been are applied in Task 4.3 to a wide range of conditions encountered in the disposal concepts, which result in a number of different chemical evolutions of the disposal cell. In order to apply the model for a wide range of conditions and parameter values, a large number of model realizations have been simulated. This work also has included sensitivity analyses of the model parameters, mapping of critical parameters to performance targets (e.g. pH, permeability…) and/or risks (loss of containment…), as well as analyzing the response of the system to different environmental conditions. This subtask has included simulations with the developed model in safety case relevant conditions for the ILW/HLW disposal cells. Task 4.3 has been performed with close co-operation with operating companies/end-user groups to implement the knowledge gained in this WP to their safety case analyses and evaluate the full performance of the developed model. The collaboration also has provided repository performance targets that will be used in sensitivity analysis of them to the model parameters.

The main milestones of Task 4.3 have included:

1) Interactions with the end-users group in co-operation with Task 1.1 in a workshop.
2) Definition of calculation cases and parameter ranges.
3) Compilation of calculation cases and parameter ranges from national HLW/ILW representative cases.
4) Performing simulations and sensitivity analyses from the models from Task 4.2.

2. Reference HLW disposal cell in granite

2.1 Short description of the reference HLW disposal cell in granite

The HLW disposal cell concept in granitic host rock includes: (1) The vitrified waste (40 cm in diameter) which is explicitly considered in the reactive transport model and is coupled with the rest of the engineered barrier components; (2) The canister which is a carbon-steel canister (5 cm thick); (3) The bentonite buffer (75 cm thick) which is composed of water-saturated FEBEX bentonite with a dry density of 1600 kg/m3; and (4) The Spanish Reference Granitic (SRG) host rock (25 m) (*Figure 2-1*). This HLW disposal cell concept in granite is not specific of any country but aims at representing several national concepts. This concept is based on the Spanish spent fuel reference concept in granite, known as ENRESA 2000 (ENRESA, 2000). The main differences between these two concepts are the type of waste (vitrified waste vs. spent fuel) and the dimensions of the carbon-steel canister (45 cm in diameter for vitrified waste and 90 cm for spent fuel). The materials and dimensions of the nuclear waste form, the canister, the engineered barrier and the host rock selected for the HLW disposal cell in granite were taken from Samper et al. (2021).

In ENRESA (2000) the carbon steel canisters are placed on horizontal disposal drifts with a separation of 2 m from one another. Canisters are surrounded by high-density blocks of bentonite which are initially unsaturated with a gravimetric water content of 14%. The disposal drifts of 500 m in length and 2.4 m in diameter are located at a depth of 500 m in the granitic host formation and separated 35 m to prevent exceeding a temperature of 100 ºC in the bentonite. The access is accomplished by "main drifts" which run perpendicular to the disposal drifts. The main drifts meet at a central area, which includes the required underground infrastructure. The granitic formation is selected to have a low fracture density, tectonic stability, low seismicity, and appropriate geochemical conditions.

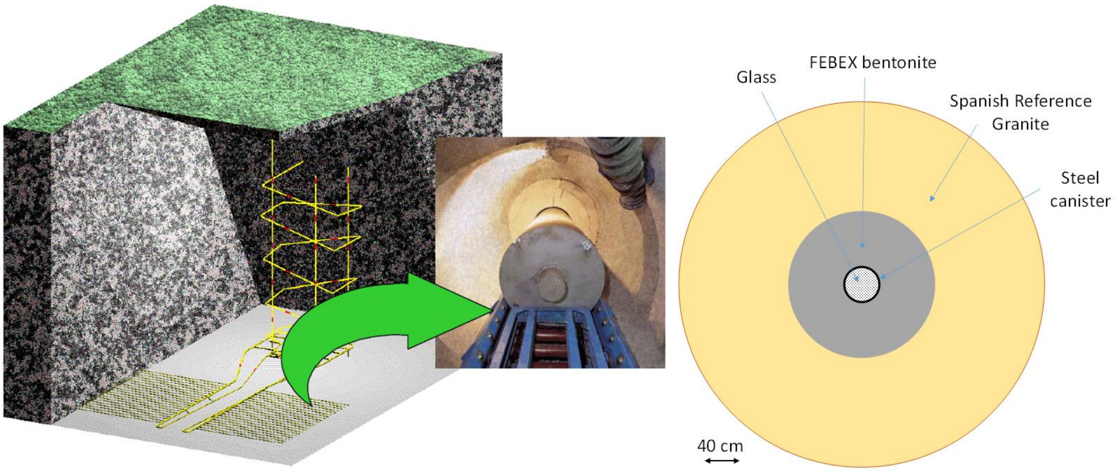

Figure 2-1. Underground installations of a radioactive waste repository in granite according to the Spanish Reference Concept for spent fuel (ENRESA, 2001). Layout of the representative HLW disposal cell concept in a granitic host rock selected in the ACED Work Package of the EURAD Project (Samper et al., 2021) which includes the vitrified waste (40 cm diameter), the steel canister (5 cm thick), the FEBEX bentonite buffer (75 cm thickness) and the Spanish Reference Granite.

2.2 Relevant output variables

The relevant outcomes of the reactive transport model of the HLW disposal cell in granite are focused on the time evolution at selected locations and interfaces and the spatial distribution at selected times of:

1) The computed pH and redox.
2) The computed concentrations of the dissolved chemical species, including Na, K, Ca, Mg, Cl, HCO_3^-, SO_4^{-2}, Si, Fe and Al.
3) The computed concentrations of mineral phases such as Fe(s), ISG (International Simple Glass), calcite, gypsum, quartz, magnetite, siderite, goethite, greenalite, cronstedtite, montmorillonite, nontronite and saponite.
4) The computed volume fractions of the mineral phases such as Fe(s), ISG, calcite, gypsum, quartz, magnetite, siderite, goethite, greenalite, cronstedtite, montmorillonite, nontronite and saponite.
5) The computed concentrations of exchanged cations (Na, K, Ca, Mg, Fe) and surface complexes.
6) The computed changes in porosity.
7) The lifetime or durability of the bentonite buffer and the carbon steel overpack (time at which the overpack will fail).

The results of the detailed reactive transport models developed in Subtask 4.1 have been used for constructing abstracted models in Subtask 4.2.

2.3 Lower fidelity models

2.3.1 Hierarchy of models

2.3.1.1 Porosity feedback effect

The base case of the non-isothermal reactive transport model of the long-term geochemical evolution of a HLW disposal cell in a granite presented in D2.17 (De Windt et al., 2023) within the Subtask 4.1 does not consider the porosity feedback effect (PFE) on chemical and transport parameters. A sensitivity run was performed by considering the PFE in a manner described by Águila et al. (2020). CORE^{2D}V5 considers the changes in porosity and updates flow, transport, and chemical parameters. The porosity, ϕ, is updated each time step from the computed values of the mineral volume fractions, f_m, according to:

$$\emptyset = 1 - \sum_{m=1}^{N_p} f_m \qquad [2\text{-}1]$$

The changes in the permeability are calculated from the Kozeny-Carma equation which relates the properties of the porous medium to the flow resistance in pore channels through:

$$k = k_o \frac{(1-\emptyset_0)^2}{(1-\emptyset)^2}\left(\frac{\emptyset}{\emptyset_0}\right)^3$$

*[**Erreur ! Source du renvoi introuvable.**-2]*

The pore diffusion coefficients are updated by using the Archie's law which describes the ratio between the effective diffusion of a solute in a porous medium and its diffusion coefficient in pure water by the following expression:

$$D_e = D_0 \emptyset^m$$

*[**Erreur ! Source du renvoi introuvable.**-3]*

The specific surface of the minerals in saturated porous media (expressed as the surface of mineral per unit volume of water) is updated each time step according to:

$$A_m^{t+1} = A_m^t \frac{\emptyset^t}{\emptyset^{t+1}}$$

***[Erreur ! Source du renvoi introuvable.**-4]*

Transport parameters are dynamically updated and mineral precipitation is restricted to ensure that porosity does not decrease below a threshold value. The threshold porosity was taken equal to 10^{-5}. Numerical results are very sensitive to the PFE. The porosity reaches the threshold porosity in the canister due to the precipitation of the corrosion products. Pore clogging prevents further precipitation and decreases solute diffusion coefficient. This in turn leads to sharp decrease of ISG dissolution.

Figure 2-2 shows the spatial distribution of magnetite precipitation at 25,000 and 50,000 years for the base case and the sensitivity run. Magnetite precipitation in the sensitivity run stops when the threshold porosity is reached. Greenalite precipitation in the sensitivity run is also smaller much than in the base run (Figure 2-3). The same computed results are obtained for siderite and calcite precipitation (not shown here). ISG glass dissolution is greatly reduced in the sensitivity run because the glass dissolution rate depends on pH and silica concentration. The glass dissolution rate drops to the residual dissolution rate (Figure 2-4).

Figure 2-5 shows the computed spatial distribution of pH at 25,000 and 50,000 years in the base case and the sensitivity run. It can be seen that the pH in the glass increases until 12.5 due to the residual dissolution rate. The pH is maintained high because solute transport from (into) the canister is prevented by pore clogging.

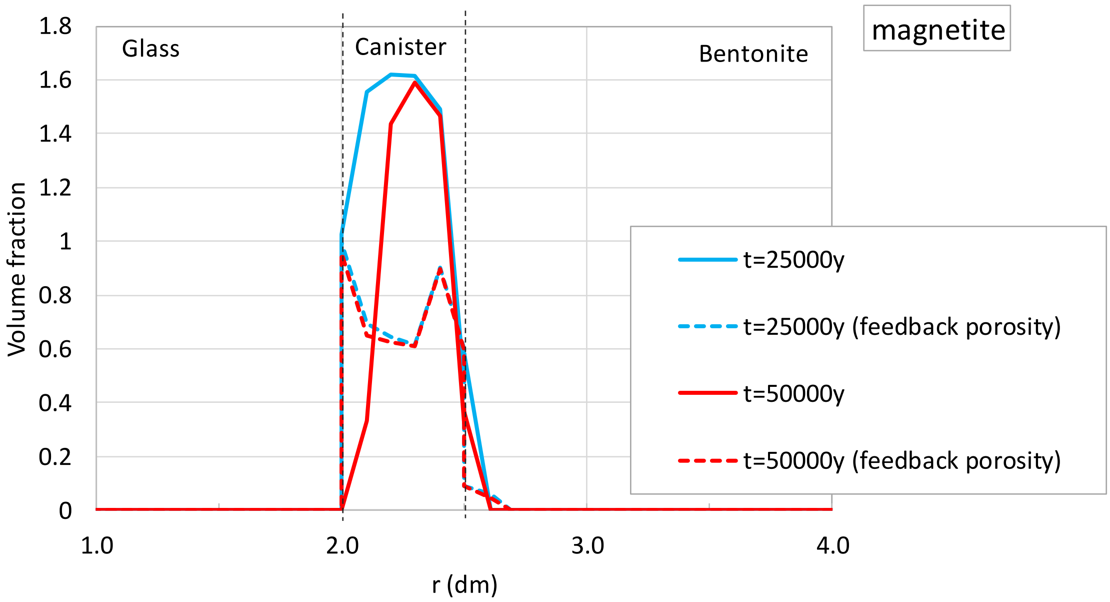

Figure 2-2. Spatial distribution of the computed volume fraction of magnetite in the base run and the sensitivity run with PFE at 25,000 and 50,000 years.

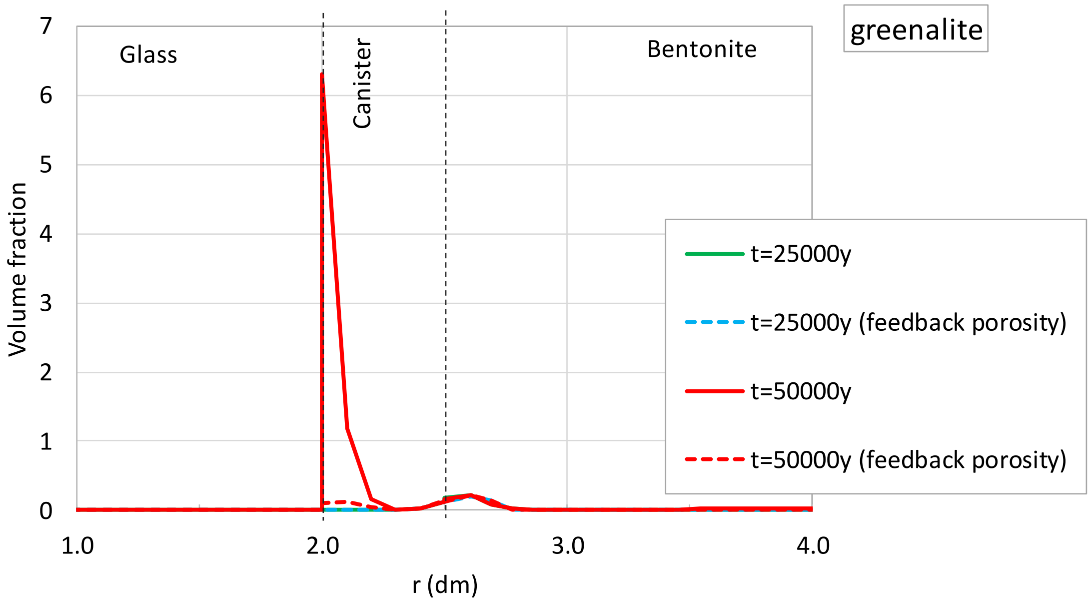

Figure 2-3. Spatial distribution of the computed volume fraction of greenalite in the base run and the sensitivity run with PFE at 25,000 and 50,000 years.

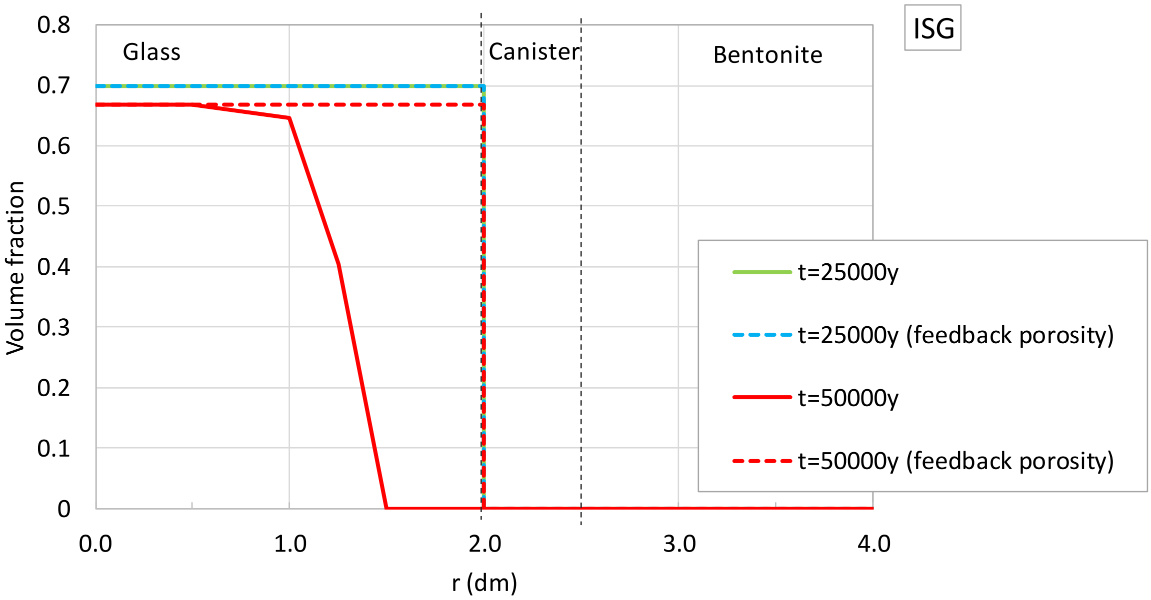

Figure 2-4. Spatial distribution of the computed volume fraction of ISG in the base run and the sensitivity run with PFE at 25,000 and 50,000 years.

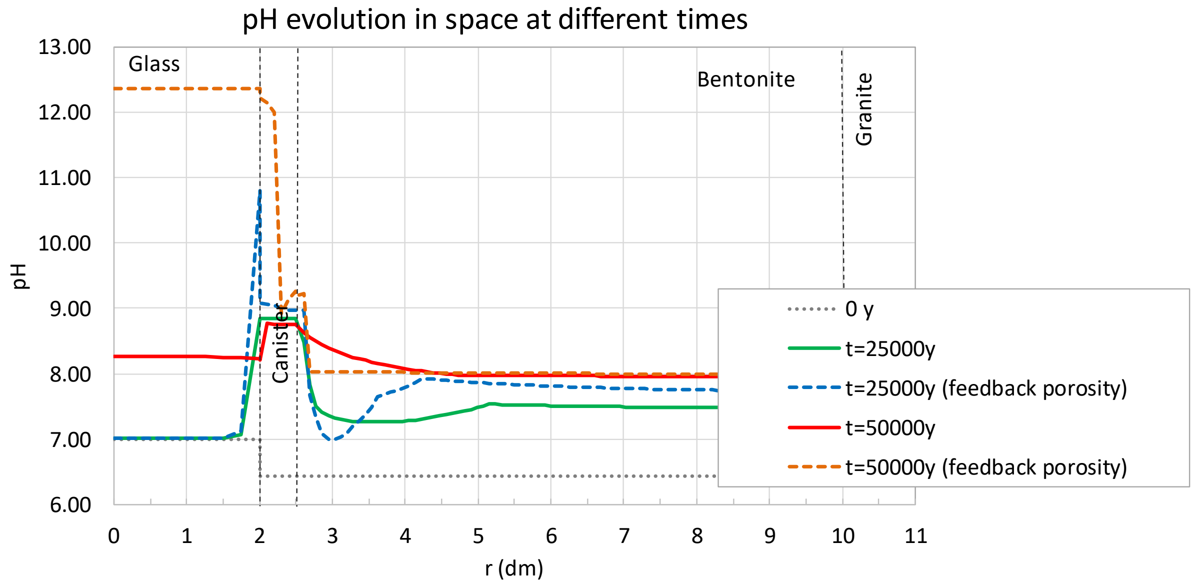

Figure 2-5. Spatial distribution of the computed pH in the base run and the sensitivity run with PFE at 25,000 and 50,000 years.

2.3.2 Delimited input domain

2.3.2.1 Corrosion rate depending on temperature and saturation index

The base case presented in D2.17 (De Windt et al., 2023) within the Subtask 4.1 considers an anaerobic constant corrosion rate in a canister made of metallic iron (Fe(s)). In the sensitivity run, the corrosion rate is assumed to vary with temperature and Fe(s) saturation index. The corrosion rate increases with increasing temperature and decreases with increasing pH and concentration of dissolved iron as described by Samper et al. (2016). Although the corrosion rate doubles when the temperature at the canister/bentonite interface is above 90ºC, the duration of the thermal pulse is not long enough to significantly affect the model predictions at the end of Period II (canister corrosion). Accounting for the dependence of the corrosion rate on the saturation index, however, slows down the corrosion rate (Figure 2-6). A 80% volume fraction of Fe(s) remains uncorroded after 50,000 years when the corrosion rate assumed to depend on saturation index. The precipitation of corrosion products such as magnetite and siderite for variable corrosion rate is smaller than the precipitation for a constant corrosion rate. Model results show a slighly decreasing in the corrosion rate at 25,000 years when glass dissolution starts. ISG glass dissolution leads to magnetite redissolution and greenalite precipitation. Greenalite precipitation in the sensitivity run is slightly larger than that of the base run. Calcite dissolution/precipitation and ISG glass dissolution are not sensitive to a variable corrosion rate (not shown here).

Figure 2-7 shows the spatial distribution of the computed pH at selected times. The pH in the sensitivity run in the canister, the glass and the bentonite at 25,000 years is similar than that of the base run. At 50,000 years the computed pH in the glass is larger for a variable corrosion rate due to the large amount of magnetite redissolution

The computed concentrations of aqueous species and exchanged cations are not sensitive to a variable corrosion rate, except for the concentrations of dissolved, exchanged and sorbed Fe^{2+}, which in the canister-bentonite interface are smaller than those of the base run.

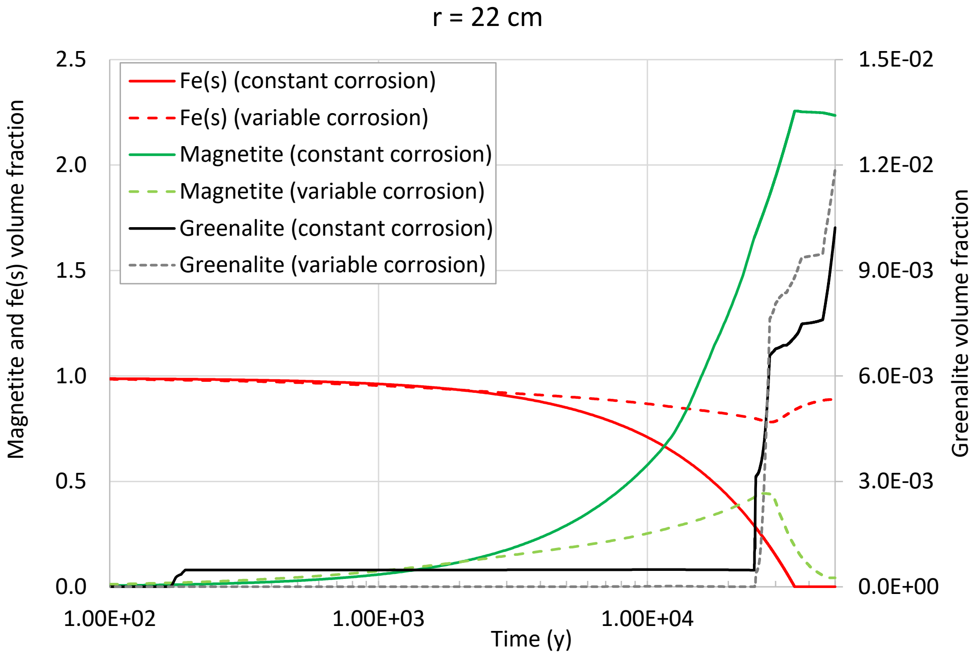

Figure 2-6. Time evolution of the computed volume fraction of Fe(s), magnetite and greenalite in the canister (r = 2.2 dm) in the base run (constant corrosion rate) and in the sensitivity run with corrosion rate depending on saturation index and temperature at 25,000 and 50,000 years.

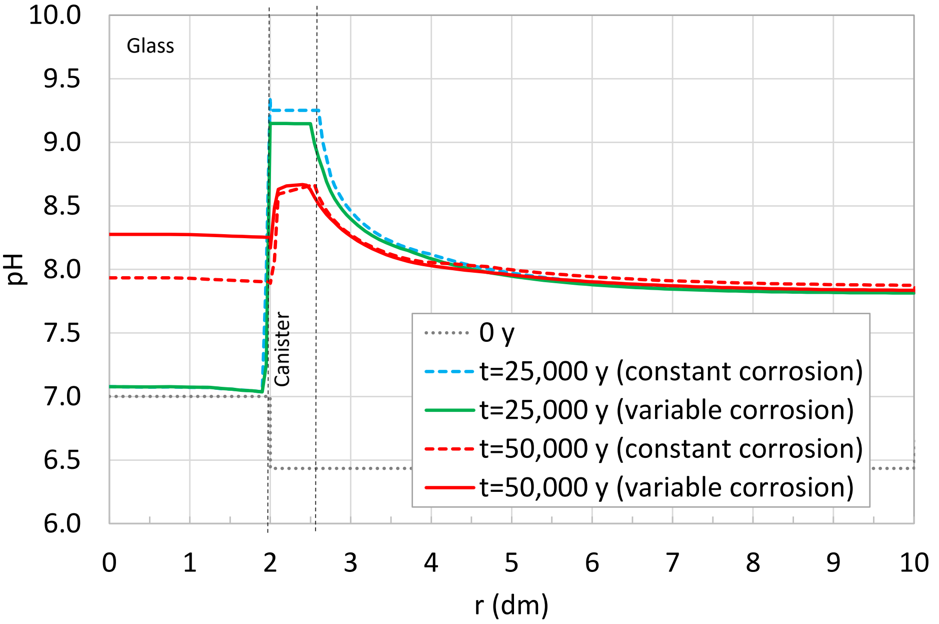

Figure 2-7. Spatial distribution of the computed pH in the base run (constant corrosion rate) and in the sensitivity run with corrosion rate depending on saturation index and temperature at 25,000 and 50,000 years.

2.3.2.2 Reduced complexity of the geochemical system (smectite dissolution)

A simulation run was performed in which smectite dissolution was neglected by considering smectite as an unreactive mineral phase. The general trends of the computed concentrations of dissolved, exchanged and sorbed species and mineral volume fractions are generally similar in the base case presented in D2.17 (De Windt et al., 2023) within the Subtask 4.1 and the sensitivity run without assuming smectite dissolution. It should be considered that only 0.5 % of the smectite is dissolved at the end of Period III (glass dissolution) in the base run. The computed volume fractions of magnetite in the base case and the sensitivity run without smectite dissolution are similar (Figure 2-8). The front of ISG glass dissolution, however, is sensitive to smectite dissolution. The penetration of the dissolution front is larger when smectite dissolution is neglected (Figure 2-9) due to the dissolved silica concentration is smaller to the threshold silica value of the ISG kinetics and leads more glass dissolution.

Figure 2-10 shows the spatial distribution of the computed pH at 25,000 and 50,000 years with and without smectite dissolution. The computed pH profile in the bentonite with smectite dissolution at 25,000 years is larger and smoother than the pH computed without smectite dissolution. The computed pH with smectite dissolution at 50,000 years in the glass is slightly smaller and in the bentonite is slightly larger than those computed without smectite dissolution.

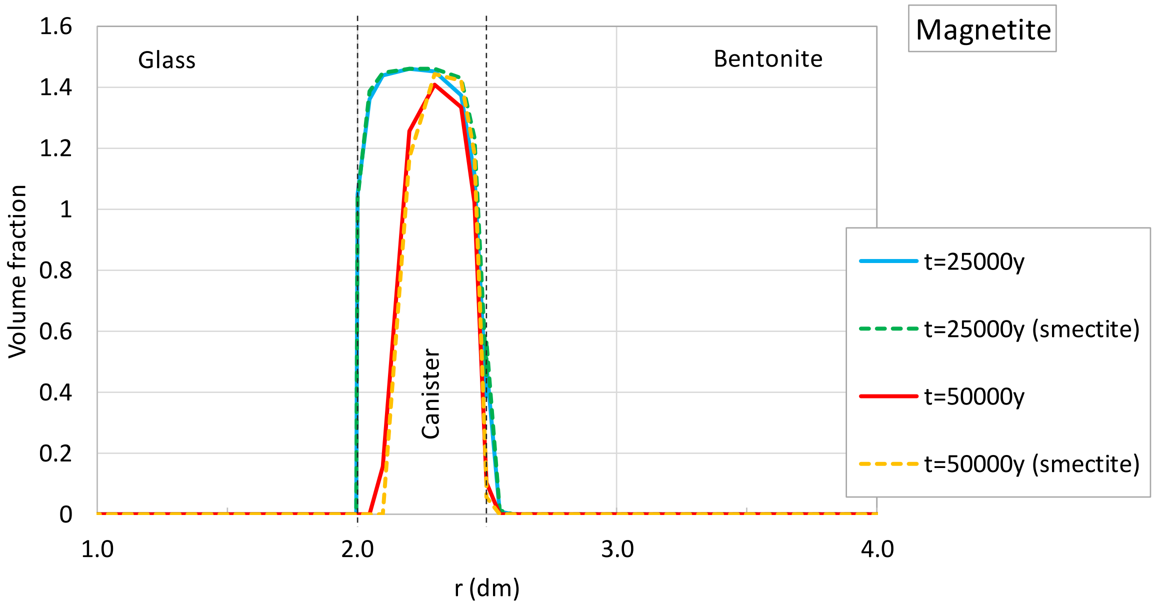

Figure 2-8. Spatial distribution of the computed volume fraction of magnetite in the base run and the sensitivity run without smectite dissolution at 25,000 and 50,000 years.

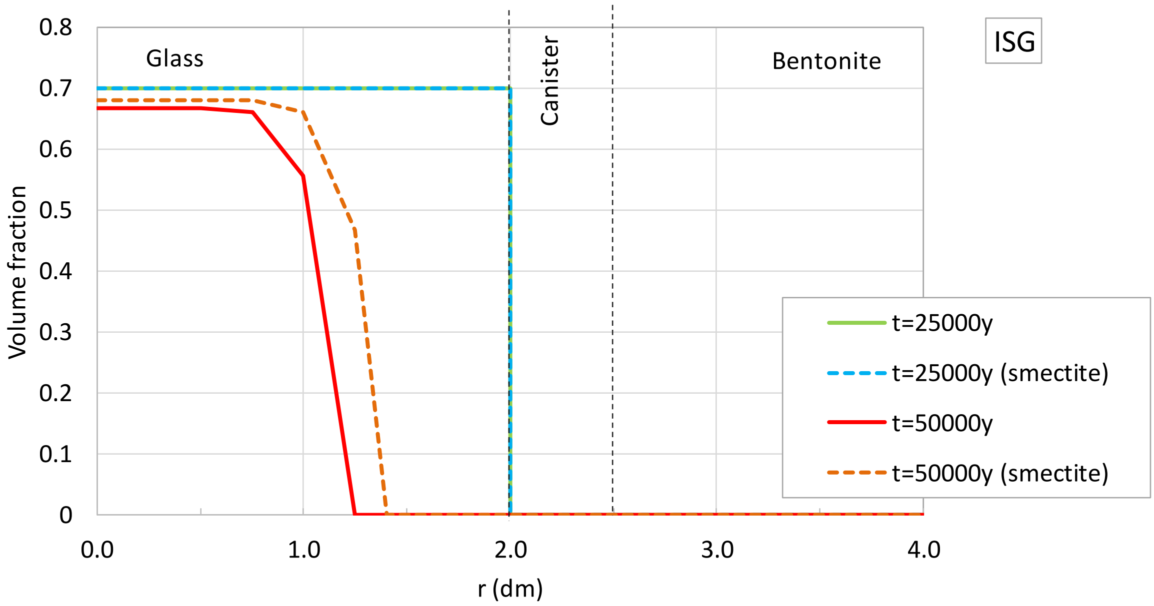

Figure 2-9. Spatial distribution of the computed volume fraction of ISG in the base run and the sensitivity run without smectite dissolution at 25,000 and 50,000 years.

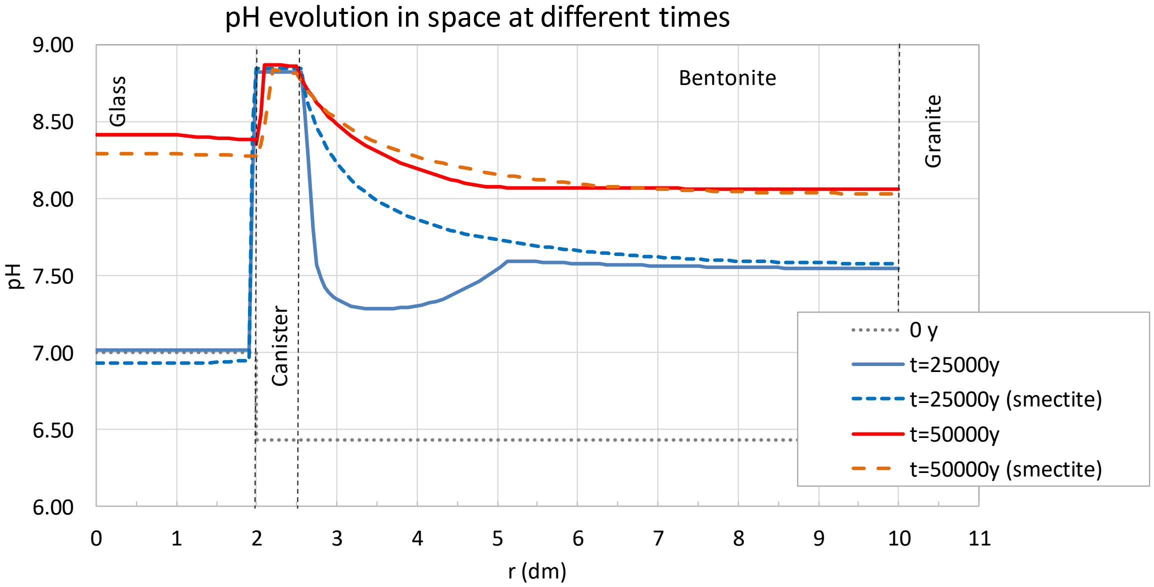

Figure 2-10. Spatial distribution of the computed pH in the base run and the sensitivity run without smectite dissolution at 25,000 and 50,000 years.

2.3.3 Reduced numerical accuracy

2.3.3.1 Mesh discretization

The 1D finite element grid of the base case presented in D2.17 (De Windt et al., 2023) within the Subtask 4.1 has 110 nodes and is more refined at the glass/canister and canister/bentonite interfaces. A simulation run was performed with a grid not refined near the interfaces, having 103 nodes (Figure 2-11).

The general behaviour of the numerical results is similar in both runs. However, it is important to point out that with the refined mesh used in the base case: (1) The gradient results at the interfaces are better represented; and (2) The computing time increases almost 2 times.

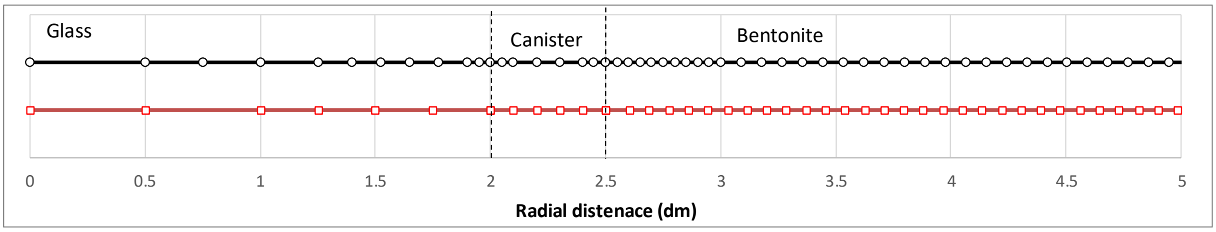

Figure 2-11. 1D finite element grids used in the base run (refined grid of 110 nodes, black symbols) and the sensitivity run (less refined grid with 103 nodes, red symbols).

Figure 2-12 shows the spatial distribution of the computed pH at 25,000 and 50,000 years for the base case and the sensitivity run. The computed pH with both grids at 25,000 years are similar, except for some differences in the glass near the canister interface. The computed pH at 50,000 years with the base run (refined grid) is slightly larger than that computed with the less refined grid.

Magnetite precipitation in the base case (more refined grid) is slightly smaller than that computed with the less refined grid. In addition, the thickness of the magnetite precipitation zone in the bentonite is also smaller in the base run (Figure 2-13). Model results for siderite and greenalite precipitation show similar patterns to those of magnetite (not shown here). The displacement of the front of ISG glass dissolution at 50,000 years is larger in the base case (Figure 2-14). Therefore, the refinement of the grid near the interfaces provides a better representation of the dissolution front.

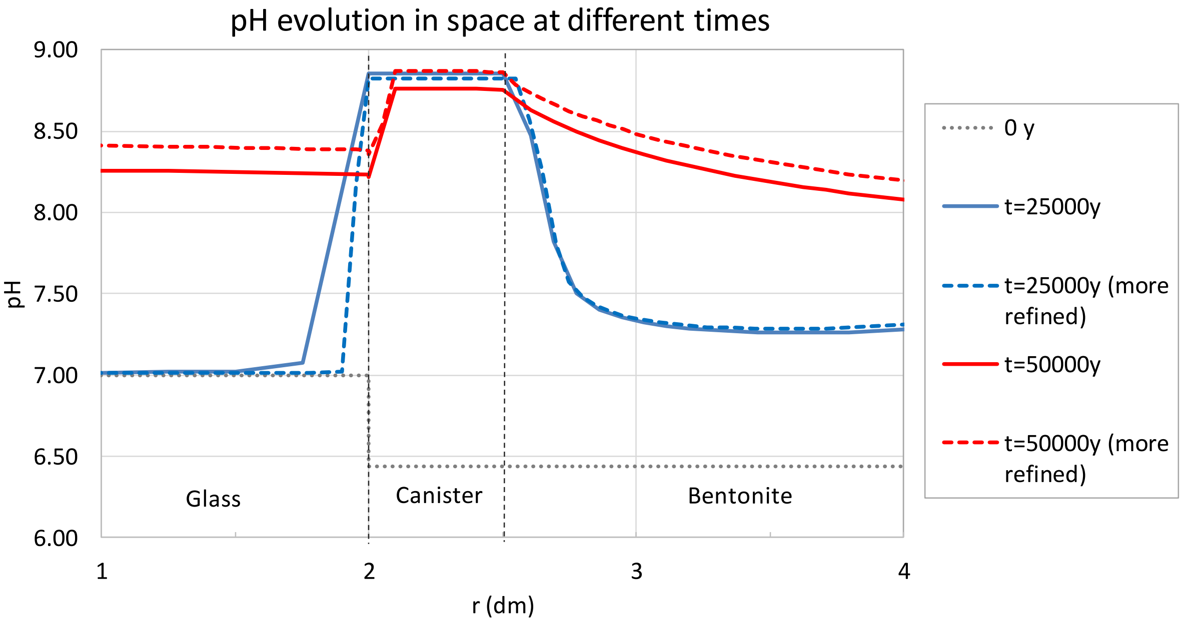

Figure 2-12. Spatial distribution of the computed pH with the base run (refined grid of 110 nodes, dashed lines) and the sensitivity run (less refined grid with 103 nodes, continuous line) at 25,000 and 50,000 years.

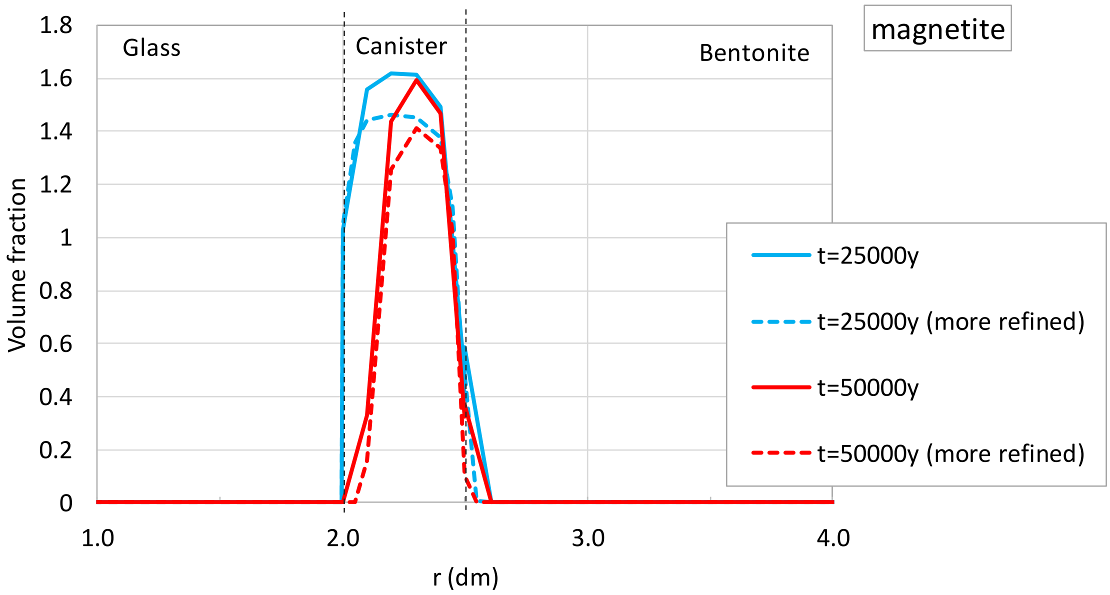

Figure 2-13. Spatial distribution of the computed volume fraction of magnetite with the base run (refined grid of 110 nodes, dashed lines) and the sensitivity run (less refined grid with 103 nodes, continuous line) at 25,000 and 50,000 years.

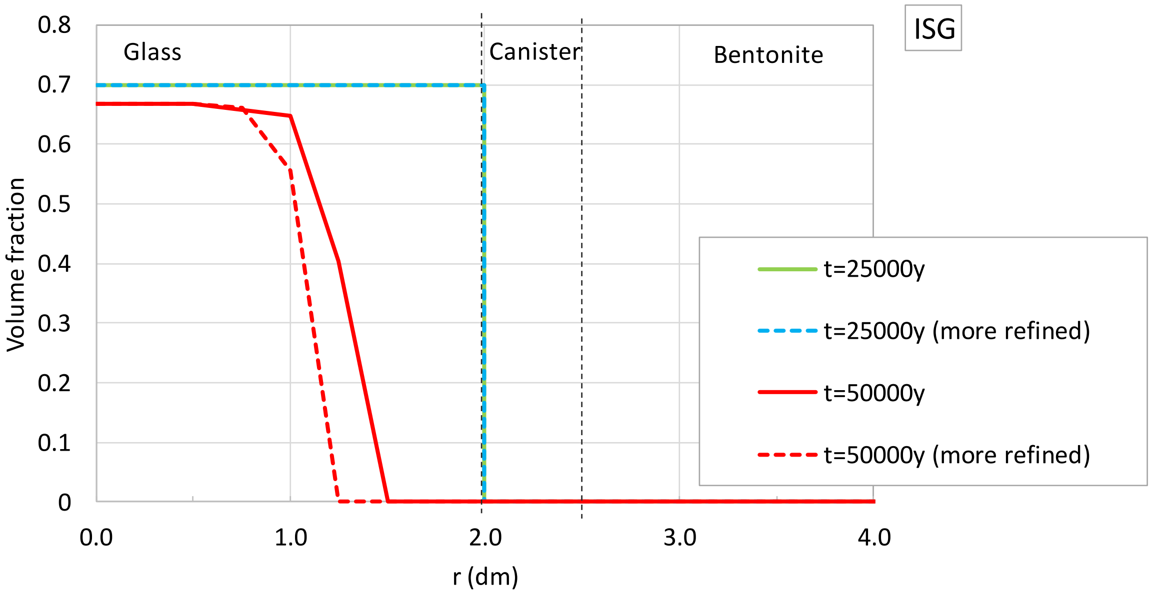

Figure 2-14. Spatial distribution of computed volume fraction of ISG with the base run (refined grid of 110 nodes, dashed lines) and the sensitivity run (less refined grid with 103 nodes, continuous line) at 25,000 and 50,000 years.

2.3.3.2 Convergence tolerances (chemistry & SIA)

A sensitivity run decreasing the tolerance has been performed to analyse the computed solution fidelity. The tolerances of the chemistry and the SIA iterations have been reduced one thousand times (from 10^{-3} to 10^{-6}). The CPU computing time increases with the decreasing of the tolerance. The computing time is equal to 3 days in the base run and 24 days for the tolerance of 10^{-6}.

Figure 2-15 shows the computed pH with the base run ($\varepsilon = 10^{-3}$) and the sensitivity run ($\varepsilon = 10^{-6}$) at 25,000 and 50,000 years. Computed pH is similar for $\varepsilon = 10^{-3}$ and $\varepsilon = 10^{-6}$ at 25,000 years. Computed pH for $\varepsilon = 10^{-3}$ is slightly larger than thar for $\varepsilon = 10^{-6}$ in the glass and in the concrete at 50,000 years.

Figure 2-16 shows computed greenalite volume fraction with the base run and the sensitivity run. Computed greenalite trend is the same for the base run and the sensitivity run. Computed greenalite at the glass/concrete interface for $\varepsilon = 10^{-3}$ is smaller than that for $\varepsilon = 10^{-6}$.

Figure 2-17 shows computed magnetite volume fraction with the base run and the sensitivity run. Computed magnetite for $\varepsilon = 10^{-3}$ is slightly larger than that for $\varepsilon = 10^{-6}$. The advance of magnetite precipitation at the glass/canister and the canister/bentonite interfaces for $\varepsilon = 10^{-3}$ is slightly larger than that for $\varepsilon = 10^{-6}$.

Computed ISG dissolution front for $\varepsilon = 10^{-6}$ moves faster into the glass than that for $\varepsilon = 10^{-3}$ (*Figure 2-18*).

Computed general results for $\varepsilon = 10^{-3}$ and 10^{-6} follow the same trend. However, considering the large tolerance could provide a lower fidelity solution, especially at the interface where there are the larger mineral precipitation/dissolution.

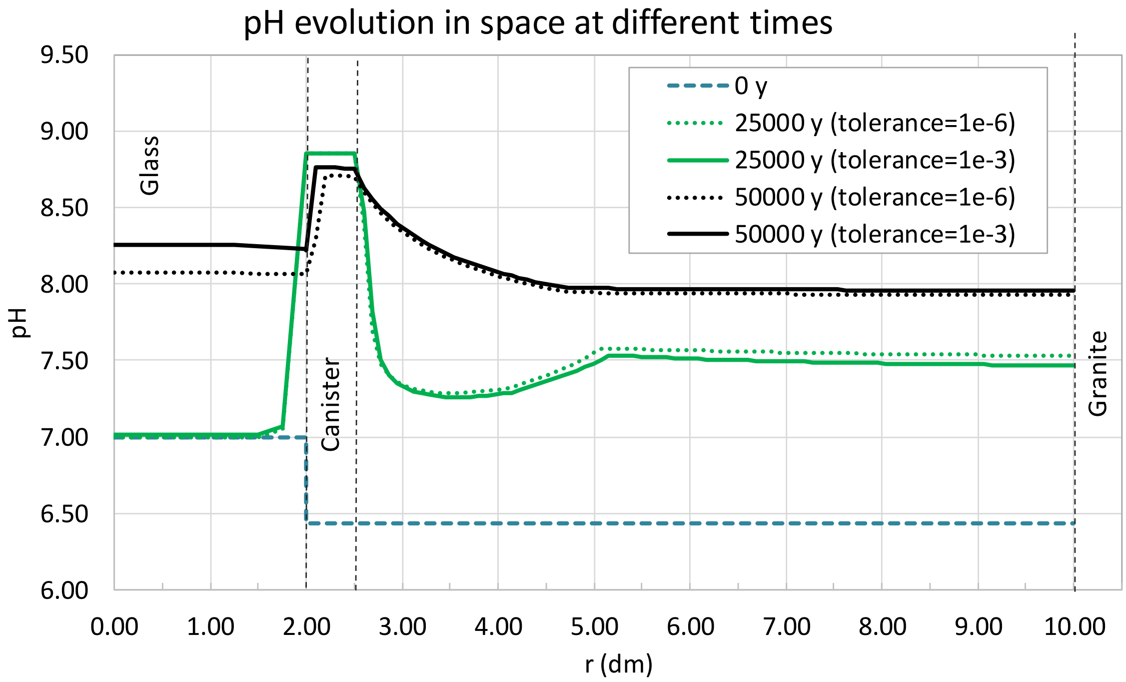

Figure 2-15. Spatial distribution of computed pH with the base run ($\varepsilon = 10^{-3}$) and the sensitivity run ($\varepsilon = 10^{-6}$) at 25,000 and 50,000 years.

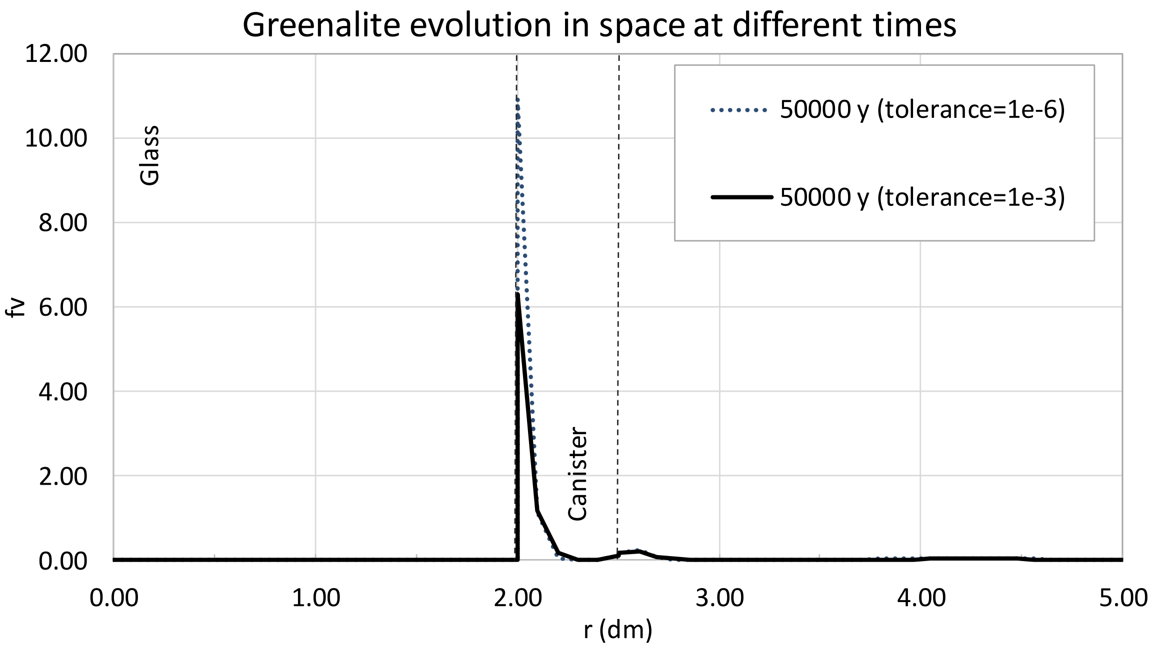

Figure 2-16. Spatial distribution of computed greenalite volume fraction (fv) with the base run (ε = 10^{-3}) and the sensitivity run (ε = 10^{-6}) at 50,000 years.

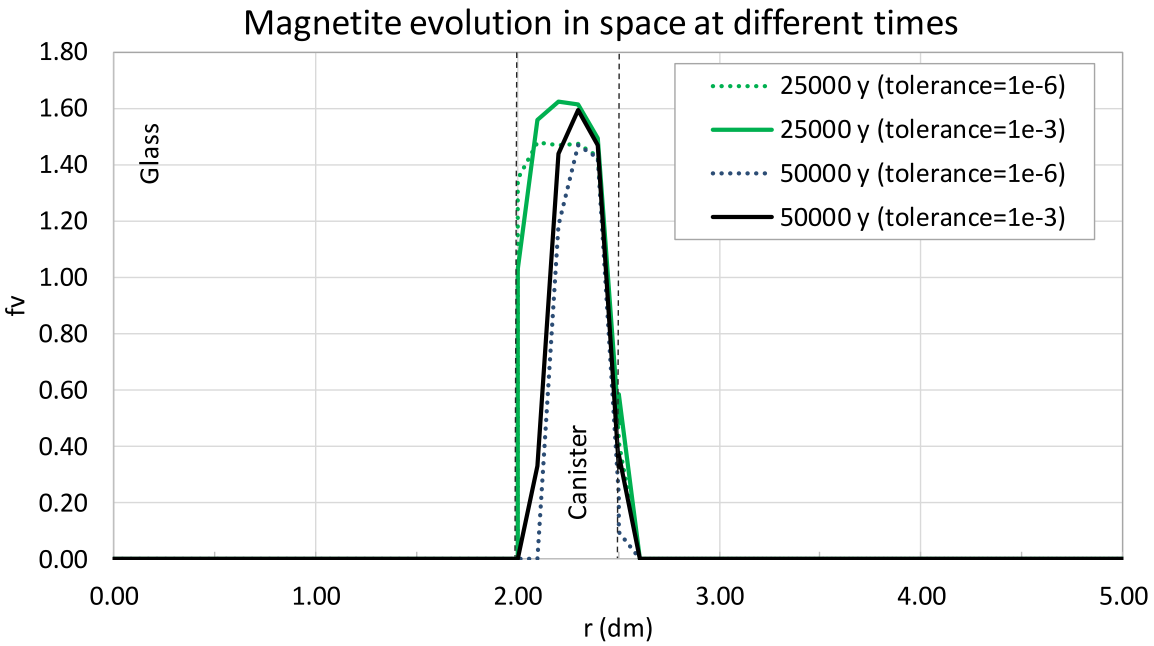

Figure 2-17. Spatial distribution of computed magnetite volume fraction (fv) with the base run (ε = 10^{-3}) and the sensitivity run (ε = 10^{-6}) at 25,000 and 50,000 years.

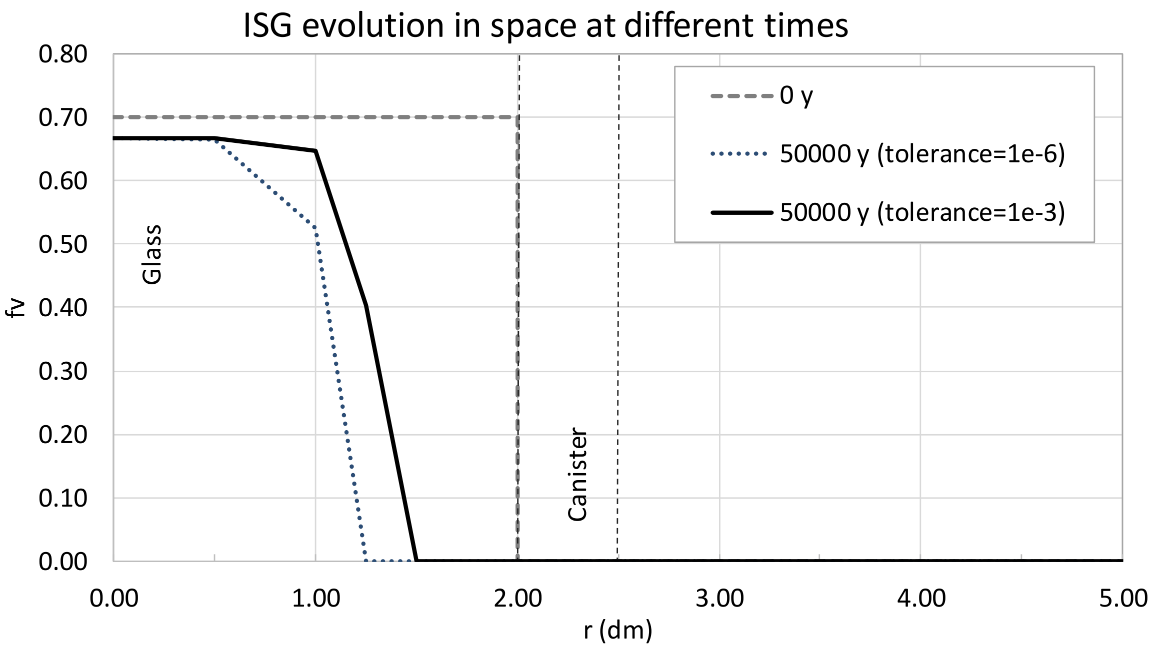

Figure 2-18. Spatial distribution of computed ISG volume fraction (fv) with the base run ($\varepsilon = 10^{-3}$) and the sensitivity run ($\varepsilon = 10^{-6}$) at 50,000 years.

2.4 Surrogate models

The following methodology was proposed: 1) Metamodels for solving the geochemical reactions; 2) Metamodels as alternatives of the geochemical solver of CORE^{2D}; and 3) Metamodels as predictors of the geochemical solver of CORE^{2D}. Here we report only the performance of the metamodels for solving the geochemical reactions (item 1), the training set production and the metamodel.

2.4.1 Geochemical system

A simplified geochemical system representative of the interactions of steel/bentonite and precipitation of corrosion products has been considered. The following primary aqueous species were considered: Fe^{2+}, H^+ and O_2(aq). OH^- and H_2(aq) were considered as secondary aqueous species and magnetite was assumed to be the main corrosion product under chemical equilibrium conditions. Table 2-1 shows the chemical reactions and the equilibrium constants considered.

The range of the total Fe concentrations was estimated from the canister corrosion in 50,000 years taken from the reactive transport model presented in ACED Deliverable D2.17 (De Windt et al., 2023). The ranges of the total O_2 and H concentrations were calculated from those of Fe. Table 2-2 presents the maximum and minimum total concentrations of Fe, O_2 and H.

Table 2-1 - Chemical reactions and equilibrium constants for aqueous complexes and minerals at 25ºC taken from ThermoChimie v10.a (Giffaut et al., 2014).

Reactions	LogK at 25ºC
$Fe(s) + 2\,H^+ + 0.5\,O_2(aq) \leftrightarrow Fe^{2+} + H_2O$	58.85
$OH^- + H^+ \leftrightarrow H_2O$	14.00
$H_2(aq) + 0.5\,O_2(aq) \leftrightarrow H_2O$	46.07
Magnetite + $6\,H^+ \leftrightarrow 3\,Fe^{2+} + 0.5\,O_2(aq)$	-6.56

Table 2-2 - Input parameters and their maximum and minimum values.

Parameter	**Maximum (mol/L)**	**Minimum (mol/L)**
Total Fe	10^{-1}	10^{-4}
Total H	$-2\cdot10^{-4}$	$-2\cdot10^{-1}$
Total O_2	$-5\cdot10^{-5}$	$-5\cdot10^{-2}$

2.4.2 Training data

A set of 5000 data were sampled with a Latin Hyper Cube (LHC) sequence for three input variables: C1, C2 and C3 which correspond to:

1) C1 = Total Fe concentration (mol/L)
2) C2 = Total H concentration (mol/L)
3) C3 = Total O_2 concentration (mol/L)

Batch simulations were performed with CORE^{2D} v5 for 5000 combinations of C1, C2 and C3 data points. The initial guess concentration was considered equal to the initial bentonite pore water concentrations:

1) $Fe^{2+} = 10^{-7}$ mol/L
2) $O_2 = 10^{-65}$ mol/L
3) $H^+ = 5\cdot10^{-6}$ mol/L
4) Magnetite = 0 mol/L

The equilibrium reactions and the magnetite saturation index were calculated. If the magnetite saturation index is lower than 0, the magnetite equilibrium is not calculated, otherwise the magnetite equilibrium is calculated.

Once the batch simulations were performed the output variables could be obtained. The output variables include:

1) Aqueous primary concentrations: Fe^{2+}, H^+, O_2(aq)
2) Aqueous secondary concentrations: OH^-, H_2(aq)
3) Magnetite
4) pH
5) Eh

Figure 2-19 shows an extract of the training data set including: 1) Input data (total Fe, O and H) and 2) Output data (aqueous concentrations, magnetite, pH and Eh).

Figures from Figure 2-20 to Figure 2-28 show the scatter plot of the output variables versus the input variables. Magnetite precipitation shows a clear top boundary which increases with the total Fe and decreases with the total H^+. Two separated groups of computed pH and Eh can be distinguished: 1) pH around 12 and 8; 2) Eh around -0.5 and around -0.8.

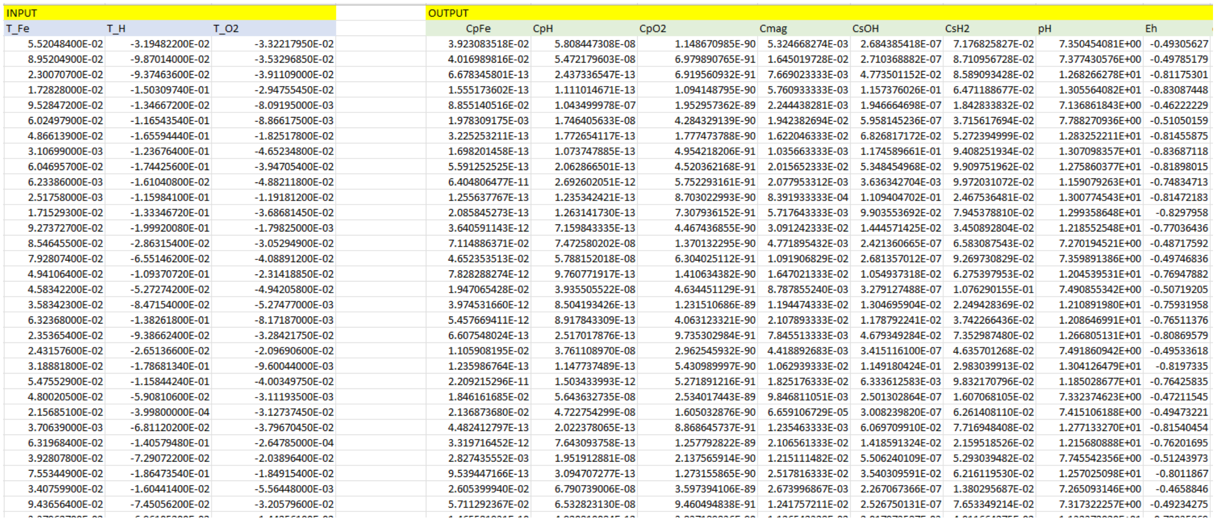

INPUT			OUTPUT							
T_Fe	T_H	T_O2	CpFe	CpH	CpO2	Cmag	CsOH	CsH2	pH	Eh
5.52048400E-02	-3.19482200E-02	-3.32217950E-02	3.923083518E-02	5.808447308E-08	1.148670985E-90	5.324668274E-03	2.684385418E-07	7.176825827E-02	7.350454081E+00	-0.49305627
8.95204900E-02	-9.87014000E-02	-3.53296850E-02	4.016989816E-02	5.472179603E-08	6.979890765E-91	1.645019728E-02	2.710368882E-07	8.710956728E-02	7.377430576E+00	-0.49785179
2.30070700E-02	-9.37463600E-02	-3.91109000E-02	6.678345801E-13	2.437336547E-13	6.919560932E-91	7.669023333E-03	4.773501152E-02	8.589093428E-02	1.268266278E+01	-0.81175301
1.72828000E-02	-1.50309740E-01	-2.94755450E-02	1.555173602E-13	1.111014671E-13	1.094148795E-90	5.760933333E-03	1.157376026E-01	6.471188677E-02	1.305564082E+01	-0.83087448
9.52847200E-02	-1.34667200E-02	-8.09195000E-03	8.855140516E-02	1.043499978E-07	1.952957362E-89	2.244438281E-03	1.946664698E-07	1.842833832E-02	7.136861843E+00	-0.46222229
6.02497900E-02	-1.16543540E-01	-8.86617500E-03	1.978309175E-03	1.746405633E-08	4.284329139E-90	1.942382694E-02	5.958145236E-07	3.715617694E-02	7.788270936E+00	-0.51050159
4.86613900E-02	-1.65594440E-01	-1.82517800E-02	3.225253211E-13	1.772654117E-13	1.777473788E-90	1.622046333E-02	6.826817172E-02	5.272394999E-02	1.283252211E+01	-0.81455875
3.10699000E-03	-1.23676400E-01	-4.65234800E-02	1.698201458E-13	1.073747885E-13	4.954218206E-91	1.035663333E-03	1.174589661E-01	9.408251934E-02	1.307098357E+01	-0.83687118
6.04695700E-02	-1.74425600E-01	-3.94705400E-02	5.591252525E-13	2.062866501E-13	4.520362168E-91	2.015652333E-02	5.348454968E-02	9.909751962E-02	1.275860377E+01	-0.81898015
6.23386000E-03	-1.61040800E-02	-4.88211800E-02	6.404806477E-11	2.692602051E-12	5.752293161E-91	2.077953312E-03	3.636342704E-03	9.972031072E-02	1.159079263E+01	-0.74834713
2.51758000E-03	-1.15984100E-01	-1.19181200E-02	1.255637767E-13	1.235342421E-13	8.703022993E-90	8.391933333E-04	1.109404702E-01	2.467536481E-02	1.300774543E+01	-0.81472183
1.71529300E-02	-1.33346720E-01	-3.68681450E-02	2.085845273E-13	1.263141730E-13	7.307936152E-91	5.717643333E-03	9.903553692E-02	7.945378810E-02	1.299358648E+01	-0.8297958
9.27372700E-02	-1.99920080E-01	-1.79825000E-03	3.640591143E-12	7.159843335E-13	4.467436855E-90	3.091242333E-02	1.444571425E-02	3.450892804E-02	1.218552548E+01	-0.77036436
8.54645500E-02	-2.86315400E-02	-3.05294900E-02	7.114886371E-02	7.472580202E-08	1.370132295E-90	4.771895432E-03	2.421360665E-07	6.583087543E-02	7.270194521E+00	-0.48717592
7.92807400E-02	-6.55146200E-02	-4.08891200E-02	4.652353513E-02	5.788152018E-08	6.304025112E-91	1.091906829E-02	2.681357012E-07	9.269730829E-02	7.359891386E+00	-0.49746836
4.94106400E-02	-1.09370720E-01	-2.31418850E-02	7.828288274E-12	9.760771917E-13	1.410634382E-90	1.647021333E-02	1.054937318E-02	6.275397953E-02	1.204539531E+01	-0.76947882
4.58342200E-02	-5.27274200E-02	-4.94205800E-02	1.947065428E-02	3.935505522E-08	4.634451129E-91	8.787855240E-03	3.279127488E-07	1.076290155E-01	7.490855342E+00	-0.50719205
3.58342300E-02	-8.47154000E-02	-5.27477000E-03	3.974531660E-12	8.504193426E-13	1.231510686E-89	1.194474333E-02	1.304695904E-02	2.249428369E-02	1.210891980E+01	-0.75931958
6.32368000E-02	-1.38261800E-01	-8.17187000E-03	5.457669411E-12	8.917843309E-13	4.063123321E-90	2.107893333E-02	1.178792241E-02	3.742266436E-02	1.208646991E+01	-0.76511376
2.35365400E-02	-9.38662400E-02	-3.28421750E-02	6.607548024E-13	2.517017876E-13	9.735302984E-91	7.845513333E-03	4.679349284E-02	7.352987480E-02	1.266805131E+01	-0.80869579
2.43157600E-02	-2.65136600E-02	-2.09690600E-02	1.105908195E-02	3.761108970E-08	2.962545932E-90	4.418892683E-03	3.415116100E-07	4.635701268E-02	7.491860942E+00	-0.49533618
3.18881800E-02	-1.78681340E-01	-9.60044000E-03	1.235986764E-13	1.147737489E-13	5.430989997E-90	1.062939333E-02	1.149180424E-01	2.983039913E-02	1.304126479E+01	-0.8197335
5.47552900E-02	-1.15844240E-01	-4.00349750E-02	2.209215296E-11	1.503433993E-12	5.271891216E-91	1.825176333E-02	6.333612583E-03	9.832170796E-02	1.185028677E+01	-0.76425835
4.80020500E-02	-5.90810600E-02	-3.11193500E-03	1.846161685E-02	5.643632735E-08	2.534017443E-89	9.846811051E-03	2.501302864E-07	1.607068105E-02	7.332374623E+00	-0.47211545
2.15685100E-02	-3.99800000E-04	-3.12737450E-02	2.136873680E-02	4.722754299E-08	1.605032876E-90	6.659106729E-05	3.008239820E-07	6.261408110E-02	7.415106188E+00	-0.49473221
3.70639000E-03	-6.81120200E-02	-3.79670450E-02	4.482412797E-13	2.022378065E-13	8.868645737E-91	1.235463333E-03	6.069709910E-02	7.716948408E-02	1.277133270E+01	-0.81540454
6.31968400E-02	-1.40579480E-01	-2.64785000E-04	3.319716452E-12	7.643093758E-13	1.257792822E-89	2.106561333E-02	1.418591324E-02	2.159518526E-02	1.215680888E+01	-0.76201695
3.92807800E-02	-7.29072200E-02	-2.03896400E-02	2.827435552E-03	1.951912881E-08	2.137565914E-90	1.215111482E-02	5.506240109E-07	5.293039482E-02	7.745542356E+00	-0.51243973
7.55344900E-02	-1.86473540E-01	-1.84915400E-02	9.539447166E-13	3.094707277E-13	1.273155865E-90	2.517816333E-02	3.540309591E-02	6.216119530E-02	1.257025098E+01	-0.8011867
3.40759900E-02	-1.60441400E-02	-5.56448000E-03	2.605399940E-02	6.790739006E-08	3.597394106E-89	2.673996867E-03	2.267067366E-07	1.380295687E-02	7.265093146E+00	-0.4658846
9.43656400E-02	-7.45056200E-02	-3.20579600E-02	5.711292367E-02	6.532823130E-08	9.460494838E-91	1.241757211E-02	2.526750131E-07	7.653349214E-02	7.317322257E+00	-0.49234275

Figure 2-19. Extract of the list of the batch calculations of the training data set.

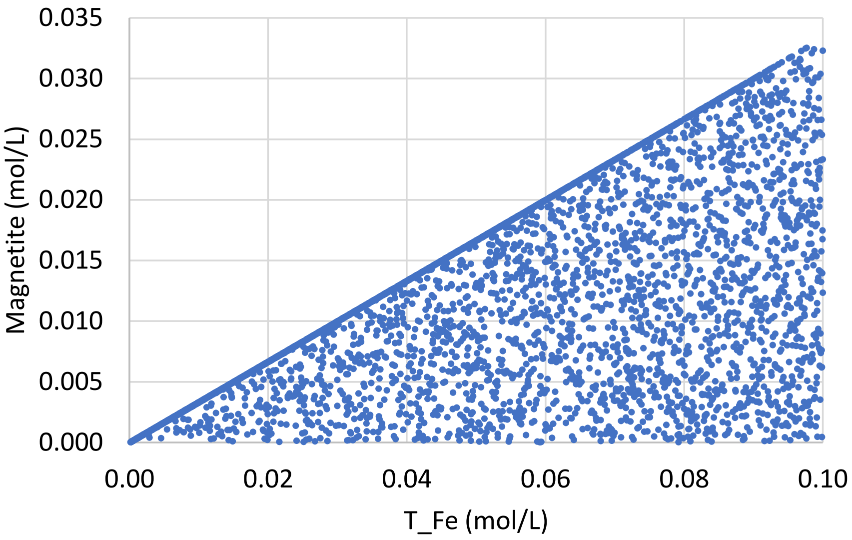

Figure 2-20. Scatter plot of the magnetite concentrations versus the total Fe concentration.

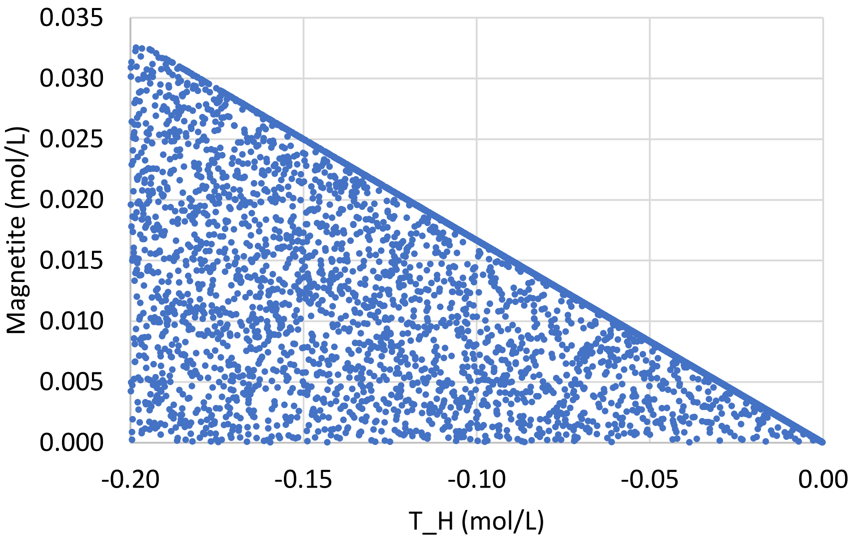

Figure 2-21. Scatter plot of the magnetite concentrations versus the total H concentration.

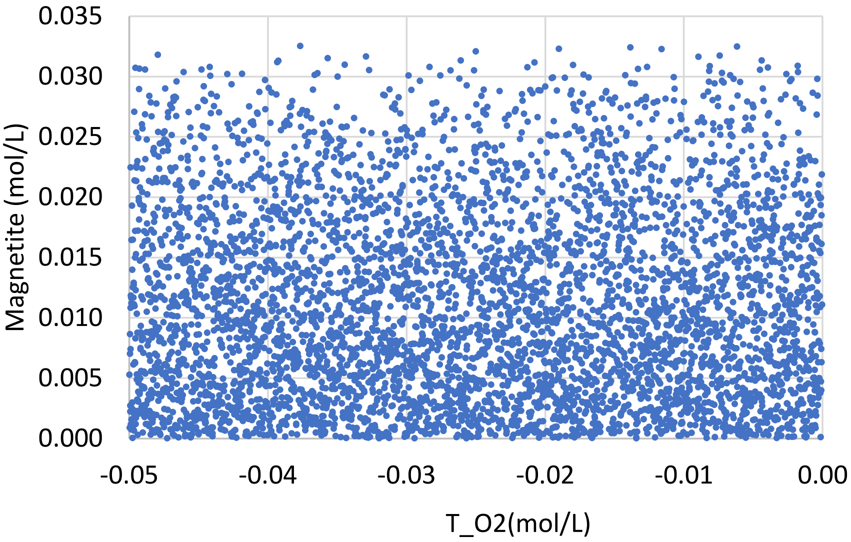

Figure 2-22. Scatter plot of the magnetite concentrations versus the total O_2 concentration.

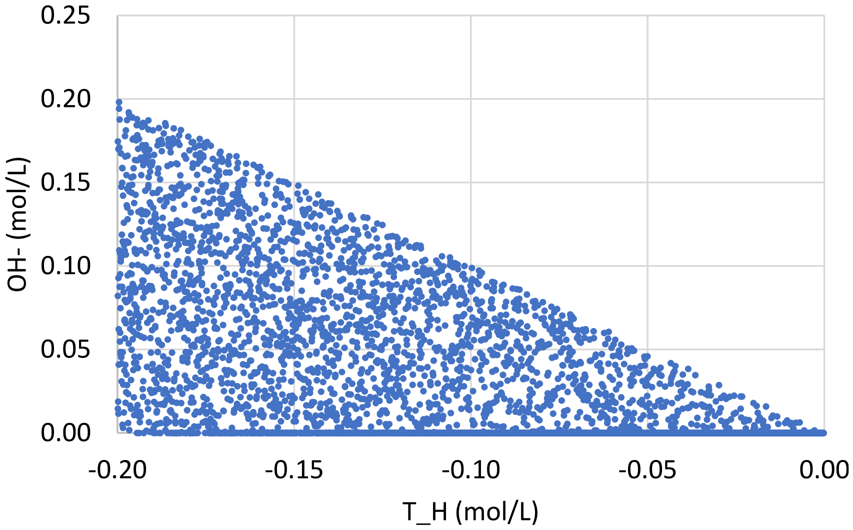

Figure 2-23. Scatter plot of the OH^- concentrations versus the total H concentration.

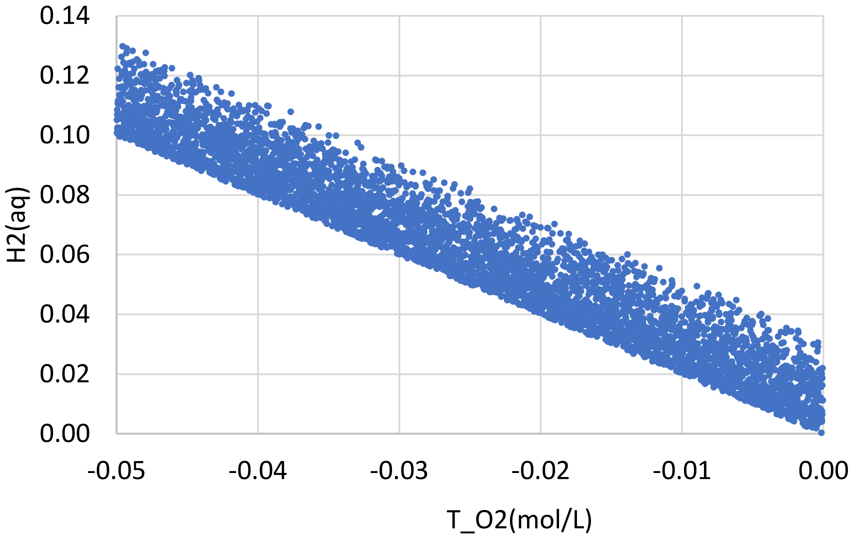

Figure 2-24. Scatter plot of the H_2(aq) concentrations versus the total O_2 concentration.

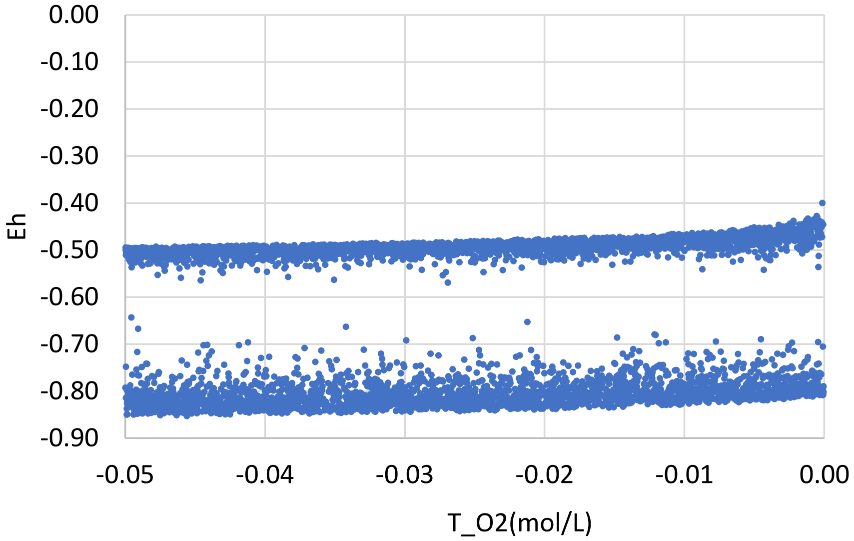

Figure 2-25. Scatter plot of the Eh concentrations versus the total O_2 concentration.

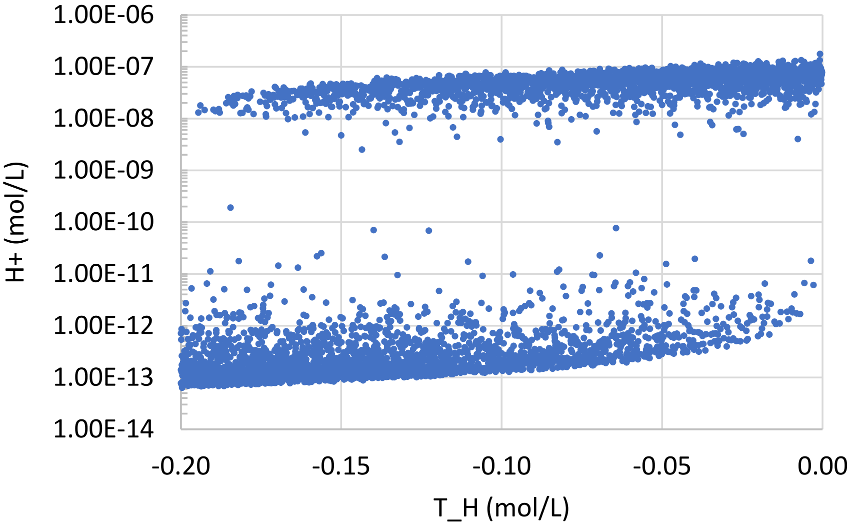

Figure 2-26. Scatter plot of the H^+ concentrations versus the total H^+ concentration.

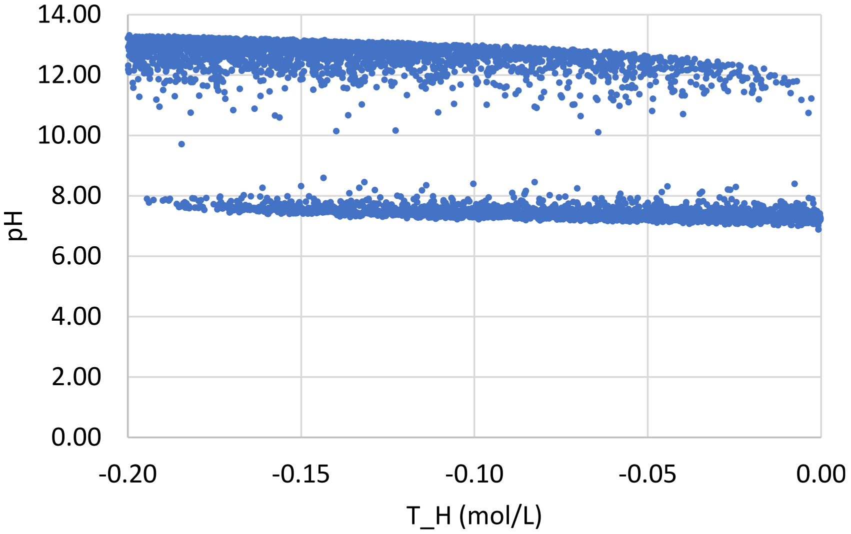

Figure 2-27. Scatter plot of the pH concentrations versus the total H concentration.

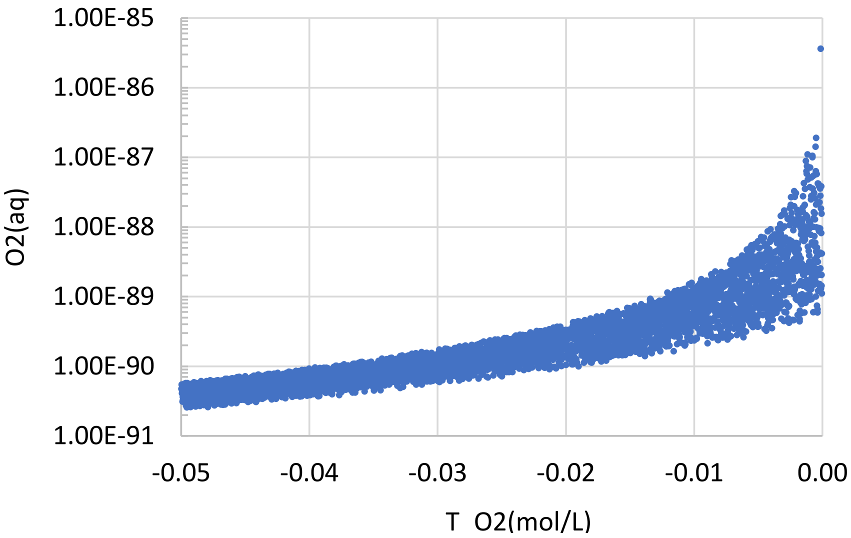

Figure 2-28. Scatter plot of the O_2 concentrations versus the total O_2 concentration.

2.4.3 Metamodel results

Gaussian Processes (GP) approach was adopted by UDC. GP are a generic supervised learning method designed to solve regression and probabilistic classification problems.

The advantages of Gaussian processes are:

1) The prediction interpolates the observations (at least for regular kernels).
2) The prediction is probabilistic (Gaussian) so that one can compute empirical confidence intervals and decide based on those if one should refit (online fitting, adaptive fitting) the prediction in some region of interest.
3) Versatile: different kernels can be specified. Common kernels are provided, but it is also possible to specify custom kernels.

The total data set of 5000 points was split into two groups of 2500 data points each. A set of 2,500 data was used to train the metamodel and the other 2,500 data to validate the metamodel. Splitting was performed by using a standard shuffle method. The random shuffle ensures that the division into training and validation sets is not biased. Data shuffling is a standard preprocessing method which improves model learning. Data shuffling is designed to counter potential issues arising from patterns in the sequential order of training samples, which can lead to overfitting. Furthermore, it mitigates the effects of significant imbalances or discrepancies in the distribution of different types of objects in the training and validation sets.

Table 2-3 shows the metrics of the results of the metamodel. These metrics were taken from Prasianakis et al. (2023; 2024) and are defined in Appendix A.

Figure 2-29 and Figure 2-30 show the scatter plots of the results of the GP metamodel results.

Table 2-3 – Metrics of the results of the metamodel.

Output	Conc. dissolved Fe	Conc. H	Conc. O2	Conc. mag	Conc. OH	Conc. H2	pH	Eh
MAE	$9.475 \cdot 10^{-4}$	$2.376 \cdot 10^{-9}$	$1.325 \cdot 10^{-89}$	$4.443 \cdot 10^{-6}$	$2.904 \cdot 10^{-5}$	$1.160 \cdot 10^{-5}$	$7.005 \cdot 10^{-2}$	$5.206 \cdot 10^{-3}$
MSE	$1.099 \cdot 10^{-4}$	$7.419 \cdot 10^{-17}$	$3.973 \cdot 10^{-175}$	$3.490 \cdot 10^{-10}$	$1.261 \cdot 10^{-8}$	$1.117 \cdot 10^{-9}$	$5.969 \cdot 10^{-2}$	$2.272 \cdot 10^{-4}$
RMSE	$1.048 \cdot 10^{-2}$	$8.613 \cdot 10^{-9}$	$6.303 \cdot 10^{-88}$	$1.868 \cdot 10^{-5}$	$1.123 \cdot 10^{-4}$	$3.343 \cdot 10^{-5}$	$2.443 \cdot 10^{-1}$	$1.507 \cdot 10^{-2}$
1-R2	$1.906 \cdot 10^{-1}$	$7.593 \cdot 10^{-2}$	$7.472 \cdot 10^{-1}$	$5.680 \cdot 10^{-6}$	$5.835 \cdot 10^{-6}$	$1.239 \cdot 10^{-6}$	$8.566 \cdot 10^{-3}$	$9.195 \cdot 10^{-3}$
NMAE	$9.697 \cdot 10^{-3}$	$1.331 \cdot 10^{-2}$	$3.642 \cdot 10^{-4}$	$1.367 \cdot 10^{-4}$	$1.523 \cdot 10^{-4}$	$8.961 \cdot 10^{-5}$	$1.095 \cdot 10^{-2}$	$1.153 \cdot 10^{-2}$

NRMSE	$1.073\cdot10^{-1}$	$4.825\cdot10^{-2}$	$1.733\cdot10^{-2}$	$5.746\cdot10^{-4}$	$5.890\cdot10^{-4}$	$2.582\cdot10^{-4}$	$3.819\cdot10^{-2}$	$3.337\cdot10^{-2}$
Normsupnorm	$1.685\cdot10^{-1}$	$4.958\cdot10^{-1}$	$8.663\cdot10^{-1}$	$7.518\cdot10^{-3}$	$6.521\cdot10^{-3}$	$3.306\cdot10^{-3}$	$3.222\cdot10^{-1}$	$4.043\cdot10^{-1}$
MAElog	$3.050\cdot10^{-1}$	$1.615\cdot10^{-1}$	5.011E-03	$7.634\cdot10^{-4}$	$4.494\cdot10^{-1}$	$3.021\cdot10^{-4}$	$7.748\cdot10^{-3}$	0.000
RMSElog	1.078	$5.634\cdot10^{-1}$	$4.335\cdot10^{-2}$	$4.410\cdot10^{-3}$	1.168	$2.554\cdot10^{-3}$	$2.667\cdot10^{-2}$	0.000
RMSLE	$9.132\cdot10^{-3}$	$8.613\cdot10^{-9}$	0.000	$1.834\cdot10^{-5}$	$1.122\cdot10^{-4}$	$3.090\cdot10^{-5}$	$2.400\cdot10^{-2}$	$4.156\cdot10^{-2}$
GMAQabs	1.357	1.175	1.005	1.001	1.567	1.000	1.008	1.000
MAPE	30.60	6.295	0.000	$7.650\cdot10^{-2}$	2332.0	$3.051\cdot10^{-2}$	$7.896\cdot10^{-1}$	$8.963\cdot10^{-1}$
RRMSE	4.833	$3.865\cdot10^{-1}$	0.000	$4.444\cdot10^{-3}$	121.3	$2.697\cdot10^{-3}$	$2.819\cdot10^{-2}$	$2.672\cdot10^{-2}$
NNEG	0.000	0.000	0.000	0.000	298.0	0.000	0.000	2500
Range	$9.771\cdot10^{-2}$	$1.785\cdot10^{-7}$	$3.637\cdot10^{-86}$	$3.251\cdot10^{-2}$	$1.907\cdot10^{-1}$	$1.295\cdot10^{-1}$	6.397	$4.516\cdot10^{-1}$

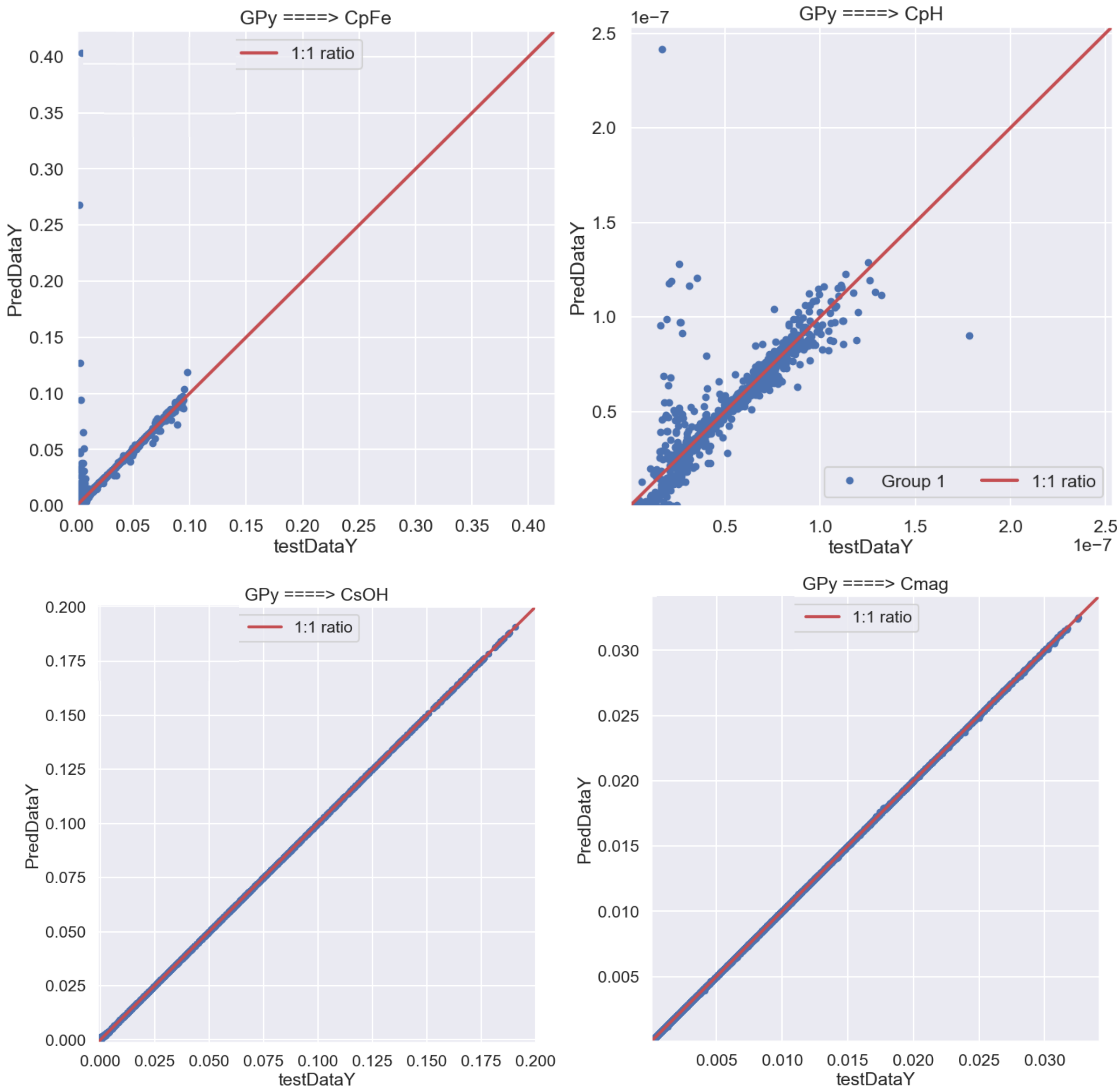

Figure 2-29. Scatter plot of the results of the GP metamodel results.

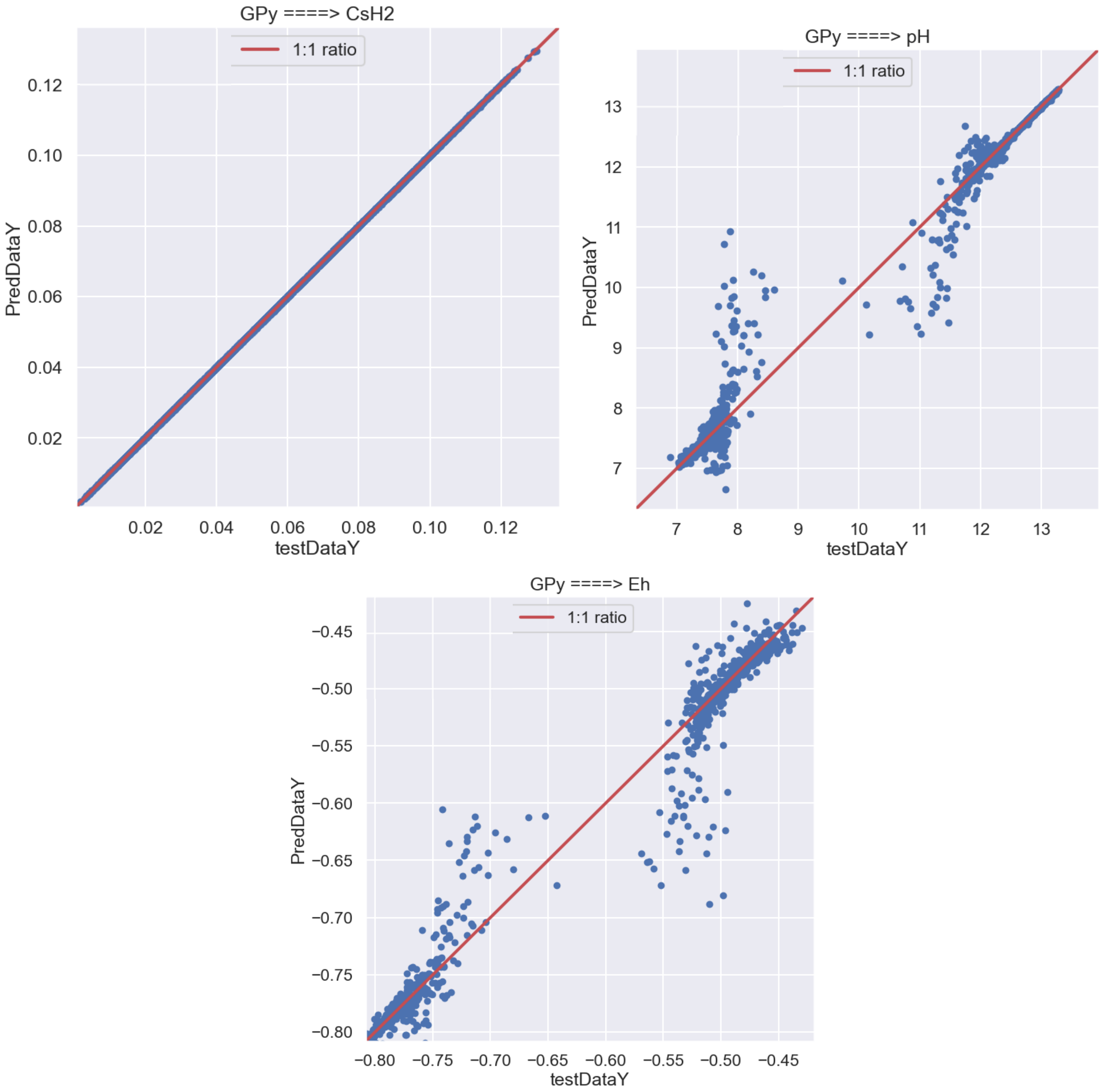

Figure 2-30. Scatter plot of the results of the GP metamodel results.

2.4.4 Performance of the metamodel

The metamodel provides excellent results for most of the output variables. Working with log for concentrations of H, OH and O_2 improves significantly the results for H and O_2, but leads to worse results for OH. When the metamodel is trained by working with concentrations of dissolved Fe, the validation results show some cases (617 out of 5000) with negative concentrations. On the other hand, when the metamodel is trained by working with the logarithm of the concentrations of dissolved Fe, the predicted validation concentrations are always positive, but the metrics of the validation are slightly worse.

The accuracy of the metamodel could be improved by: 1) Using a larger training data set and 2) Defining two groups, one for pH ≤ 9 and another for pH > 9.

The metamodel was improved by coupling a supervised Random Forest (RF) with Gaussian Processes. The supervised RF model is based on the definition of two groups. The groups are based on the following criteria:

1) Group 1: pH ≤ 9
2) Group 2: pH > 9

The supervised RF grouping for these two groups was trained with 2500 data points selected randomly with a shuffle method from the available data set. Input and output variables are used to train the RF. Therefore, pH training data are used to train the RF grouping. After the training, the RF is used to estimate the group of each data point in the validation data set. In this case, the estimation of the grouping is performed by using only the input variables.

The total data set of 5000 points was split into two groups of 2500 data points each. Splitting was performed by using a standard shuffle method. The random shuffle ensures that the division into training and validation sets is not biased. Data shuffling is a standard preprocessing method which improves model learning. Data shuffling is designed to counter potential issues arising from patterns in the sequential order of training samples, which can lead to overfitting. Furthermore, it mitigates the effects of significant imbalances or discrepancies in the distribution of different types of objects in the training and validation sets.

The results for two groups is shown in Figure 2-31. The performance of the metamodel improves significantly, although some small discrepancies remain in pH and Eh.

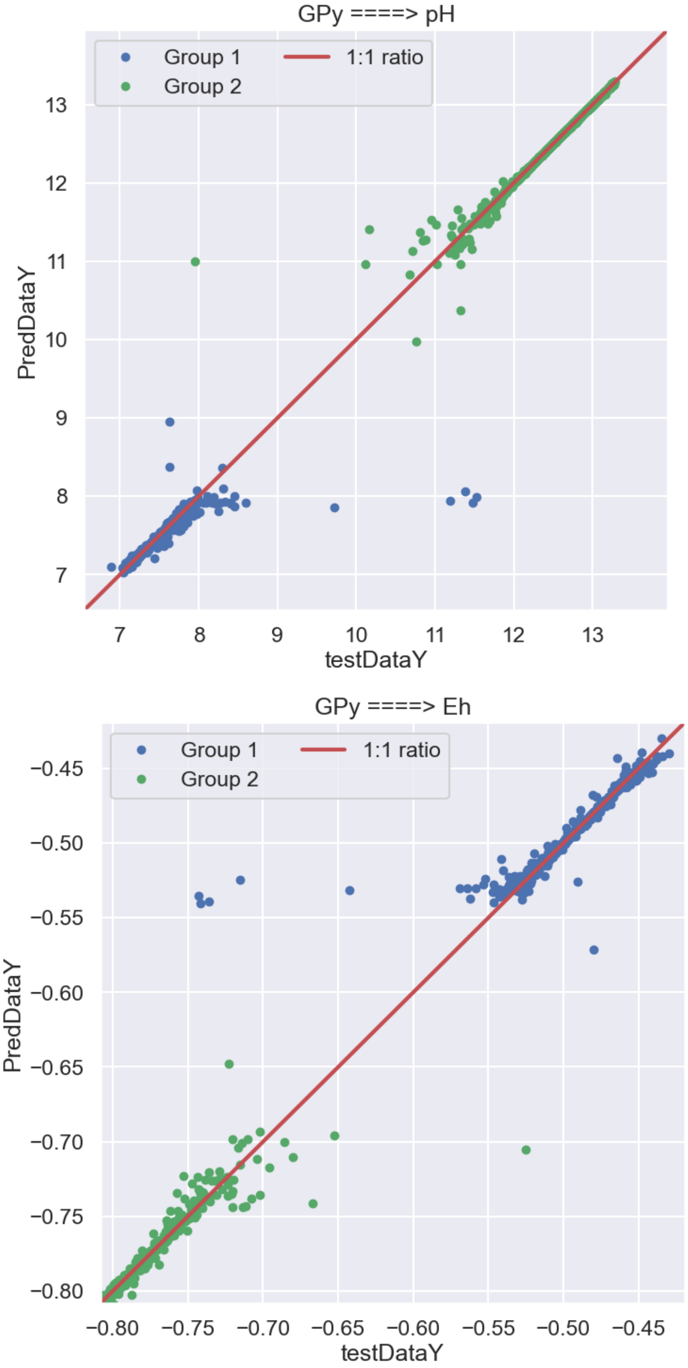

Figure 2-31. Scatter plot of the results of the GP metamodel results when the metamodel is constructed for two groups which correspond to pH ≤ 9 and pH > 9.

2.5 Sensitivity simulations

Several variants and sensitivity cases of the non-isothermal reactive transport model of the long-term geochemical evolution of a HLW disposal cell in a granite were performed and presented in D2.17 (De Windt et al., 2023) within the Subtask 4.1. In this Subtask 4.2 new sensitivity simulations were performed for the following parameters and assumptions: 1) A decrease in the threshold silica concentration in the kinetic glass dissolution rate; and 2) An earlier canister failure with a shorter duration of the canister corrosion period.

2.5.1 Sensitivity of the predictions to the silica saturation threshold

Sensitivity Case 1 aims at evaluating the sensitivity of the predictions to the silica saturation threshold, C_{Si}^*, used in the kinetic glass dissolution rate (Equation 2.7 in D2.17). The value used in the base case was 10^{-3} mol/L while in the sensitivity run was $5\cdot10^{-4}$ mol/L. A decrease in C_{Si}^* leads to a decrease in glass dissolution rate. The computed ISG glass dissolution at 50,000 years for $\mathrm{C}_{\mathrm{Si}}^* = 5\cdot10^{-4}$ mol/L is clearly smaller than that for $\mathrm{C}_{\mathrm{Si}}^* = 10^{-3}$ mol/L (Figure 2-32). The spatial distribution of the predicted pH, however, is not sensitive to the change in the silica saturation threshold (Figure 2-33). It can be concluded that the change in $\mathrm{C}_{\mathrm{Si}}^*$ leads to a change in the glass dissolution front, but it does not affect the computed pH.

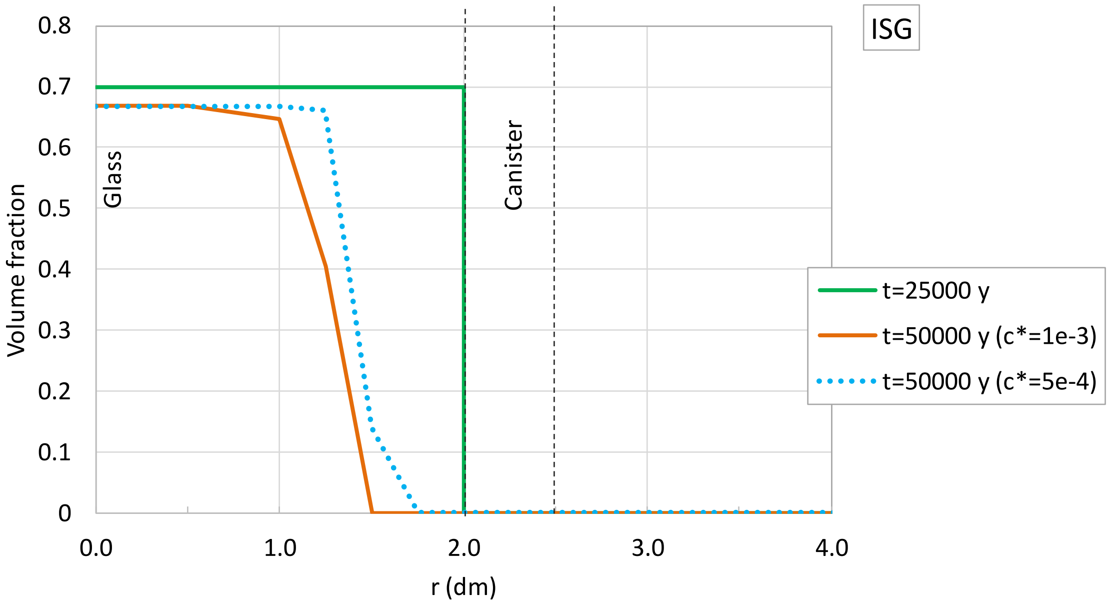

Figure 2-32. Spatial distribution of the computed volume fraction of ISG at selected times of Period III (50,000 years) for the base case and the sensitivity run.

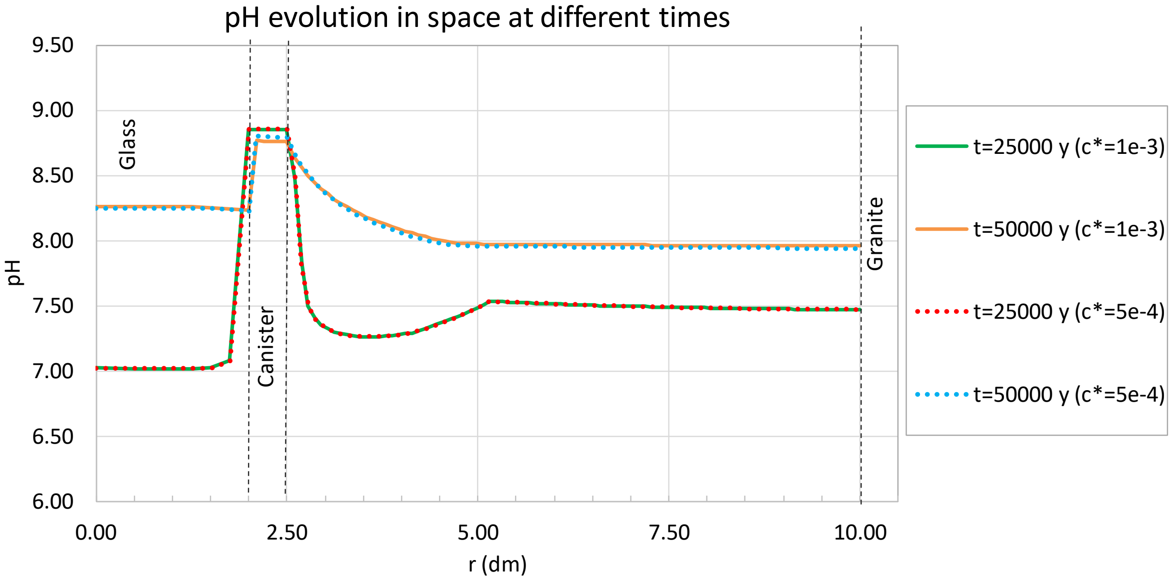

Figure 2-33. Spatial distribution of the computed pH at Periods II (25,000 years) and III (50,000 years) for the base case and the sensitivity run.

2.5.2 Earlier canister failure with a shorter duration of Period II

The base case presented in D2.17 (De Windt et al., 2023) within the Subtask 4.1 was based on the assumption that the canister fails when 70% of the canister is corroded after 25,000 years. Then, the dissolution of the ISG glass starts This sensitivity run considers an earlier canister failure with a shorter duration of Period II (canister corrosion). ISG glass dissolution is assumed to start after 10,000 years when 30% of the canister is corroded.

Shortening the duration of Period II from 25,000 years to 10,000 years has a significant impact in the ISG glass dissolution front after 50,000 years (Figure 2-34). The volume fraction of the precipitated corrosion products in the sensitivity run with an earlier canister failure and a shorter duration of Period II is smaller than in the base run because ISG glass dissolution causes greenalite precipitation instead of magnetite and siderite precipitation (Figure 2-35).

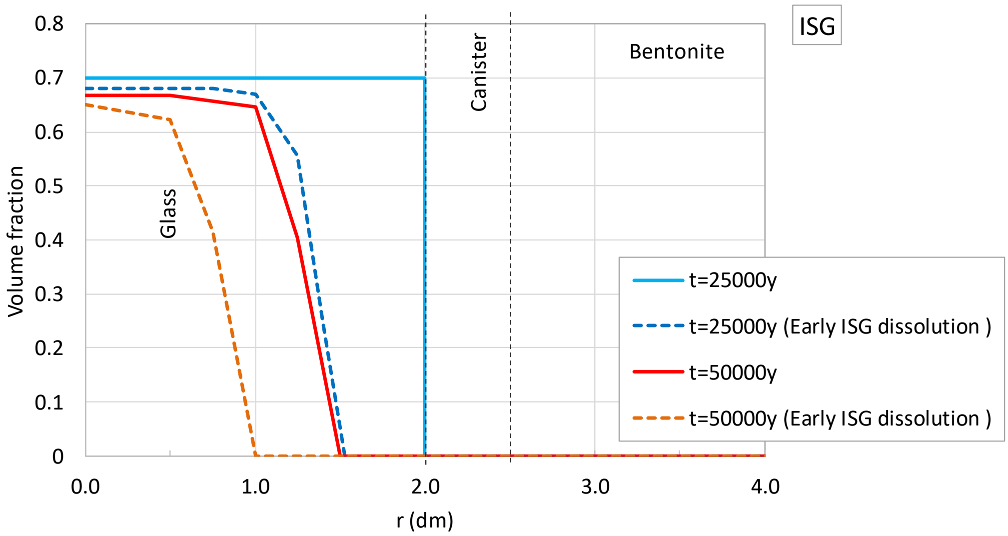

Figure 2-34. Spatial distribution of the computed volume fraction of ISG at 25,000 and 50,000 years in the base case and the sensitivity run with an earlier canister failure and a shorter duration of Period II.

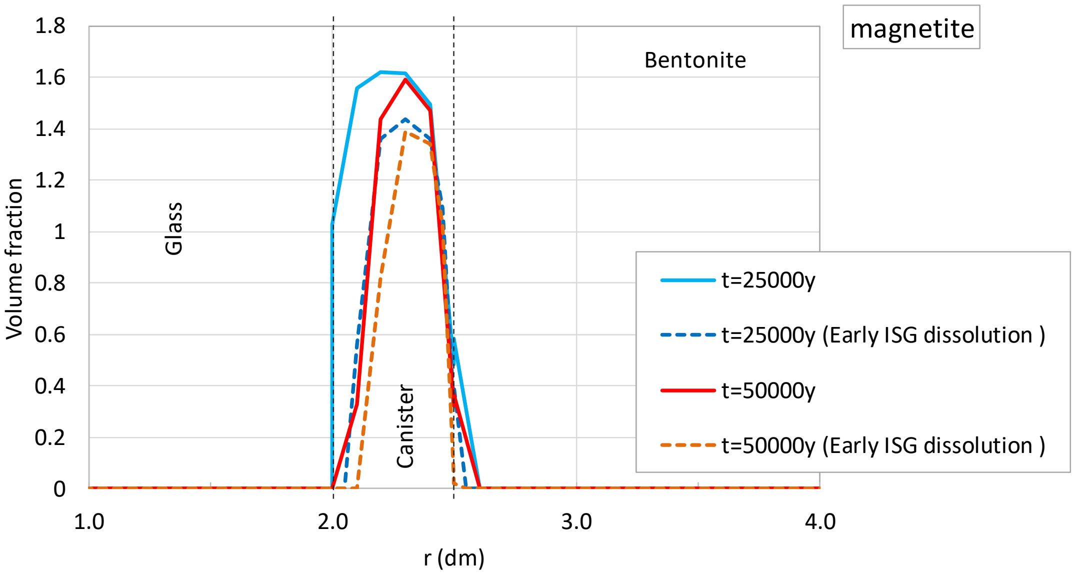

Figure 2-35. Spatial distribution of the computed volume fraction of magnetite at 25,000 and 50,000 years in the base case and the sensitivity run with an earlier canister failure and a shorter duration of Period II.

2.6 Conclusions

Model abstraction methodologies represent the complex interacting processes with more simple descriptions such as geometrical simplification, process simplification of equilibrium or kinetic processes, and look-up tables. To evaluate the results obtained from the lower fidelity models several runs have been performed: 1) Hierarchy of models (porosity feedback effect); 2) Delimited input domain (corrosion rate depending on temperature and saturation index; and reduced geochemical system) and; 3) Reduced numerical accuracy (mesh discretization and convergence tolerances).

The computed results are very sensitive to the porosity feedback effect. The porosity reaches the threshold porosity in the canister due to the precipitation of the corrosion products. Pore clogging prevents further precipitation and decreases solute diffusion coefficient. This in turn leads to sharp decrease of ISG dissolution.

The corrosion rate increases with increasing temperature and decreases with increasing pH and concentration of dissolved iron. A 80% volume fraction of Fe(s) remains uncorroded after 50,000 years when the corrosion rate assumed to depend on saturation index. The precipitation of corrosion products such as magnetite and siderite for variable corrosion rate is smaller than the precipitation for a constant corrosion rate.

A simulation run was performed in which smectite dissolution was neglected by considering smectite as an unreactive mineral phase to reduce the geochemical system. The general trends of the computed concentrations of dissolved, exchanged and sorbed species and mineral volume fractions are generally similar to the base case.

A simulation run was performed with a grid not refined near the interfaces. The general behaviour of the numerical results with the less refined mesh are similar to those of the base case. However, it is important to point out that with the refined mesh used in the base case: (1) The gradient results at the interfaces are better represented; and (2) The computing time increases almost 2 times.

Computed results for the convergence tolerances of $\varepsilon = 10^{-3}$ and 10^{-6} follow the same trend. However, considering the large tolerance could provide a lower fidelity solution, especially at the interface where there are the larger mineral precipitation/dissolution. On the other hand, the CPU time increases when the convergence tolerance decreases.

Additional sensitivity runs were performed to study the sensitivity of the predictions to the silica saturation threshold and to the earlier canister failure with a shorter duration of Period II. A decrease in the silica saturation threshold leads to a decrease in glass dissolution rate but it does not affect the computed pH. Shortening the duration of Period II from 25,000 years to 10,000 years has a significant impact in the ISG glass dissolution front after 50,000 years. The volume fraction of the precipitated corrosion products in the sensitivity run with an earlier canister failure and a shorter duration of Period II is smaller than in the base run because ISG glass dissolution causes greenalite precipitation instead of magnetite and siderite precipitation.

A metamodel has been developed for a simple geochemical system representative of the interactions of steel/bentonite and precipitation of corrosion products. The geochemical system includes 3 primary dissolved species (Fe^{2+}, H^+ and O_2(aq)), two aqueous complexes (OH^- and H_2(aq)) and a mineral (magnetite). The range of the total Fe concentrations was estimated from the canister corrosion in 50,000 years. A set of 5000 data were sampled with a Latin Hyper Cube (LHC) sequence for three variables. Then, batch simulations were performed with CORE^{2D}v5 for the 5000 combinations data of the total Fe, H and O_2. The following output data were obtained: 1) Aqueous primary concentrations: Fe^{2+}, H^+, O_2(aq); 2) Aqueous secondary concentrations: OH^-, H_2(aq); 3) Magnetite; 4) pH and 5) Eh. Gaussian Processes (GP) approach was adopted by UDC. 2500 data were used to train the metamodel and 2500 data were used to validate the metamodel. The metamodel is based on Gaussian Processes and Random Forests for defining two groups corresponding to high pH values (pH > 9) and lower pH values (pH ≤ 9). The metamodel provides excellent results for most of the output variables. Working with log for concentrations of H, OH and O_2 improves significantly the results for H and O_2, but leads to worse results for OH. When the metamodel is trained by working with concentrations of dissolved Fe, the validation results show some cases (617 out of 5000) with negative concentrations. On the other hand, when the metamodel is trained by working with the logarithm of the concentrations of dissolved Fe, the predicted validation concentrations are always positive, but the metrics of the validation are slightly worse. The accuracy of the metamodel is significantly improved for pH and by defining two groups, one for pH ≤ 9 and another for pH > 9.

3. Reference HLW disposal cell in clay

3.1 Short description of the reference HLW disposal cell in clay

The rather large discrepancies in the supercontainer and sleeve/liner concepts (see D2.16) did not facilitate the development of a common definition of a representative HLW disposal cell in a clay host rock. Therefore, a generic configuration of the HLW disposal cell in a clay host rock was set as a base case and variants were then applied to fulfil more explicitly one feature of the Belgian/Dutch concept or one feature of the French concept.

Figure 3-1 shows the initial state of the generic configuration of the HLW disposal cell in a clay host-rock:

1) The vitrified waste (40 cm in diameter) was explicitly considered in reactive transport modelling (not as boundary conditions) for coupling with the barriers and host-rock evolutions.
2) The overpack (5 cm thick) consisted of low alloy carbon-steel. A mechanical breaching was assumed when the non-corroded thickness reached 1.5 cm, allowing for the nuclear glass degradation to start. A technical gap of 1 cm thick was considered in contact with the overpack.
3) The cement-base buffer (30 cm thick in the base case, 5 or 100 cm in variants) was composed of Portland cement (CEM I) and calcareous aggregate without any reinforcement by steel structures.
4) The clay host rock (several meter thick in the calculations) was the French Callovo-Oxfordian (COx) claystone.

The modelling of the full HLW disposal cell in clay host rock without transient stage was performed with the reactive transport modelling code HYTEC (Van der Lee *et al*., 2003). All chemical reactions (aqueous, sorption and solid phases) were modelled at thermodynamic equilibrium, excepted for the clay phase dissolution, steel corrosion and nuclear glass dissolution that were modelled under kinetic constraints. The thermodynamic database of reference was ThermoChimie v10.a (Giffaut et al., 2014).

The detailed information on the material properties and reactive transport model can be found in the deliverable D2-17: Integrated reactive transport models for assessing the chemical evolution at the disposal cell scale (De Windt et al., 2023). This section only brings a few complementary sensitivity calculations to the main results developed in D2-17.

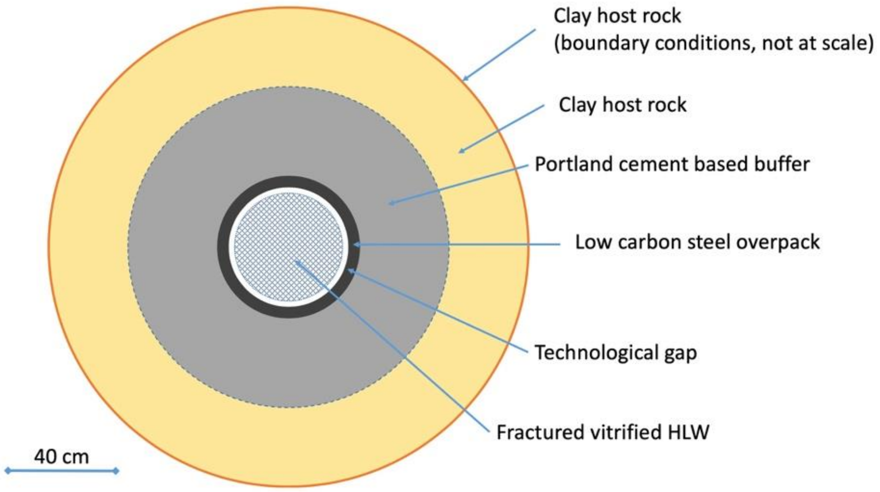

Figure 3-1. Initial geometry of the generic configuration of the HLW disposal cell in a clay host rock.

3.2 Sensitivity simulations

3.2.1 Chemical feedback on diffusion – clogging

The HYTEC modelling of D2-17 was performed under constant porosity. That is to say without chemical feedback effect on porosity and effective diffusion coefficient. This was an approximation of the reality. From the one hand, clogging at the cement/clay interface might rapidly stop any chemical degradation. From the other hand, decalcification might increase the porosity and D_e parameters, enhance the progression of the diffusion fronts and reduce the durability of the cement buffer.

The effect of the cement thickness cannot be separated from the evolution of the porosity and transport properties of the materials around the cement/clay interface. When the feedback effect of the mineral dissolution/precipitation was taken into account in the HYTEC modelling, clogging occurred at the cement/clay interface due to saponite, CASH and calcite precipitation. The porosity dropped, the diffusion coefficient strongly decreased (Figure 3-2) and the evolution of the system stopped after about only 1,000 years.

There was also a clear possibility of clogging of the steel overpack by the formation of corrosion products. Greenalite and, to a lesser extent magnetite, had indeed a much higher molal volume than the dense metallic Fe(0). Figure 3-3 shows the porosity calculated *a posteriori* from the volume fraction of the Fe-phases. A clear negative porosity is not physical and demonstrates that clogging would have occurred if the variable porosity had been considered in the HYTEC modelling.

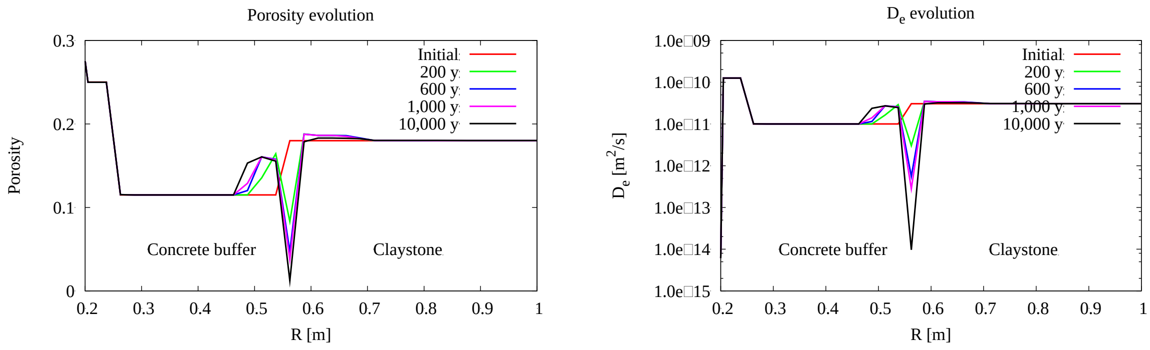

Figure 3-2. Sensitivity analysis – 30 cm CEM I buffer with variable porosity. *HYTEC modelling of the evolution of the porosity and diffusion coefficient at the concrete buffer and claystone interface taking into account the feedback effect of mineralogical change on the physical parameters.*

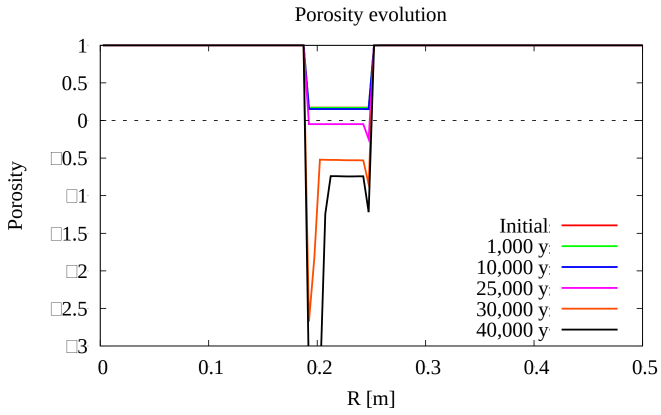

Figure 3-3. Base Case – 30 cm CEM I buffer. *Evolution of the porosity in the waste package and technological gap merged zone calculated from a HYTEC modelling performed without considering the feedback effect of mineralogical change on the physical parameters.*

3.2.2 Effect of cracks within the concrete buffer

Cracking of the concrete buffer might occur for mechanical and/or chemical perturbation. The ageing of cement, cement/clay interactions, or less likely expansive corrosion products of steel, may generate a few transversal cracks or a transversal network of interconnected cracks within the cement buffer (e.g. Craeye et al., 2009; Perko et al., 2015; Seetharam and Jacques, 2015). In that case diffusive mass transfers are enhanced and may accelerate the degradation of the buffer.

In a first approximation, the effective diffusion coefficient D_{eff} of the concrete buffer 10^{-11} m^2/s (base case, D2-17) was increased by about a factor 5 in the cracked state (this deliverable) within a representative elementary volume (REV) approach. This factor 5 corresponded to a pore diffusion coefficient of $5x10^{-11}$ m^2/s (to be compared to 10^{-9} m^2/s in pure water). It was thus realistic but arbitrarily set as a first sensitivity calculation that was feasible in the time allocated (most part of the effort was brought to D2-17). The degradation factor on the D_{eff} was chosen as a first trial. As a perspective, a larger set of effective diffusion coefficients could be tested. In addition, the fracture network could be either explicitly discretized in the modeling grid, or simulated in a dual porosity approach, as performed for instance in De Windt et al. (2007) for concrete monoliths.

HYTEC led to a similar sequence of chemical alteration of the cementitious buffer as in the other cases without cracks: in the concrete, moving fronts of decalcification of the cement phases, another front of secondary ettringite formation at the expense of monocarboaluminate dissolution of montmorillonite, in the host-rock partial illitization and neoformation of saponite and calcite. But cracking might significantly decrease the buffer lifetime. Table 3-1 assesses of the “durability” of the concrete buffer according to two indicators of durability already used in D2-17, i.e. the duration for high-pH buffering (that minimized steel corrosion) and the duration to reach C-S-H 0.8 (that altered the mechanical properties). For the reference thickness of 30 cm, the buffer lost its pH buffering capacity of portlandite after about 8,500 and less than 2,000 years for the base case and cracked concrete, respectively. The decalcification occurred after about 25,000 years in the base case but less than 6,000 years while assuming a cracked concrete.

Table 3-1. Duration indicators of the durability of the CEM I concrete buffer with respect to high-pH buffering and the completion of decalcification, calculated for different hypothesis on the concrete buffer state.

Cementitious buffer: **thickness – modeling assumption**	**Full portlandite dissolution** **(pH ≤ 12)**	**Advanced decalcification** **CSH 0.8 (pH ~ 10)**
30 cm – constant porosity	8,500 y	~ 25,000 y
30 cm – variable porosity	Never, clogging < 2,000 y	Never
30 cm – cracked	~ 2,000 y	~ 6,000 y
100 cm – constant porosity	82,000 y	> 100,000 y

3.2.3 Number of discretized C-S-H phases

Not shown in this report, HYTEC modelling made on the sub-system concrete buffer/claystone indicated that the reduced set of 3 C-S-H led to similar results than those obtained with an extended set of 9 C-S-H. The smaller set was then kept in D2-17 for the sake of simplicity.

3.3 Conclusions

Sensitivity calculations with respect to the effective diffusion coefficient of the concrete buffer were performed with HYTEC. A higher diffusion coefficient induced by cracking led to a similar sequence of chemical alteration of the cementitious buffer as calculated in the base cases but would significantly decrease the buffer lifetime. On the contrary, much lower diffusion coefficients were calculated over time due to clogging at the cement/clay interface by secondary cement phases as well as in the steel overpack by the formation of corrosion products, which should increase the buffer lifetime.

4. Reference ILW disposal cell in clay

4.1 Short description of the ILW disposal cell in clay

4.1.1 General model description

Figure 4-1a illustrates the overall cross-section of a general ILW repository model adopted by UFZ. The model domain represents a gallery constructed in the clay host-rock. The dimensions of the gallery are following a general concept proposed by Nagra (2016). There are a couple of waste containers stacked in a 3-level structure inside of the repository. Two types of waste containers are considered in the model.

1) The container with metal waste, marked with red color in Figure 4-1b. Each container is filled with 6640 kg of carbon steel waste. The steel surface area is 0.064 m^2/kg (Wieland et al. 2018) leading to a surface area per volume of 127 m^2/m^3. Considering the thickness of the concrete wall in the 3rd dimension and converting it to 2D, a conversion factor of 0.75 is introduced into the numerical model and is multiplied with the steel surface area and applied on the 2D surface area of the metal waste. The steel corrosion rate is set to 0.02 µm per year leading to a H_2 gas production of 0.00375 mol/(m^2a) when pH is higher than 10.5 (Huang et al 2021). If the pH value is below 10.5 the corrosion rate increases to 2 µm per year. This pH dependent corrosion rate is adopted from Wieland et al. (2020), which is also used in Huang et al. (2021).
2) The other type of container is filled with the organic waste (marked with orange color in Figure 4-1b), which is stored in multiple drums. As already described in D2.16, the waste drums are further organized in a 2x3x2 layout in the container (see Figure 4-2), with the surrounding space filled with mortar. Here in the large-scale model, the difference in comparison to the smaller scale model used in D2.16 is that the inner metal tube placed in the D2.16 model has been removed. For accounting the correct amount of organic waste in the third dimension, we have calculated a smaller drum area of 0.374 m x 0.545 m and a waste area of 0.299 m x 0.436 m, considering a distance between the container mid-point of 2 m in the third dimension. After the removal of the inner tube, there is no metal waste inside of the drums (see Table 4-1). The reduction in total metal quantity is negligible, considering the large amount of metal waste placed in the other type of containers. But still, the model considers H_2 production from the corrosion of the drum metal hull.

Outside of the gallery wall, an excavation-damage-zone (EDZ) is also reflected in the model domain, which is located between the concrete liner and the clay host rock. The entire gallery will be equipped with a concrete liner (light gray color in Figure 4-1b). Between the waste container and the concrete liner, a special M1 mortar is introduced (blue color in Figure 4-1). It has a relatively higher porosity value, with the intention to give more volume to host the gas produced by the degradation and corrosion reactions. The high porosity of the M1 mortar goes along with a high permeability, allowing the gas to move to the top of the gallery. Similar to the configuration of the organic waste containers, the void space between the containers is again filled with the same mortar material.

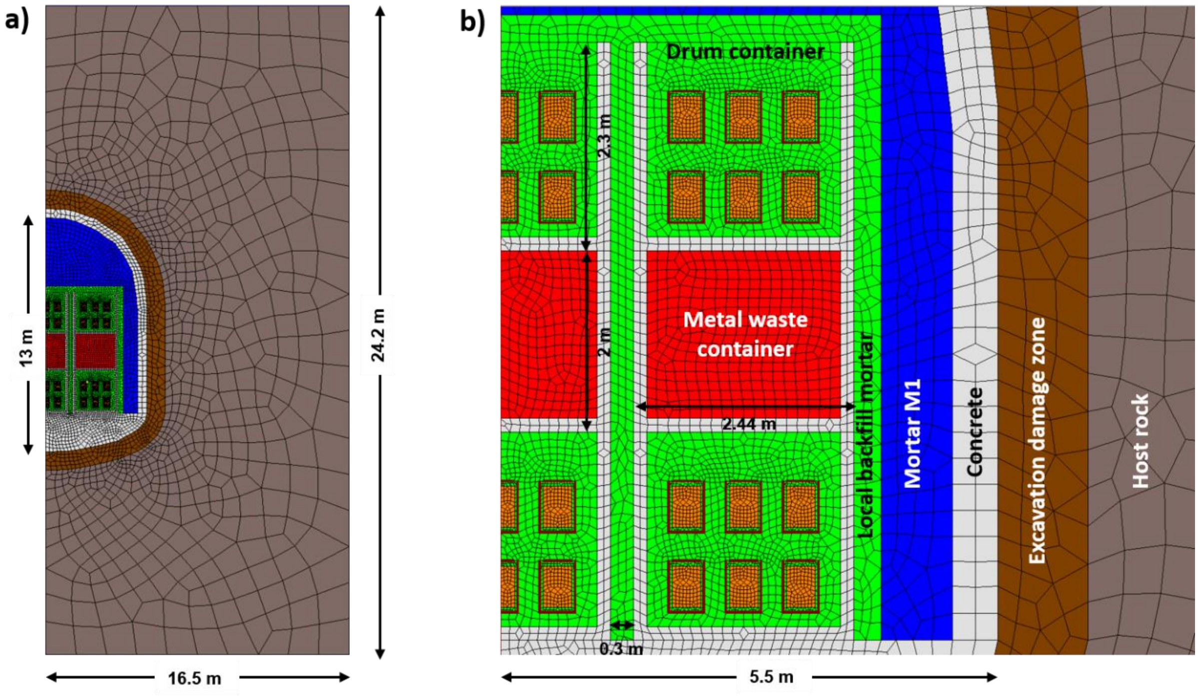

Figure 4-1: a) Domain and discretization of the gallery model. Description of the disposal concept and design is reported in D2.16 Conceptual model formulation; b) Zoom-in view on the cross section of the gallery model. Brown lines show the metal hull of the drums and waste areas are shown in orange.

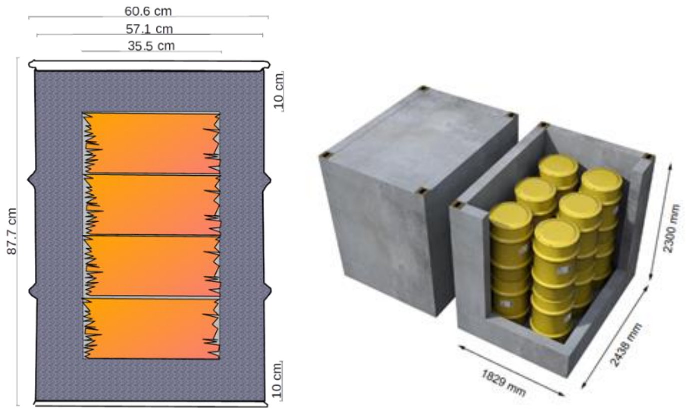

Figure 4-2: Schematic sketch of the generic waste package. Organic waste (orange) with local back fill mortar (grey) (ACED_T3.3 Deliverable 2.15).

Table 4-1. Content of organic waste drum, degradation parameters, gas generation rates and rates for water consumption for two waste groups from Huang et al (2021).

Symbol	Unit	Group 1 (Cellulose)	Group 2 (Polysterene)	Reference
m(t=0)	kg	30.6	65.3	This Study (in comparison to the model of Huang et al 2021 the metal waste is emplaced by organic waste)
Mass per volume waste	kg/m³	234	500	waste per m³ in waste area
λ	a^{-1}	$1.89 \cdot 10^{-3}$	$6.51 \cdot 10^{-5}$	Wieland et al 2018, Wieland et al 2020
k_D	mol kg^{-1} a^{-1}	0.07	0.005	Leupin et al 2016
Rate for CO_2	mol kg^{-1} a^{-1}	$k_D \cdot 3/6$	$k_D \cdot 3/8$	Huang et al 2021
Rate for CH_4	mol kg^{-1} a^{-1}	$k_D \cdot 3/6$	$k_D \cdot 5/8$	Huang et al 2021
Rate for water consumption	mol kg^{-1} a^{-1}	$k_D \cdot 1/6$	$k_D \cdot 6/8$	Huang et al 2021

Table 4-2. Hydraulic properties used in the gallery model.

Parameter	Symbol	Unit	Local back fill Mortar	Waste matrix	Host rock (Clay)	EDZ	Mortar1**	Concrete
Intrinsic permeability	k	m²	1e-19	1e-16	4e-20	5e-18	1e-12	5e-19
Porosity	Φ	-	0.076*	0.2	0.18	0.18	0.3	0.2
Residual saturation	S_L^{rel}	-	0.2	0.2	0.4	0.2	0.3	0.2
van Genuchten characteristic (entry) pressure	p_d	Pa	1e6	1e4	4e6	2e6	5e2	1e6
van Genuchten parameter	m	-	0.36	0.5	0.4	0.4	0.5	0.5

* Local back fill mortar porosity changes with cement carbonation and alkali silica reaction (ASR)
** no mortar degradation

In the model configuration, the initial liquid saturation is given with different values for different materials. More specifically, the back fill mortar is considered to have an initial saturation of 0.996, reflecting the fact that there is enough water available after the hydration process. The organic waste was assumed to have an initial saturation of 0.33, similar as the configuration in D2.16. The clay host-rock has an initial water saturation of 1. On the pressure side, the initial gas pressure in the gallery is set to 5 MPa. This reflects the hydro-static pressure at 500 m depth below subsurface, and it is also linearly increasing following the hydrostatic pressure gradient. At the domain boundary, a capillary pressure of 0 Pa is set in the model, suggesting that the clay rock at the far-field is fully saturated.

4.1.2 Two-phase multi-phase multi-component model

In order to investigate the controlling factors of the gas production process, the coupled reactive transport model of component based two-phase flow module in the OpenGeoSys (OGS) framework is adopted here. A detailed description of the reactive transport model can be found in Huang et al. (2021). Here in this report, a brief summary of the model is also provided.

For the two-phase module in OGS, the standard Galerkin finite element (FE) method is employed for spatial discretization with a fully implicit backward Euler scheme for the time integration. The concrete, mortar and waste are implemented as porous and permeable medium with two mobile phases, gas and liquid. The gas components are water vapour, nitrogen, methane, hydrogen and CO_2 and can dissolve into the water dominated liquid phase. As mass transport model the generalized Darcy law is implemented in combination with diffusive transport given by Fick's law:

$$\frac{\partial}{\partial t}\sum_{\alpha\epsilon\{\mathrm{G,L}\}}(N_\alpha S_\alpha x_\alpha^i)+\nabla\left[\sum_{\alpha\epsilon\{\mathrm{G,L}\}}N_\alpha(x_\alpha^i\boldsymbol{q}_\alpha+\boldsymbol{J}_\alpha^i)\right]=F^i \tag{4-1}$$

Where α denotes the gas phase G or the liquid phase L, x is the molar fraction of component i in phase α, S_α is the saturation of phase α, and N_α represents the phase molar density. F^i is a source or a sink term for each component. The Darcy law is given as:

$$\boldsymbol{q}_\alpha=-\frac{kk_\alpha^{\mathrm{rel}}}{\mu_\alpha}(\nabla p_\alpha-\rho_\alpha\boldsymbol{g}) \tag{4-2}$$

Here ρ_α is the phase density and p_α is the phase pressure. The diffusive flux $\boldsymbol{J}_\alpha^i$ is obtained by Fick`s law:

$$\boldsymbol{J}_\alpha^i=-D_{\mathrm{e}}\nabla x_\alpha^i \tag{4-3}$$

where the effective diffusion coefficient D_e is defined as $D_e = \Phi \cdot S_\alpha \cdot D_\alpha$. Here Φ denotes the material porosity and D_α is the diffusion coefficient of i in phase α. For unsaturated conditions the capillary pressure p_c has to be takin into account and is obtained by the van Genuchten model:

$$p_{\mathrm{L}}=p_{\mathrm{G}}-p_{\mathrm{c}} \tag{4-4}$$

$$p_{\mathrm{c}}(S_{\mathrm{L}}^{\mathrm{eff}})=p_{\mathrm{d}}\left((S_{\mathrm{L}}^{\mathrm{eff}})^{\frac{-1}{m}}-1\right)^{\frac{1}{n}} \tag{4-5}$$

Here $m = 1 - 1/n$ and n are the van Genuchten parameters and p_d is the characteristic van Genuchten pressure. The effective saturation S_L^{eff} is given by

$$S_{\mathrm{L}}^{\mathrm{eff}}=\frac{S_{\mathrm{L}}-S_{\mathrm{L}}^{\mathrm{res}}}{1-S_{\mathrm{L}}^{\mathrm{res}}-S_{\mathrm{G}}^{\mathrm{res}}} \tag{4-6}$$

4.2 Relevant output variables

4.2.1 Gas production

The numerical model simulations reveals distinctive gas production processes in containers filled with metal or organic waste. In the metal-filled containers, where the void space between the metal is cemented, simulated pH values remains around 13 during the entire 500 years simulation time. As the pH is relatively high, there is barely any hydrogen producing corrosion of the metal observed. Because of the high saturation condition in container, Alkaline-Silica-Reactions are happening with the consumption of water. However, due to the low reaction rate of ASR, there is no observable impact on the liquid saturation and pH in the container. Due to the presence of high pH value, the molar gas production rate inside of the metal containers is one order of magnitude lower than those inside the drum containers. Therefore, there is only negligible contribution of gas production from the metal container. However, as ASR is a very slow process, given long enough time, it may cause the pH in the container to drop below 10.5, which may further lead to a completely different metal corrosion rate. Yet, this process is not seen in the current simulation, which only covers the first 500 years.

In contrast, the process in the drum is completely different. Here, the cellulose degradation (fast degradation organics) becomes the main source of CO_2 production. Despite of the high CO_2 production rate in the first 500 years, most of the CO_2 produced in the drum moves upwards to the top of the drum and then participates in the carbonation reactions with the mortar there. This caused a continuous reduction of pH of the mortar progressing towards the top part of the metal hull. At the same time, methane is being produced by the fast degrading organics at the same rate. As there are no local reactions holding it, the methane gas will gradually leave the waste drum (see Figure 4-3b). The gas generation rates are decreasing with a minimal rate because the degradation rate drops along with less amount of degradable organic waste. In comparison to the metal container, the pH value at the top of the drum is dropping due to the cement carbonation reactions, it is approaching 10.5 after about 320 years. This then triggers the fast corrosion of the drum metal lid, leading to an increase in the hydrogen production observed in Figure 4-3b. After 500 years the hydrogen and methane fluxes are equal indicating an equal gas production rate for both gases.

4.2.2 Gas and liquid flux at a drum opening and liquid saturation inside of a drum

At the beginning, the mortar inside of the drum and in the container are close to be fully saturated. Therefore, the relative gas permeability of the mortar is very low. Therefore, the produced gases lead to a strong gas pressure increase that leads first to a strong increase of the liquid flux out of the drum (Figure 4-3b). The gas flux is then increasing with increasing gas saturation, having the peak gas flux after 30 years. The initial decrease of liquid saturation leads to an increase of capillary pressure of 0.2 MPa, which reduces the liquid flow out of the drum significantly (Figure 4-3b and d).

After this initial period, the flow regime is then heading to relative stable mode, which lasts between 200 and 300 years. The reason is that there is enough water available to feed the outflow of liquids and the water consuming organic degradation, which is continuously reducing the initial liquid saturation in the mortar and waste. The liquid flow regime is then disturbed by the water consuming steel corrosion leading to a reversal of the liquid flow into the drum. After 450 years the hydrogen production rate and therefore the water consumption become nearly constant. But this does not lead to a constant liquid flow into the drum, because at the same time the liquid saturation of the waste could not be depleted anymore for feeding the organic degradation. It has reached the residual value of 0.2, where the liquids become immobile and chemical reactivity drops. Later than 500 years, a flow regime will be established where the water flux into the drum has to match the water consumption rate of the chemical reaction rate, which will probably decrease due to a decrease of chemical reactivity.

4.2.3 Gas pressure and gas flux at the gallery scale

As the time goes along, the high-pressure zone gradually extends from the containers to the outer spheres of the gallery, and also into the host rock. Driven by the pressure gradient, the produced gas is moving outwards into the clay host rock, as well as moving upwards due to the density effect (see Figure 4-4, e and f). In comparison to the simulation results in a smaller scale reported in D2.15, a distinctive feature in the larger gallery model is the influence of the M1 mortar. From the lower and middle containers, the produced gases are mostly transported horizontally into the M1 mortar using the easiest conduit to the high permeable M1 mortar. Here the gases can easily move upwards into the gallery roof, where the M1 Mortar is designed as intermediate gas storage. In Figure 4-4a, it can be observed that gas moves faster in the M1 mortar zone (indicated by red arrows). This is also reflected in the 25 and 50 years' results (Figure 4-4c and d). From the upper containers the gas is directly moving upwards into the M1 mortar. After 160 years the gas pressure has increased in total by 0.6 MPa and is slowly increasing further because of the fixed pressure boundary condition. Here a larger modeling area would lead to higher gas pressures within the gallery, especially when the hydrogen gas production of the drums starts to increase.

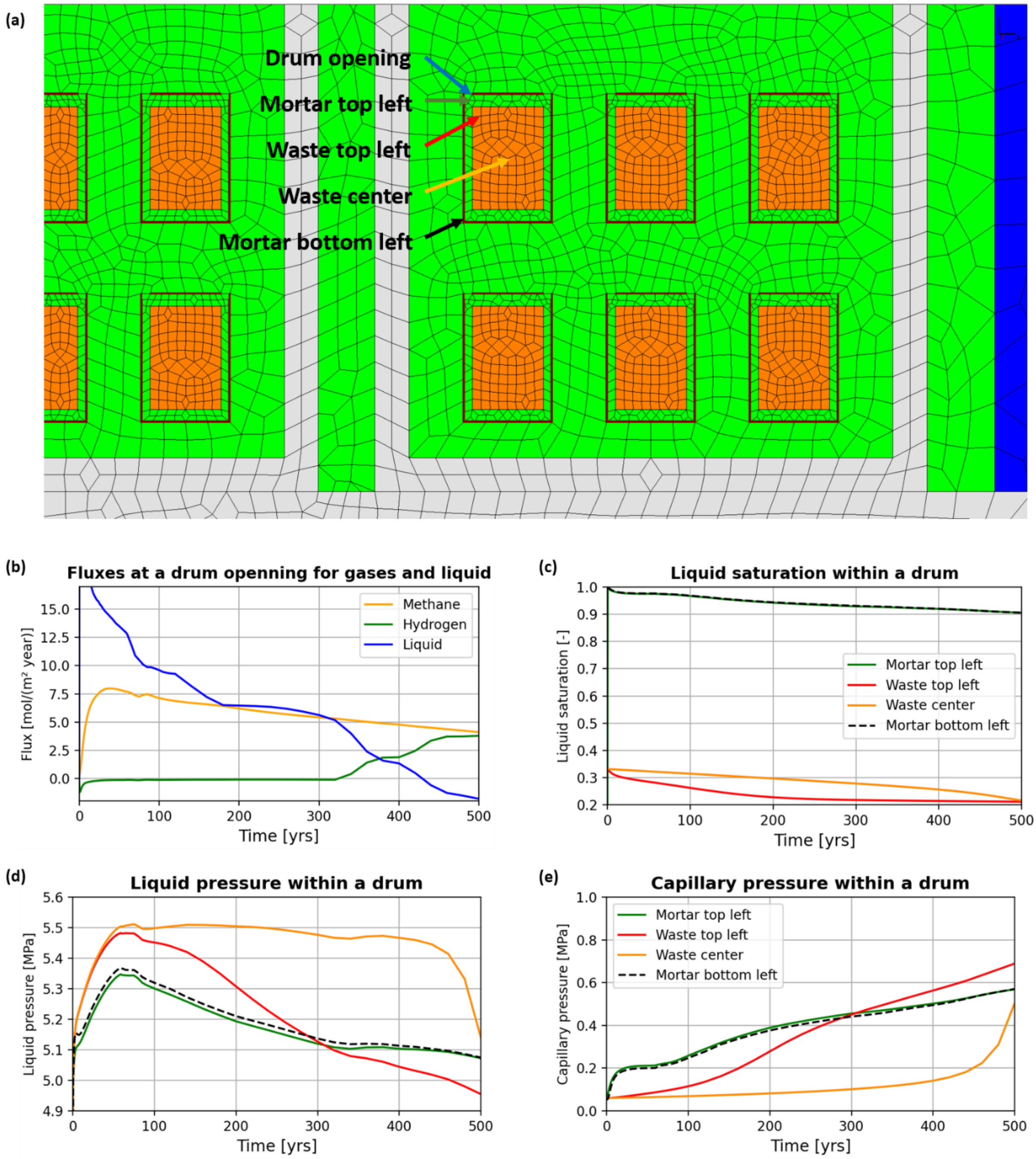

Figure 4-3: Time series plots showing the hydrological evolution of the upper left drum in the lower right container. Panel (a) shows the location of mesh nodes corresponding to the time plots. Panel (a) show gas fluxes (methane and hydrogen) and liquid flux out of the upper left drum in the lower right container. Displayed gas flux is the sum of diffusive and advective flux. Negative values indicate fluid flow into the drum. Panel (c) shows liquid saturation, (d) liquid pressure and (e) capillary pressure.

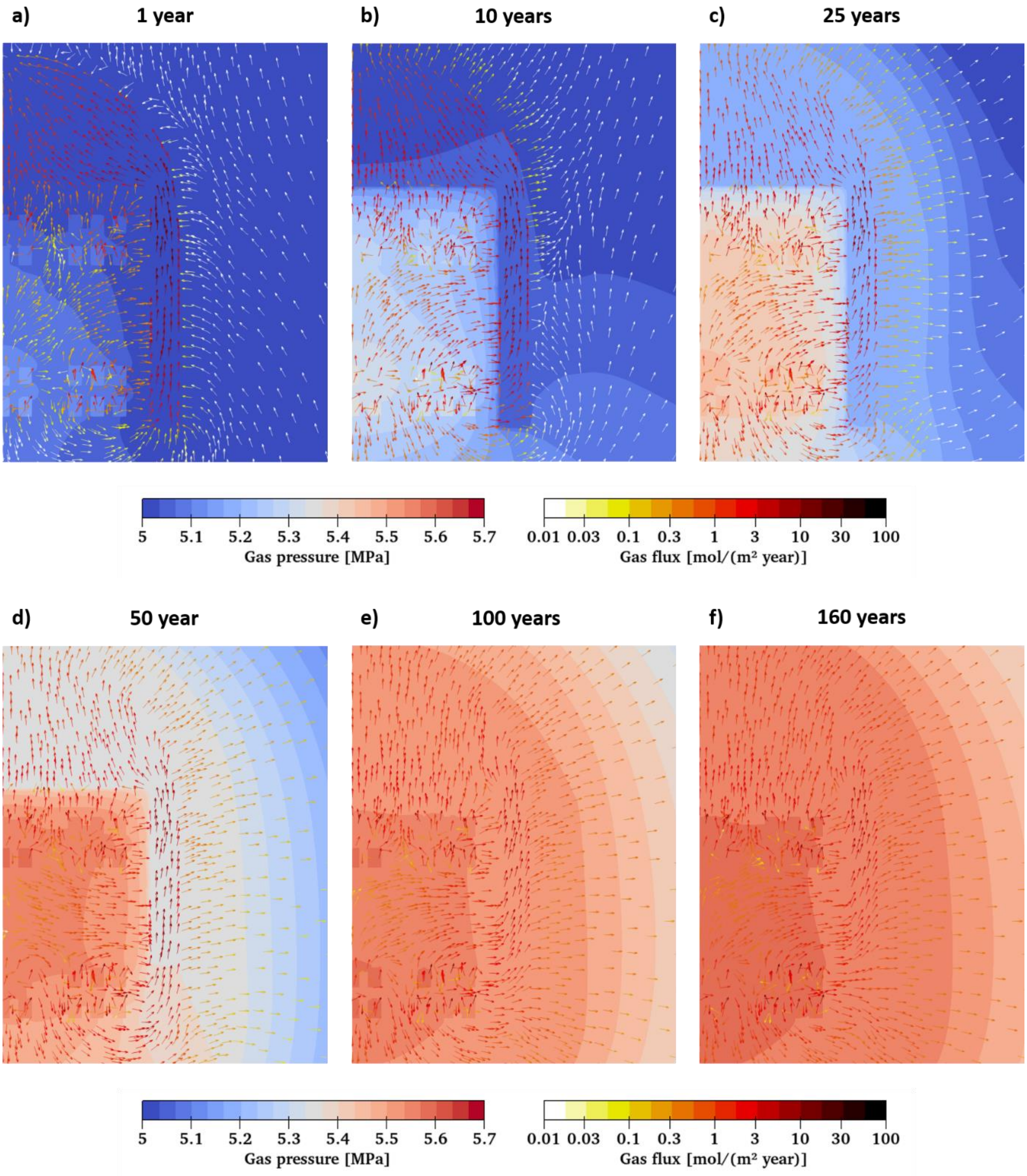

Figure 4-4: Gas pressure (colored legend) and gas flux (arrows) after 1, 10, 25, 50, 100 and 160 years of model simulation.

4.2.4 Capillary pressure and liquid flux at gallery scale

The hydrological material parameters have a high impact on the liquid flow field. The van Genuchten characteristic entry pressure of the local back fill mortar is four orders of magnitude higher than the value for the M1 mortar. This has the effect that the local back fill mortar will hold the pore water due to the high capillary effect. Due to the initial gas pressure increase the liquids of the container area (back-fill mortar) are flowing upward and sideward into the M1 mortar which is shown in Figure 4-5a and *b*. At the upper M1 mortar they stay fixed because of the gravity and at the sideward M1 mortar they can move downwards. At the low part of the gallery the liquids are pushed downwards to the mesh boundary.

After 25 years (see Figure 4-5c), the liquid flux in the upper container area has significantly decreased and the direction has changed downwards. The reason is that the gas pressure is not high enough to overcome the gravity effect and the capillary pressure. After 50 years the liquids, which were pushed into M1 mortar before, are sucked into the container area due to the increased capillary pressure and the increased gas pressure of the M1 mortar.

After 160 years the liquid saturation at the lower containers have decreased to 0.9 and is higher than at the upper containers (Figure 4-6c). The reason is that the gas pressure gradient at the upper containers slows down the liquid flow downwards.

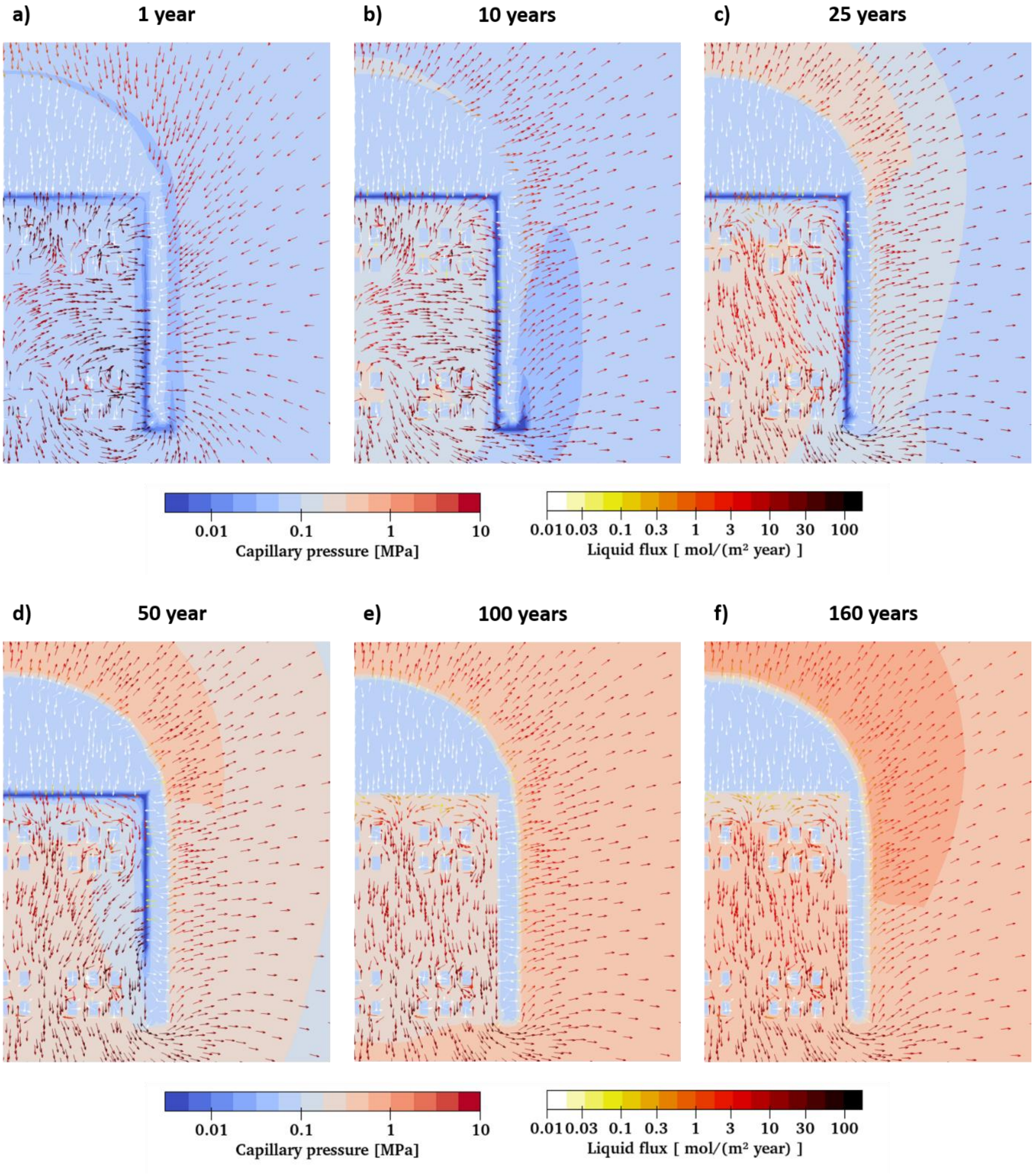

Figure 4-5: Capillary pressure (colored legend) and liquid flux (arrows) after 1, 10, 25, 50, 100 and 160 years of model simulation.

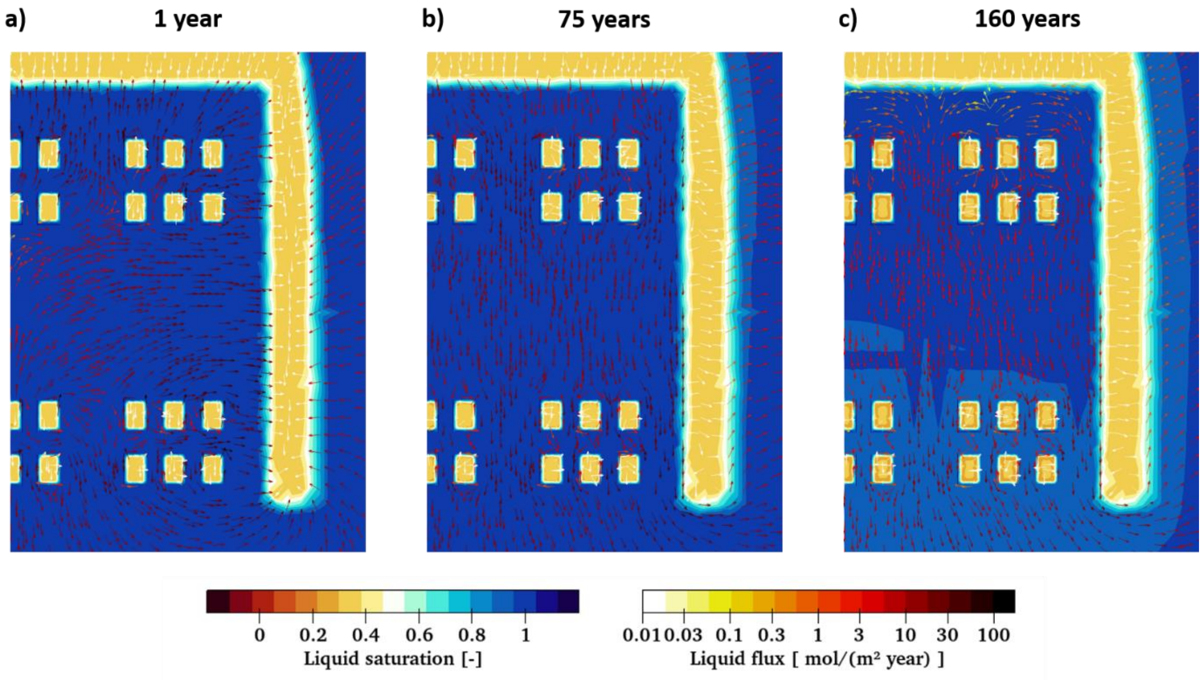

Figure 4-6: Liquid saturation (colored legend) and liquid flux (arrows) after 1, 75 and 160 years of model simulation.

4.3 Summary

In this study we found that the difference of the drum model, which is introduced and studied in D2.15, in comparison with this drum model here, leads to significant differences in gas generation rates for the first 50 years. The emplacement of the metal waste part with organic waste, i.e. increased amount of fast degrading cellulose, increases the methane and CO_2 production rate, but as the cement carbonation reaction consumes the CO_2 and releases water, the water is than available for further degradation of organics. As the fast corroding metal tube and the metal waste inside of the drum is missing in this study, the overall net water consumption rate is much lower leading to lower but more constant gas net generation rate of the first 500 years. The single container study in D2.15 has a higher gas generation rate with a sharp drop after 50 years when available water has been consumed.

The in this study presented gallery scale simulation is one of the first having a detailed resolution of the drum characteristics. This allows more precisely simulations for better performance assessments of the repository. Here The impact of changes of different material parameters is of interest to find parameters leading to a minimization of the gas pressure peak and to predict re-saturation times of the repository. In this study the simulation time does not cover the increase of hydrogen generation of the metal containers due to pH decrease by the ASR reaction. This will happen under saturated conditions after around 1000 years and could potentially lead to a new gas pressure maximum. This study shows that it is unlikely that CO_2 migrates towards the metal containers if there are no fractures in the mortar. Therefore, it is unlikely that cement carbonation leads to a significant drop in pH in the metal containers and increase in corrosion rates. However, this has to be studied/confirmed in additional simulations including a 1000+ years simulation time. The model setup here could be further improved by increasing the model size and the mesh resolution especially at the drums and at the transition areas of materials with large properties changes. Additionally, the function for calculating the steel corrosion rate could be replaced by a continuous function in dependence of pH.

5. Reference ILW disposal cell in granite

5.1 Short description of the ILW disposal cell in granite

The generic configuration of the ILW disposal cell concept in granitic host rock is presented in Figure 5-1. The domain under consideration includes:

1) Waste zone with two types of waste packages
    - Metallic waste;
    - Organic waste.
2) Cementitious backfill.
3) Granitic host rock.

The tunnel width is 11 m and the height is 13 m. In addition, several meters of the host rock should be considered in the model.

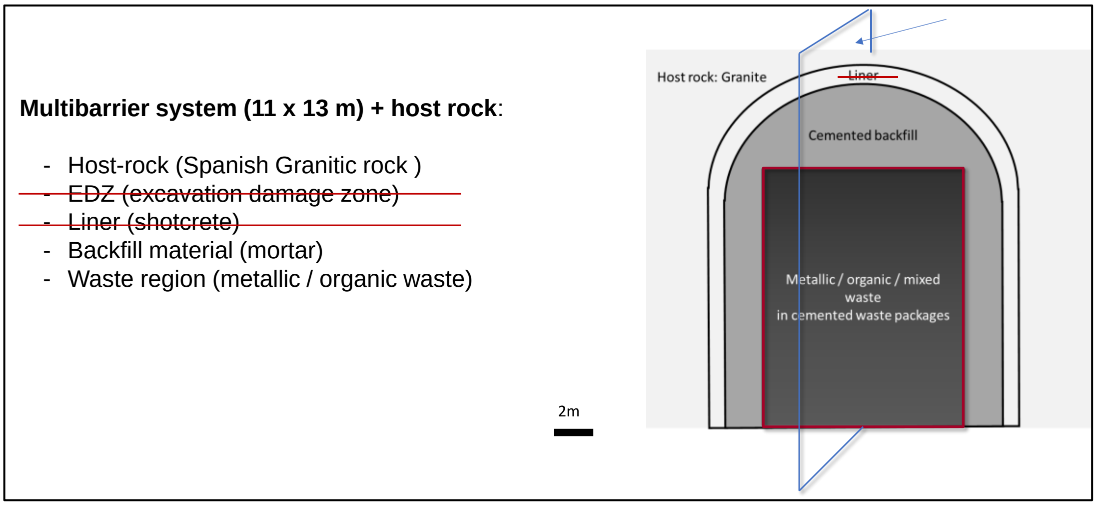

Multibarrier system (11 x 13 m) + host rock:

- Host-rock (Spanish Granitic rock)
- ~~EDZ (excavation damage zone)~~
- ~~Liner (shotcrete)~~
- Backfill material (mortar)
- Waste region (metallic / organic waste)

Figure 5-1. Layout of the representative ILW disposal cell concept in a granitic host rock. Note: The EDZ and the liner considered in the ILW clay disposal cell are not part of the disposal ILW cell in crystalline rock.

A more detailed representation of the waste zone is provided in Figure 5-3. It is assumed that the waste zone contains three rows of containers: two rows with organic waste packages and a row of metallic waste packages in between.

As regards granitic host rock, Spanish granite was proposed and its characteristics were provided in Chapter 2 (Samper et al., 2008).

According to the disposal cell in granitic rock layout (Figure 5-1), the dimensions of the multibarrier system are 11 x 13 m plus host rock. In order to keep up with similar model dimensions between the different host rock concepts for ILW (i.e. clay and crystalline rock), the disposal cell in the clay rock, presented during ACED meeting (January 2021, see Figure 5-2), is taken as an example without considering the EDZ and the liner.

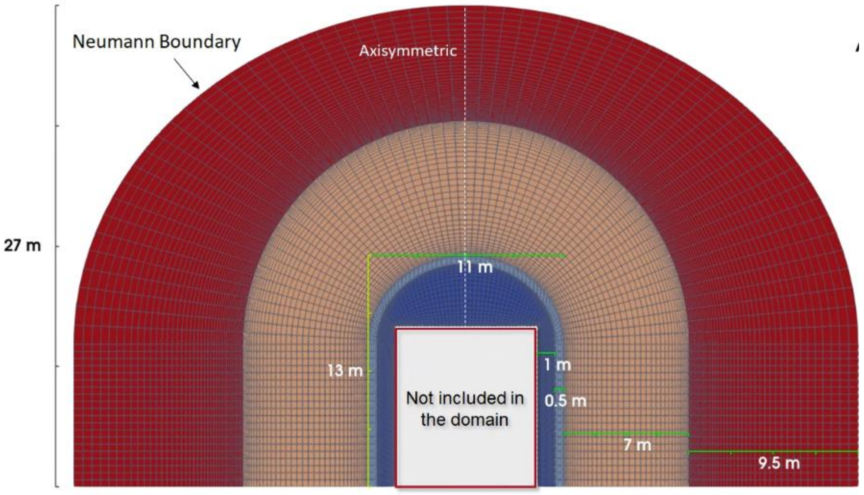

Figure 5-2. Layout of the representative ILW disposal cell concept in a clay host rock. In dark blue: backfill material, light blue: liner, brown: EDZ, red: host rock

According to the layout of the ILW disposal cell concept in a clay host rock (see Chapter 4 for more details), the waste zone is surrounded by backfill of 1 m thickness from both sides and somewhat higher thickness on the top. In addition, about 10 m of the host rock around the tunnel is considered. Based on this information, it is assumed that the thickness of the backfill at both sides of the waste zone is 1 m and the thickness of the backfill on the top is 2 m. Taking into account that emplacement dimensions are 11 x 13 m (L x H), the dimensions of the waste zone are assumed to be 9 x 11 m (L x H). 10 m of the granitic host rock around the backfill is also included.

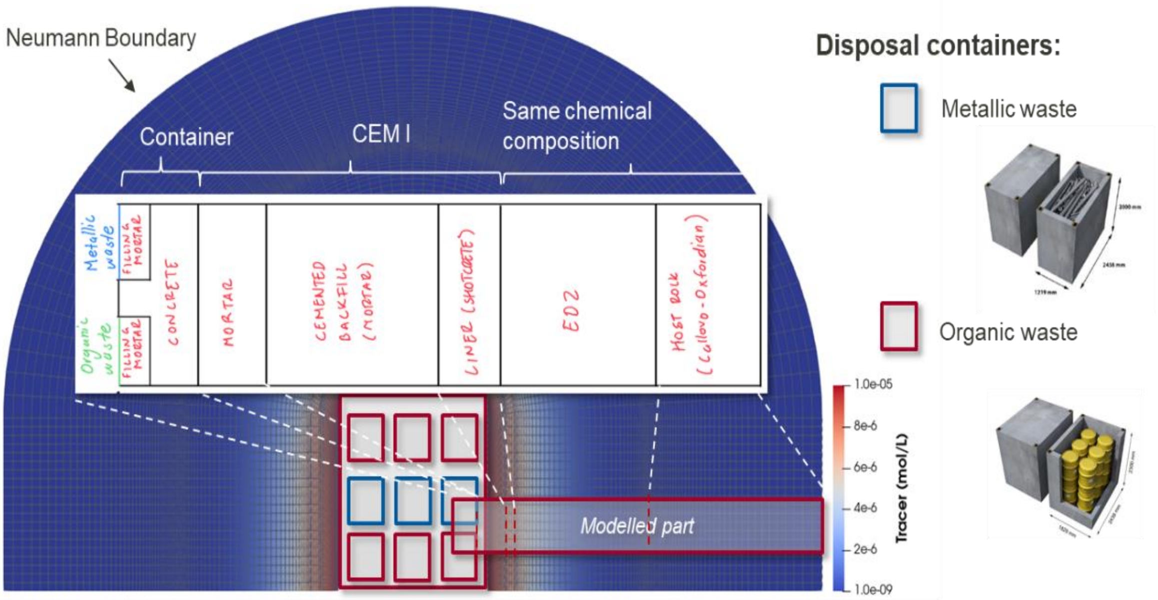

Figure 5-3. Waste zone *(as presented in ACED meeting, January 2021)*.

5.2 Relevant output variables

The relevant outcomes of the reactive transport model of the ILW disposal cell in granite are focused on the time evolution at selected locations and interfaces and the spatial distribution at selected times of:

1) The computed pH and redox.
2) The computed concentrations of the dissolved chemical species, including Na, K, Ca, Mg, Cl, HCO_3^-, SO_4^{-2}, Si, Fe and Al.
3) The computed concentrations of the included mineral phases (portlandite, CSH, calcite, ettringite, …)
4) The computed volume fractions of the mineral phases.

5.3 Lower fidelity models

5.3.1 Hierarchy of models

5.3.1.1 Simplified cement model

The chemical processes involved are assumed to evolve under thermodynamic equilibrium, including the reactions between each cementitious material and the host rock. A thermodynamic database, CEMDATA v18 (Lothenbach, 2019) (https://www.empa.ch/cemdata) – PHREEQC version is used to represent the cement system, where a comprehensive selection of cement hydrates on ordinary Portland cement and alkali-activated materials is available. Moreover, the equilibrium constants (i.e., log K values) for each equilibrium reaction under various conditions, standard molar volumes for each mineral, etc., are available in this thermodynamic database. For the minerals and solute species not found in CEMDATA, i.e., B, Br, F, Mn, and P present in one of the sensitivity cases, additional thermodynamic data, including the element species, chemical formula, molar weight, equilibrium constants and related mineral phases, from the Phreeqc 3.7.0 database (Parkhurst and Appelo, 2013) was added to the system. The calcium silica hydrate is considered ideal solid solutions with six end members (CSHQ-JenD, CSHQ-JenH, CSHQ-TobD, CSHQ-TobH, KSiOH, and NaSiOH), following the CSHQ model proposed in (Kulik, 2011). All cementitious materials are considered fully equilibrated as initial conditions in the reactive transport simulations. The cement hydration calculations have been carried out using the Gibbs energy minimization approach (with the GEM-Selektor software (Kulik et al., 2013)), and the composition of initial mineralogical phases and equilibrated pore water were reported in D2.16. It is worth noting that aggregates are considered chemically inert in the reactive transport model in this work.

The chemical reactions lead to porosity changes in cementitious materials due to the dissolution/ precipitation of phases, which changes the permeability property of the cementitious barrier. Therefore, the porosity and permeability feedback are considered important factors when simulating the chemical evolution at the disposal cell scale. In the case of considering the feedback, the porosity is updated in each time step of the chemical calculations by adding the precipitated phases and removing the dissolved ones in volume fraction. The resulting change of porosity is then transferred to the transport equations as feedback and the corresponding diffusive properties are updated.

5.3.1.2 Simplified internal geometry

The reactive transport model of the ILW disposal cell surrounded by granitic host rock considers the system in an initially fully saturated state, and each section has been conceptualized as homogeneous porous media. The schematic layout is presented in Figure 5-4, which includes:

1) Waste zone (with a length of 7.4 m).
2) Container wall (with a length of 0.2 m).
3) Waste package backfill (with a length of 0.3 m).
4) Vault backfill (with a length of 0.8 m).
5) Granitic host rock (with a length of 10 m).

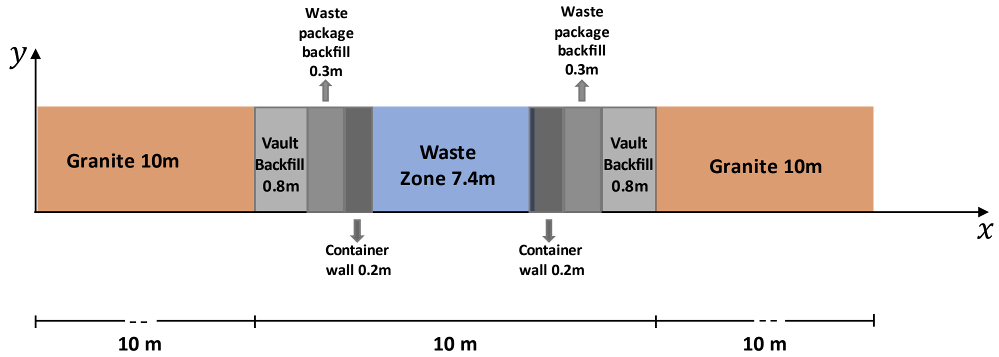

Figure 5-4. Layout of the representative ILW disposal cell in a granitic host rock.

As explained above, the waste zone is treated as a homogeneous material, and the gas generated from the waste packages is out of the scope in the abstracted model. Two cases of the waste zone are investigated in this work: (i) the waste zone is treated as the same material as the backfill mortar; and (ii) the waste zone is considered as an empty space, which is initially filled with backfill pore water. The first case will be studied as the reference case, and the second case will be investigated in sensitivity analyses (see subsection 5.3.3).

The container wall is a low-porosity material that has a low diffusion coefficient, preventing the groundwater from flowing into the waste package. Waste package backfill and vault backfill are considered the same mortar material. All cementitious materials use CEM I 42.5 N cement with a composition reported previously in D2.16 (Samper et al., 2021). The Spanish granite is used as the host rock for the ILW disposal cell, which has properties of low fracture density, tectonic stability, and low seismicity (Samper et al., 2021). Two cases of granite are considered in abstracted models: active in chemical reactions (see section 5.3.1.4) and inert material (see section 5.3.1.5). The interested reader is referred to D2.16 (Samper et al., 2021) for detailed information on the granitic host rock.

5.3.1.3 Input for simulations

Cementitious materials are considered fully equilibrated as initial conditions in the reactive transport simulations. The summary of input parameters are presented in *Table 5-1* and *Table 5-2*, i.e., the initial mineral phases, the composition of pore water in cementitious materials and groundwater. The fully hydrated mortar/concrete includes portlandite, CSHQ, and calcite as the main minerals, and the C-S-H solid solution shows a relatively higher amount of the JenD (Ca/Si=2.25) and TobD (Ca/Si=1.25) end members. The equilibrated pore water in backfill mortar and container wall shows a highly alkaline pH due to the high concentrations of Na and K. The calculated porosity of the backfill mortar is 29% based on the cement hydration calculations, while that of container wall is 8.5%. A pore diffusion coefficient of 1.0E-9 m^2/s is selected, which considers the high interconnection of the pore structure in the mortar and a corresponding high impact on transport property.

Table 5-3 lists the simulation cases that were performed in this study.

Table 5-1. Initial mineral phases in cementitious materials (T4.7, D2.16 (Samper et al., 2021)).

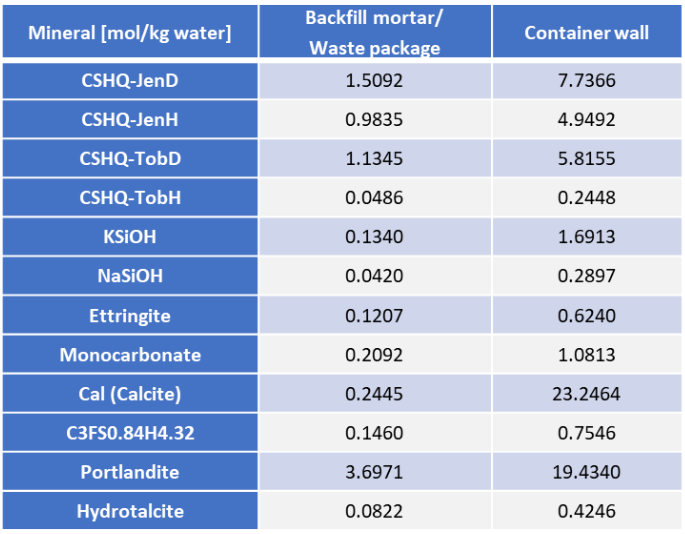

Mineral [mol/kg water]	Backfill mortar/ Waste package	Container wall
CSHQ-JenD	1.5092	7.7366
CSHQ-JenH	0.9835	4.9492
CSHQ-TobD	1.1345	5.8155
CSHQ-TobH	0.0486	0.2448
KSiOH	0.1340	1.6913
NaSiOH	0.0420	0.2897
Ettringite	0.1207	0.6240
Monocarbonate	0.2092	1.0813
Cal (Calcite)	0.2445	23.2464
C3FS0.84H4.32	0.1460	0.7546
Portlandite	3.6971	19.4340
Hydrotalcite	0.0822	0.4246

Table 5-2. Composition of groundwater and pore solution in cementitious materials (T2.5 and T4.6, D2.16 (Samper et al., 2021)).

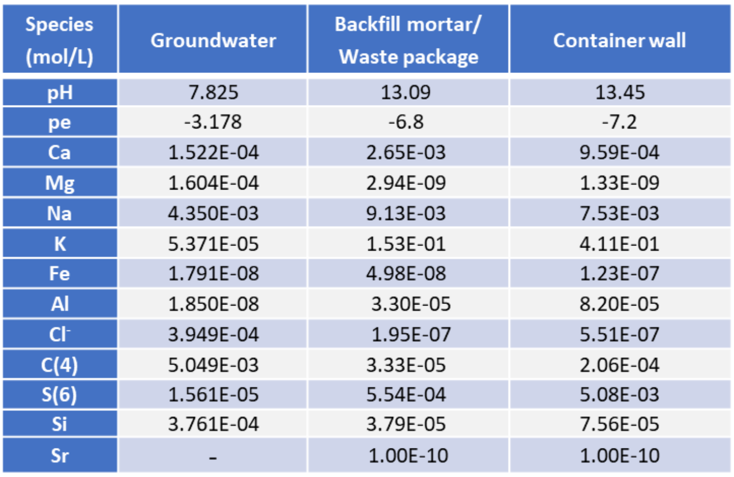

Species (mol/L)	Groundwater	Backfill mortar/ Waste package	Container wall
pH	7.825	13.09	13.45
pe	-3.178	-6.8	-7.2
Ca	1.522E-04	2.65E-03	9.59E-04
Mg	1.604E-04	2.94E-09	1.33E-09
Na	4.350E-03	9.13E-03	7.53E-03
K	5.371E-05	1.53E-01	4.11E-01
Fe	1.791E-08	4.98E-08	1.23E-07
Al	1.850E-08	3.30E-05	8.20E-05
Cl^-	3.949E-04	1.95E-07	5.51E-07
C(4)	5.049E-03	3.33E-05	2.06E-04
S(6)	1.561E-05	5.54E-04	5.08E-03
Si	3.761E-04	3.79E-05	7.56E-05
Sr	-	1.00E-10	1.00E-10

Table 5-3. Summary of simulation cases.

Case	Flow rate (m/s)	Granite hydraulic conductivity (m/s)	Hydraulic gradient	Waste zone	Vault backfill/waste package backfill	Container wall/vault wall	Boundary condition	Granite host rock considered
1-1D: Section 5.3.1.4	2.33e-13	8.72e-12	0.026773	Same material as Vault backfill.	Referred to *Table 5-1* and *Table 5-2*.		Constant concentration with a hydraulic gradient.	Yes
2-2D: Section 5.3.1.6								Yes
3-2D: Section 5.3.3.3	-		-				Constant concentration	Yes
4-1D: Section 5.3.1.5	2.33e-13		0.026773				Constant concentration with a hydraulic gradient.	No
5-1D: Section 5.3.3.1				Empty space and saturated with pore solution of backfill mortar.				No
6-1D: Section 5.3.3.2	-	3.70E-09	0.005	Same as case 1.	Vault backfill is considered as non-reactive granitic crushed rock, with only diffusional transport; Reinforced concrete is considered as material in vault walls; Detailed information is in *Table 5-6* to *Table 5-8*.			No

5.3.1.4 1D abstracted model considering disposal tunnel and surrounding granite

The considered ILW cell in granite is composed of the waste zone, vault backfill mortar and several meters of host rock. The waste zone itself is a complex system consisting of two types of concrete containers with cemented organic or metallic waste; containers are backfilled with cementitious material (see Section 5.1). In the abstracted model, described in this section, containers are not represented explicitly. Instead, the volume of the waste zone is considered as a rectangle filled with homogeneous cementitious material with the properties of the vault backfill mortar surrounded by the functional concrete (representing container wall) and a layer of waste package backfill. The abstracted model is one-dimensional and considers advective and diffusive transport. Groundwater flow is assumed to be 2.33E-13 m/s (based on data for Spanish granite, see deliverable D2.16 (Samper et al., 2021)) and the flow direction is arbitrarily selected to be from left to right. The modelled system is presented in Figure 5-5. The chemical composition of the vault backfill mortar and functional concrete as well as pore water composition are taken from ACED deliverable D2.16 (Samper et al., 2021) as presented in Section 5.3.1.3. The chemical composition of the granite boundary water is listed in Section 5.3.1.3 and is based on (Samper et al., 2016). The initial calcite volume fraction is 5%. Mineral dissolution and precipitation in the entire system is enabled. Modelling is performed with the computer code PHAST (Parkhurst et al., 2010).

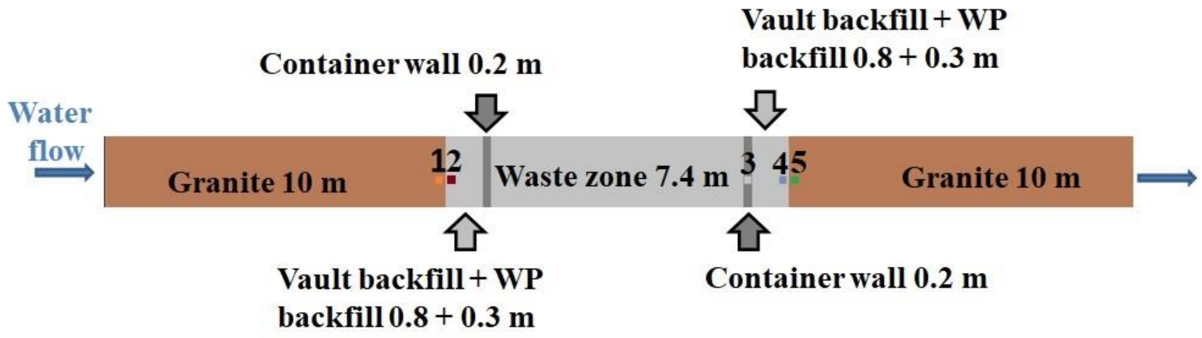

Figure 5-5. 1D representation of the system considered in the abstracted model with the homogenized waste zone (numbers 1-5 indicate observation points).

One of the main parameters indicating the chemical evolution in a disposal cell is pH. Figure 5-6 presents pH profile in the modelled domain at certain time after the repository closure (Figure 5-6a) and pH evolution at certain disposal cell locations (Figure 5-6b).

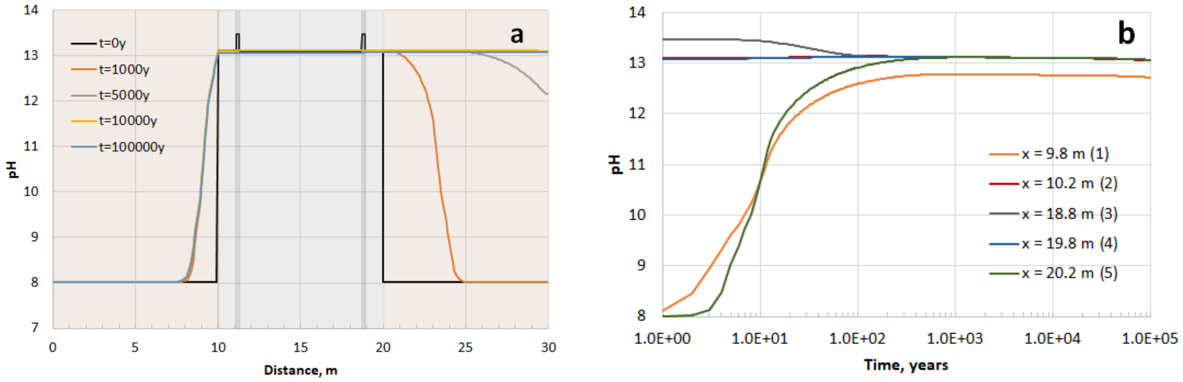

Figure 5-6. pH evolution in ILW cell in granite obtained with the abstracted model: a – pH profile, b – pH evolution at certain locations of the system (position of the locations (observation points) is indicated in Figure 5-5).

It can be seen from Figure 5-6 (a) that on the left-hand side of the granite and vault backfill boundary, the pH increases for a few meters to the left from this boundary. This increase is related to leaching of cementitious material and transfer of chemical species by diffusion into granitic host rock. However, the competing process of advection prevents the high pH front from going deeper into granite. This is also confirmed in Figure 5-6 (b), where pH change in time 20 cm from the boundary is presented (observation point (1)). At this location pH increases up to value of 12.8 in about 800 years and stays almost constant for the rest of the modelled period of time.

On the right-hand side of the granite and vault backfill boundary, pH front propagates deeper into granite and reaches about 5 m from the boundary in 1,000 years. After 5,000 years pH increases up to 13.1 in the whole modelled granite region to the right from the boundary. Looking at Figure 5-6 (b), it can be seen that in about 500 years pH in the vault backfill mortar, container walls, waste zone and granite in near vicinity of the boundary becomes equal and is slightly above value of 13.

The spatial distribution of the concentrations of Na, K, Ca and Cl in the pore water obtained with the abstracted model at certain time after the repository closure is presented in Figure 5-7.

It can be seen from Figure 5-7 that differences in the pore water composition of the vault backfill mortar and container wall decrease with time. Na, K, Ca and Cl concentrations in the pore water in the whole cement region is almost the same after 10,000 years. The left-hand side granite pore water composition is affected by the cement region up to few meters from the granite-vault backfill mortar boundary only (similar to the pH increase). However, species, leached from cement, change pore water composition in the granite significantly to the right from the vault backfill mortar-granite boundary, e.g., K concentration after 10,000 years in the modelled 10 m of granite reaches the same value as in the cement region.

Cl concentration initially is higher in the granite pore water than in the pores of cementitious materials. It can be seen from Figure 5-7 (d) that Cl concentration in course of time is constantly increasing in the cement region. On the other hand, change of Cl concentration in the cement region affects pore water composition in the granite. It can be seen that after 100,000 years Cl concentration in the cementitious barriers and the modelled granitic host rock pore water to the right from the tunnel (in the direction of the groundwater flow) is very similar.

Figure 5-7 suggests that pH evolution in the disposal cell (see Figure 5-6) correlates strongly with potassium leaching. This can be confirmed analysing Figure 5-8 where K concentration changes in time at the observation points are presented. Comparing Figure 5-6 b and Figure 5-8 it can be noticed that changes in K concentration and pH in time are of the same pattern.

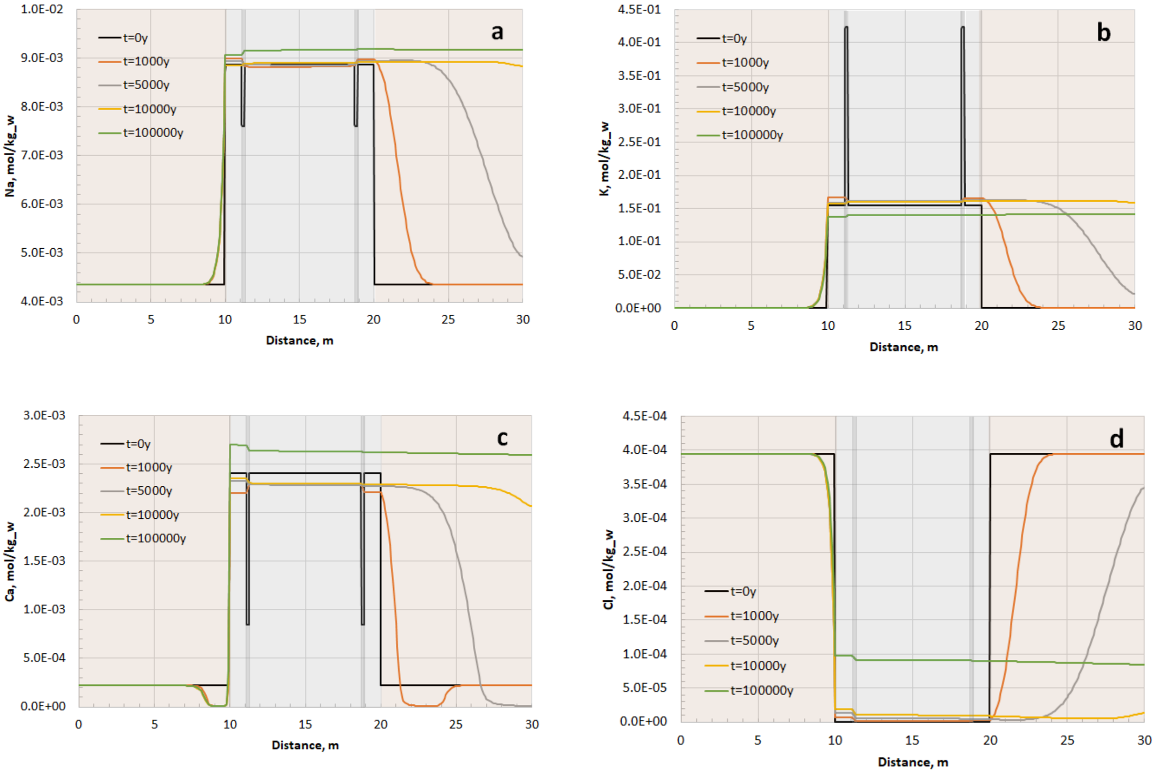

Figure 5-7. Spatial distribution of dissolved species: a – Na, b – K, c – Ca, d – Cl.

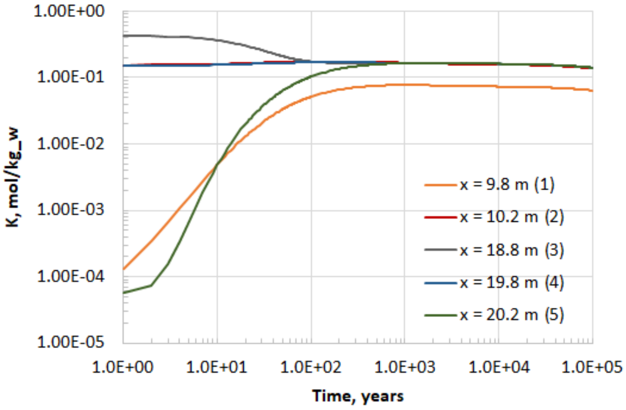

Figure 5-8. K concentration at certain locations of the modelled system (position of the locations is indicated in Figure 5-5).

Dissolution and/or formation of minerals in the analysed disposal cell proceeds very slowly. During the modelled period of time, very low dissolution of portlandite and CSH phases as well as formation of calcite were observed. Initial concentration profiles of the mentioned minerals and mineral concentrations at the end of the modelled period of time are presented in Figure 5-9.

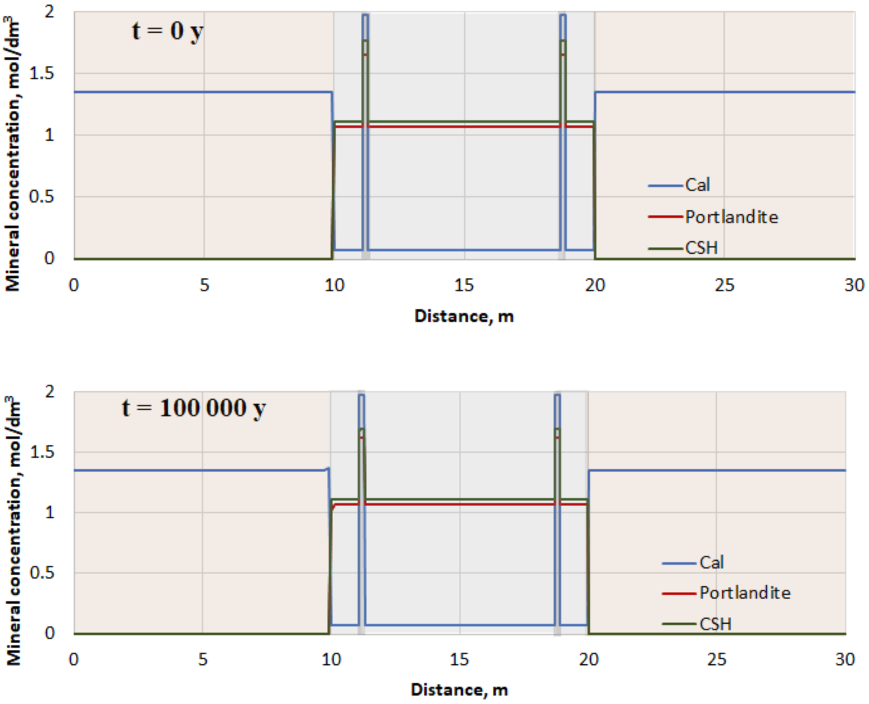

Figure 5-9. Mineral concentration profiles: initial (top) and after 100 000 years (bottom).

Comparison of initial mineral concentrations and mineral concentrations after 100,000 years revealed that the most significant change was in portlandite concentration close to the left-hand side of the granite and vault backfill boundary where concentration of portlandite decreased by about 5% due to its dissolution. Similar change, but with opposite effect, was also in calcite concentration: close to the left-hand granite and vault backfill boundary precipitation of calcite resulted in increased calcite concentration by about 5%. The most significant change in CSH phases concentration was observed in functional concrete (corresponding to container wall), due to leaching of KSiOH and NaSiOH components. However, the total change of CSH phases concentration was less than 4.5%. It should be mentioned that very small amounts of hydrotalcite precipitated in the granitic host rock, as precipitation of minerals in the granite was enabled. However, the concentration of hydrotalcite was of the order of 1E-7 mol/dm^3 and it cannot be excluded that such result is due to numerical issues.

5.3.1.5 1D abstracted model without considering granite

In this subsection, we present a 1D abstracted model where granitic host rock is not considered in the simulation. A case considering the full temporal scale (100,000 years) is simulated. The reactive-transport modelling tool HP1, which couples Hydrus-1D with PHREEQC geochemical code, is used. The simulated evolution and profile of the mineralogical phases and pore water composition in the multibarrier system are presented.

The investigated cementitious barrier system has a length of 10 m, and it is divided into 100 elements with $\Delta x = 0.1$ m. The porosity-permeability feedback is considered in the simulations. The interaction with granite is simplified to a constant advection-diffusion of groundwater on the boundaries, and a constant concentration was applied as the boundary condition. A hydraulic gradient of 0.026773 is applied here in the reference case with a pressure head of 0.26773 m on the left and 0 on the right within a distance of 10 m. The calculations are based on assumptions of a slow groundwater flow rate of 2.33E-13 m/s and a hydraulic conductivity of 8.72E-12 m/s in the granite (T5.5 in D2.16, Samper et al., 2021).

Figure 5-10 shows the initial state of the mineralogical phases in the ILW repository disposal cell, where the aggregate in mortar is represented by the inert phase and the empty space represents the porosity. The pH value is shown on the secondary axis on the right, which has a highly alkaline pH above 13 at initial states. The container wall is denser with a relatively higher content of aggregates, portlandite, C-S-H, calcite, ettringite, and other minerals, compared to the backfill mortar.

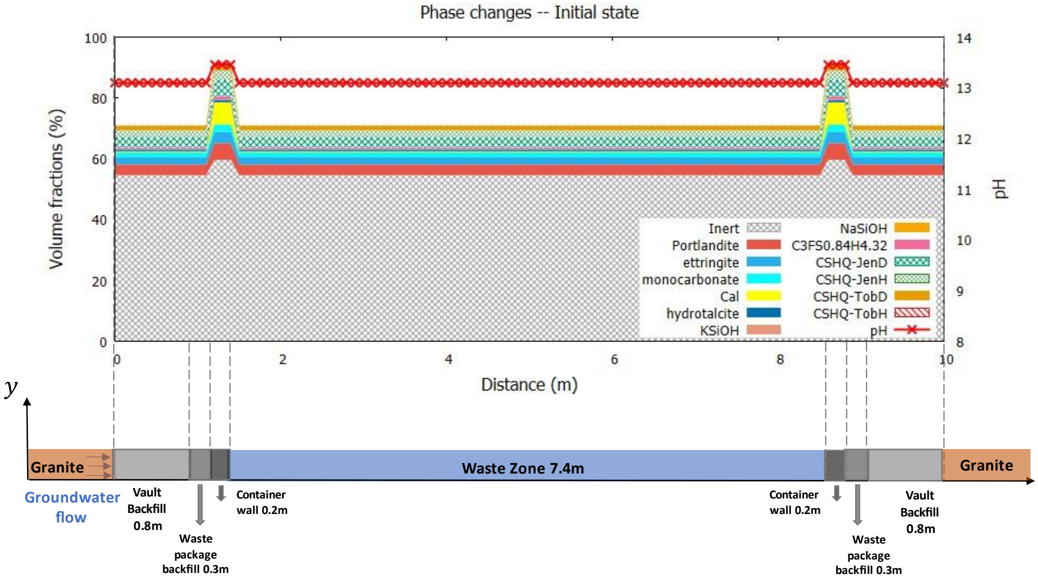

Figure 5-10. Initial mineralogical phases present in the representative ILW disposal cell.

Due to the ingress of groundwater and the concentration gradient of elements in pore solutions at the interface among host rock, mortar, and concrete, chemical reactions are initiated leading to chemical gradients, as shown in Figure 5-11 The figures show the evolution of mineralogical phases and the pH in the ILW disposal cell after being exposed for up to 100,000 years. The main degradation phenomenon occurring in cementitious material is the transformation of portlandite into calcite, followed by the decalcification of C-S-H and the formation of calcite. These reactions lead to porosity increase due to their molar volume differences. After being exposed for 5 000 years (see Figure 5-11(b)), all portlandite included in vault backfill and waste package backfill are dissolved and the degradation almost reaches the container wall. Meanwhile, a large amount of calcite is observed accumulated near the border of the considered system reducing the porosity. The mortar degradation extends to the waste zone over time. The porosity of the container wall increased from 8.5% to approximately 13.8%, while the porosity at the border region decreased to almost 0 due to the accumulated formation of calcite after being exposed for 100,000 years.

The pH values of the cementitious material drop from an initial value of above 13 along the degradation. The decrease of pH values is observed firstly in vault backfill and subsequently in waste package backfill and container wall due to the interaction with groundwater, e.g., leaching of species from cementitious material to host rock and ingress of groundwater. The pH values in the region close to the border of the considered system continue to decrease, approaching 8 due to a low pH value in groundwater of around 7.825. However, the pH values in most parts of cementitious material rise again. This can be explained by the relatively higher kinetics of leaching out of species from cementitious material to the granitic host rock, compared to the ingress rate of groundwater. It means that the diffusion process is playing the dominant role, instead of the advection process. This can be further confirmed by the symmetrical mineral profiles in the disposal cell. The advection process simulated by the low gradient of the pressure head has no obvious effect on the chemical reactions. However, this can be explained by the fact that a very low flow rate of groundwater (2.33E-13 m/s) is applied in the simulations.

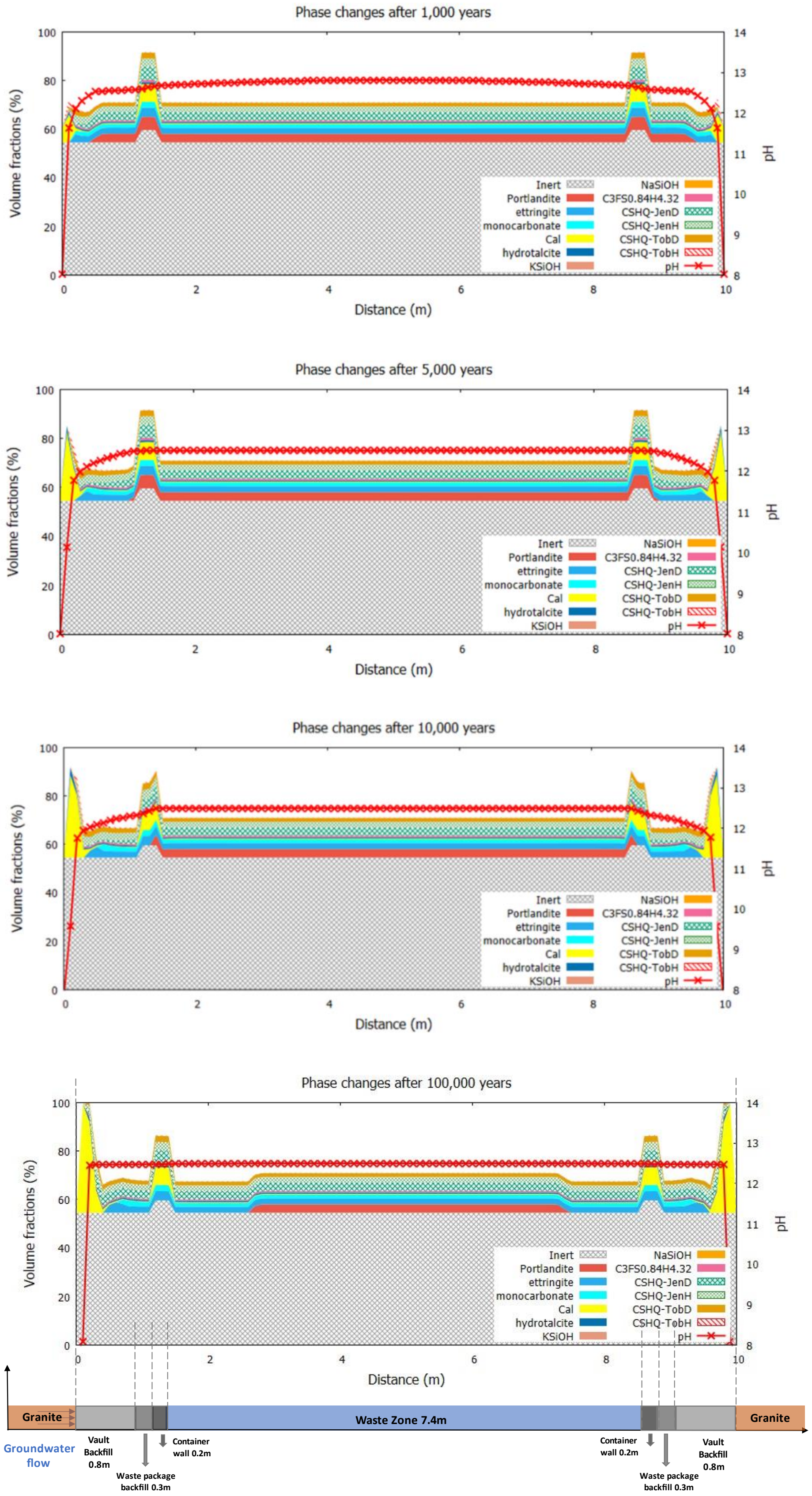

Figure 5-11. Profiles of the mineralogical phases present in the ILW disposal cell after being exposed for up to 100,000 years.

Figure 5-12 summarizes the evolution of the concentration of Na, K, Ca, and Cl in cementitious barriers after being exposed for up to 100,000 years. The changes in concentration are much faster compared to the simulation case presented in section 5.3.1.4, and the reason is due to the constant concentration we applied as the boundary condition in this case. Sodium tends to leach out from cementitious material to granitic host rock over time. The concentration of K increases obviously during the first 1,000 years, and goes down afterwards. The concentration of Ca in vault backfill and waste package backfill increases in the first 1,000 years, followed by a decrease in the following 10,000 years and a rise again until 100,000 years, which results from the dissolution of Ca-containing phases and the leaching of Ca to granitic host rock. However, the concentration of Ca in the waste zone increases continuously due to a gradual dissolution of CH and C-S-H. This observation is consistent with the evolution of pH values discussed above. The concentration of Cl increases over time due to the interaction with ground water where the concentration is relatively higher.

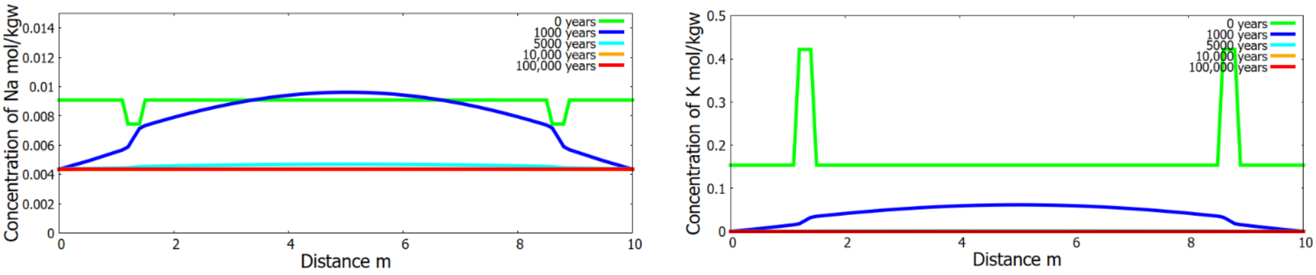

(a) Profile of the concentration of Na [mol/kgw];

(b) Profile of the concentration of K [mol/kgw];

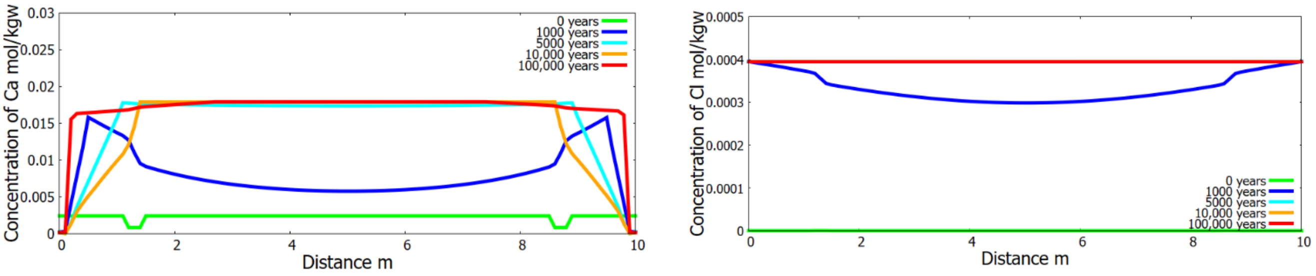

(c) Profile of the concentration of Ca [mol/kgw];

(d) Profile of the concentration of Cl [mol/kgw];

Figure 5-12. Profiles of the (a) Na; (b) K; (c) Ca, and (d) Cl concentration [mol/kgw] in pore solution of cementitious material after being exposed for up to 100,000 years.

5.3.1.6 2D abstracted model

The abstracted model with homogenized waste zone as described in Section 5.3.1.4 was also implemented in a 2D geometry. It should be noted that due to large demand of computational resources required for 2D models, a coarser spatial and time-step grid was used. Spatial grid was set to 10 cm for the larger part of the domain. The exception was only the middle part of the granite to the left and bottom from the waste zone, where the grid size was 20 cm. Time-step size was used as presented in Table 5-4 for the "very coarse time-step grid". The changes in pH in the modelled region at certain time steps are presented in Figure 5-13.

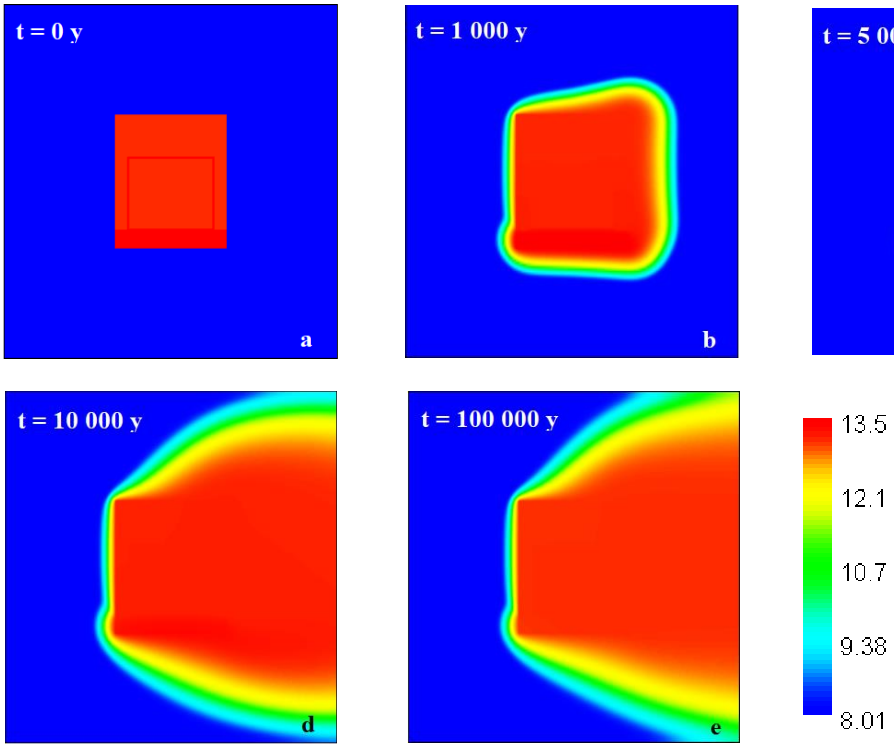

Figure 5-13. pH plots at different time steps: a – 0 years, b – 1,000 years, c – 5,000 years, d – 10,000 years and e – 100,000 years (spatial dimensions: horizontal – 30 meters, vertical – 32 meters).

It can be seen from Figure 5-13 that propagation of the high pH front is to the right from the tunnel and follows the groundwater flow direction. In addition, due to diffusion, an increase of pH to the left-hand side granite close to the vault backfill is also observed. These results are consistent with the pH changes obtained with the 1D model and presented in Section 5.3.1.4. However, 2D model indicates that propagation of the high pH front is non-symmetric: it is slightly higher in the top right corner and lower at the bottom. This is because of the functional concrete at the bottom of the tunnel which is of lower hydraulic conductivity and has lower effective diffusion coefficient.

One of indicators of changes in pore water composition is Cl, which is considered as a tracer. Cl concentrations in the pore water at different time steps are presented in Figure 5-14.

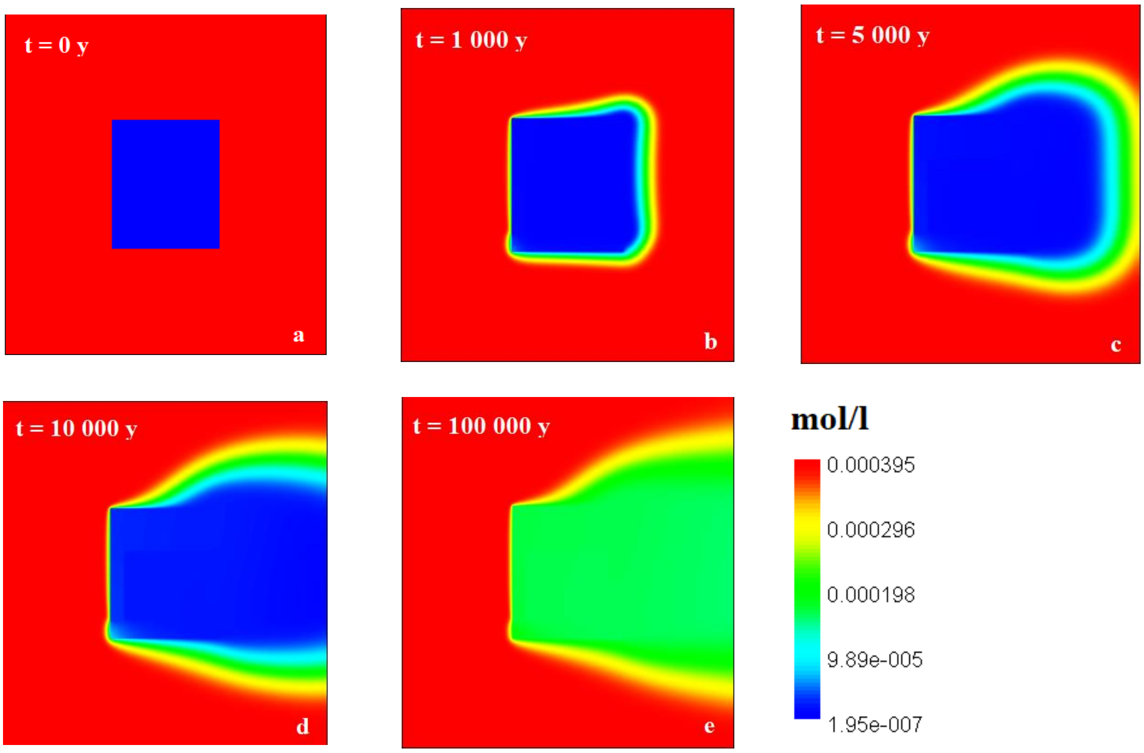

Figure 5-14. Cl concentration in the pore water at different time steps: a – 0 years, b – 1,000 years, c – 5,000 years, d – 10,000 years and e – 100,000 years (spatial dimensions: horizontal – 30 meters, vertical – 32 meters). Note that the colour scale is not linear.

It can be seen from Figure 5-14 that groundwater flowing through the tunnel filled with cementitious material changes pore water composition in the granite to the right from the tunnel, where decrease of Cl concentration is observed. On the other hand, granitic water with higher Cl concentration as in the cement region enters the tunnel from the left side and as consequence Cl concentration in the vault backfill, container walls and waste zone increases. It can be seen that after 100,000 years Cl concentration in the pores of cementitious materials and in original granite water differs by about factor of 2.

It is also interesting to observe the changes in K concentrations, which are presented in Figure 5-15. It can be seen that K concentration in the functional concrete pores at the bottom of the tunnel decreases significantly slower than in the other parts of the tunnel. Again, this can be explained by the lower functional concrete hydraulic conductivity and effective diffusion coefficient. The plots also indicate that in 100,000 years K could be leached from the cementitious material because its concentration in the tunnel has already been decreasing.

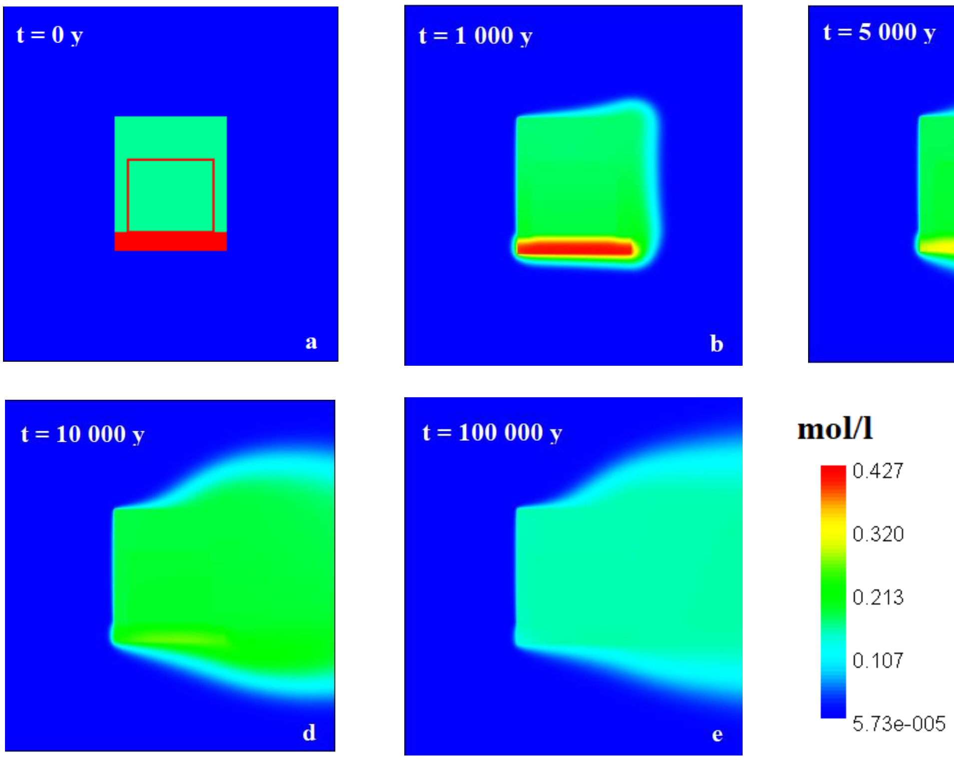

Figure 5-15. K concentration in the pore water at different time steps: a – 0 years, b – 1,000 years, c – 5,000 years, d – 10,000 years and e – 100,000 years (spatial dimensions: horizontal – 30 meters, vertical – 32 meters). Note that the colour scale is not linear.

Changes in the mineralogical composition in the whole modelled domain for the considered time frame were insignificant, therefore no plots are provided.

The chemical evolution in the ILW disposal cell in granite obtained with the abstracted 2D model was also compared with the results from the abstracted 1D model described in Section 5.3.1.4. It should be noted that such comparison is not straightforward. The water flow path lines in the 2D system with several different materials are of complex manner and it is difficult to choose the horizontal line which could appropriate represent the 1D model. For comparison of the results for 1D and 2D geometries, the results on the horizontal line laying in the middle of the waste zone in 2D model are compared with the results from 1D model. One more point is that 2D model has a coarser time-step and space grid than 1D model described in Section 5.3.1.4. In order to make 1D and 2D models more consistent, additional 1D simulation was performed with modified grid corresponding to 2D case. (The effect of the coarser spatial grid and time-step size was investigated and described in Section 5.3.2 and only minor impact on the results was observed.)

Comparison of the pH profiles between 1D and 2D models for the time steps 1,000 years and 100,000 years is presented in Figure 5-16 (a). It can be seen that the difference in pH values between the cases is very small (less than 12 %). Higher differences between the 1D and 2D models were identified for components concentrations in the pore water. As an example, Cl concentration profile is presented in Figure 5-16 (b). In the case of Cl, the difference between the models for the time step 100,000 years makes about 44 % (possibly due to more appropriate representation of diffusion in the 2D model), though the general behaviour of the numerical results is of the same pattern in both runs. For other components and time steps the highest difference between the results varies from few percents to about one order of magnitude.

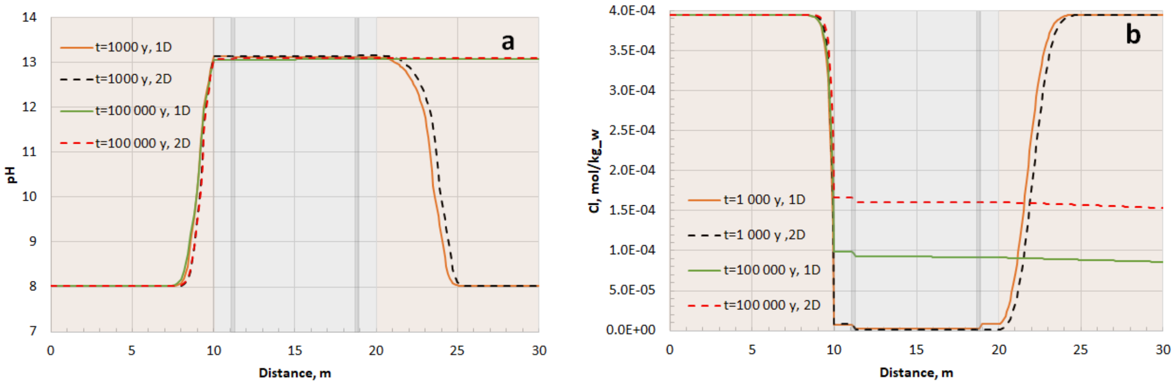

Figure 5-16. Comparison of pH profile (a) and Cl concentration profile (b) obtained with 1D and 2D models.

As a comparison of mineralogical composition obtained with 1D and 2D models, concentration profiles of portlandite and calcite were compared. It turned out that the difference between the simulation results was less than 2%.

Analysis of the results obtained with 2D model and comparison with 1D case results presented in section 5.3.1.4 revealed that the 2D model can much better represent the modelled system. However, depending on the modelling purpose (e.g. to find out the general trend of the pH evolution), 1D model could be sufficient.

5.3.2 Reduced numerical accuracy

Abstracted model described in Section 5.3.1.4 has a non-uniform grid: the grid in most of the model domain is 10 cm and is refined to 2 cm near the interfaces of different materials. To investigate the effect of the coarser spatial grid, a simulation run was performed with a uniform grid of 10 cm, i.e., not refined near the interfaces.

The numerical results in both cases are very close. Comparison of pH profiles at time steps 1,000 years, 5,000 years, 10,000 years and 100 000 years indicated that the difference between the pH values is less than 0.5 %. The difference in pore water composition is slightly higher between the models. However, the largest difference, which is observed for Cl concentration, is less than a factor of 3.5 and for low Cl concentration. Differences in pore water concentration of K and Cl obtained with finer and coarser space grids for time steps 1,000 years and 100,000 years can be seen in Figure 5-17. It can be observed that the most noticeable differences are close to the granite-vault backfill boundaries and at earlier time steps. Differences in concentrations decrease with time and after 100,000 years the results obtained with finer and coarser space grids differ less than 2 %. Regarding concentration of minerals, namely calcite and portlandite, the difference between the fine and coarse space grid cases is insignificant, i.e. is less than 1.5 %.

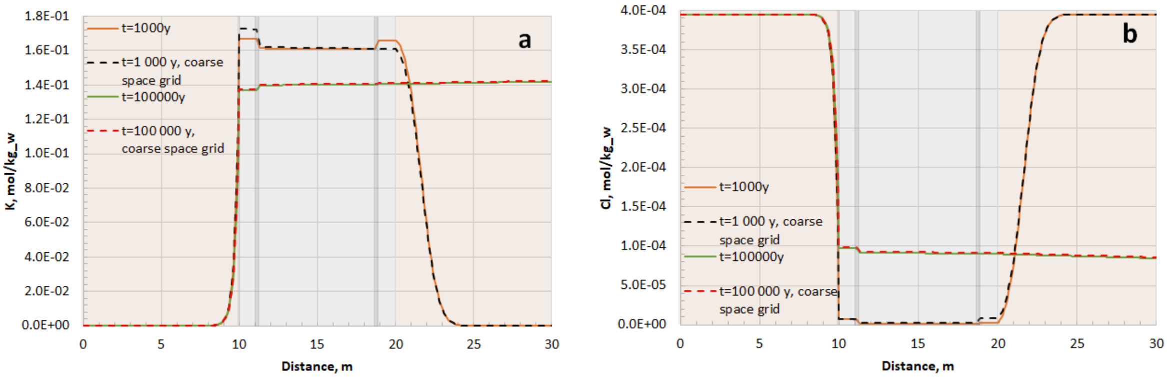

Figure 5-17. Pore water concentration profiles of K (a) and Cl (b) obtained with finer and coarser space grids.

For a simulation run of the abstracted model described in Section 5.3.1.4, the step was 0.01 years for 1,000 years and then increased to 0.1 years. To investigate the effect of a coarser time-step size, the time step after 10,000 years was increased to 1 year. In addition, one more run was performed with a very coarse time-step size grid when the maximal time step of 10 years was selected. The calculation cases of different time step size are summarized in *Table 5-4*.

Table 5-4. Calculation cases and selected time-steps

Time period, years	**Time step size, years**		
	Fine time-step grid	**Coarse time-step grid**	**Very coarse time-step grid**
≤100	0.01	0.01	0.1
100<t≤1,000	0.01	0.01	1
1,000<t≤10,000	0.1	0.1	1
>10,000	0.1	1	10

Analysis of the results obtained with the abstracted model described in Section 5.3.1.4 by varying the time-step size indicates that the selected time step has a minor impact on predicted chemical evolution in the analysed system. The difference between pH values obtained with the fine and coarse time-step grid was less than 0.1 %, while comparing fine and very coarse time-step grid results, the difference did not exceed 0.5 %.

Comparing the concentrations of K, Na, Ca and Cl in the pore water obtained with the finer and coarser time-step grid, the results differ insignificantly. In the case of the coarse time-step grid, the difference was less than 0.2 % and in the case of the very coarse time-step grid – less than 4.5 %. In both cases the largest difference was observed in the Ca concentration.

Regarding concentration of minerals, namely calcite and portlandite, the difference between the fine and coarse time-step grid cases was less than 3 % for coarse time-step grid and less than 5 % for very coarse time-step grid.

It was mentioned in Section 5.3.1.4 that for comparison purposes of 1D and 2D models, additional 1D simulation was performed with modified grid corresponding to 2D case, i.e. the combination of the very coarse time-step grid and coarse spatial grid. The simulation results indicated that in such a case the difference in pH value in comparison with the fine grid simulation is less than 3 %. However, differences in component concentration in the pore water could be significantly larger. The highest difference was observed for Cl concentration in the cement region close to the right-hand vault backfill-granite boundary (see Figure 5-18 where the comparison of Cl concentration profiles simulated with finer and coarser space and time-step grid is presented). On the other hand, such difference was for very low concentrations (of the order of 1E-6 mol/kg_w). When concentration becomes higher, the difference decreases and after 100,000 years is only about 1.5%.

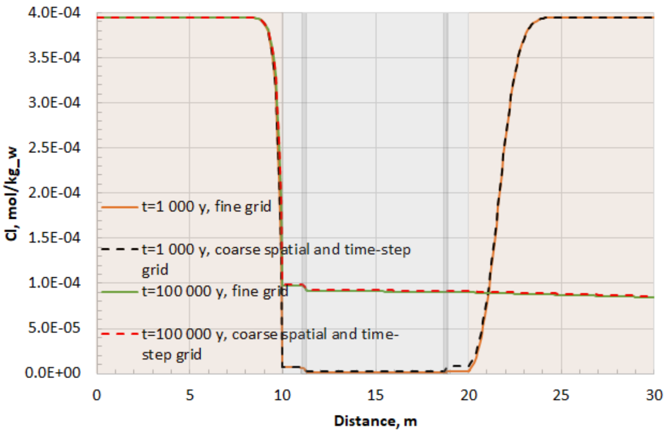

Figure 5-18. Cl concentration profile simulated with finer and coarser space and time-step grid.

Calcite and Portlandite concentration profiles obtained with coarser space and time-step grid were very similar to the profiles obtained with the fine grid – the difference in minerals concentration was less than 1.5%.

Analysis of spatial and time-step grid size effect on modelling results indicated that for the analysed system pH can be sufficiently well modelled with the coarser spatial and time-step grid, therefore saving computational resources. The highest differences between the cases were observed for component concentration in the pore water. In any case, the final selection of the grid size should be consistent with the modelling purpose and tasks.

5.3.3 Sensitivity simulations

In addition to the reference case presented in subsection **5.3.1**, some sensitivity analyses are performed here. The considered sensitivity cases are as follows:

1) 1D abstracted model (granite as inert material) considering the waste zone as a space that is initially filled with backfill pore water, while in the case presented in section 5.3.1.5 the waste zone is considered the same material as the backfill mortar.
2) 1D abstracted model (granite as inert material) simulating the long-term performance of the multibarrier system following the layout of the Olkiluoto repository in Finland.
3) 2D abstracted model (granite as active material) investigating the sensitivity of the predictions to the groundwater flow rate.

5.3.3.1 Sensitivity of the predictions to the property of waste zone

A case considering the waste zone as an empty space filled with the pore water of backfill mortar is simulated by the 1D abstracted model that considers granite as inert material, and the transport properties considered for the waste zone are presented in *Table 5-5*. *Figure 5-19* shows the mineralogical phases of the ILW disposal cell at the initial state and after being exposed for up to 20,000 years. The calculation was stopped soon after 20,000 years since the porosity of the area close to the border was approaching 0 and no space was available for transporting the solution. The degradation kinetics in this case are much faster compared to the case presented in section 5.3.1.5 for the lack of the cementitious material included in the waste zone. As explained in subsection 5.3.1.5, the pH in the cementitious barrier is maintained stable largely due to CH and C-S-H in the waste zone. This indicates the importance of placing cementitious material in the waste packages. Moreover, the mineralogical profile of the system shows some differences on the two border sides: the cementitious material is more degraded on the left, with a lower pH value compared to the right side. This could be explained by the fact that without the cementitious material placed in the waste zone, the groundwater can flow more easily through the system and the advection process is more dominant.

Table 5-5. Transport properties for the waste zone (T5.1, D2.16):

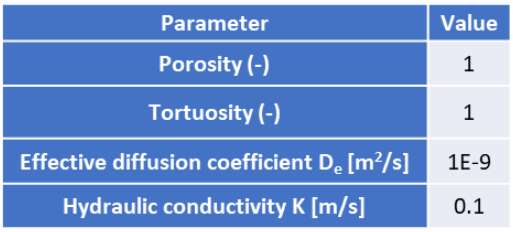

Parameter	Value
Porosity (-)	1
Tortuosity (-)	1
Effective diffusion coefficient D_e [m^2/s]	1E-9
Hydraulic conductivity K [m/s]	0.1

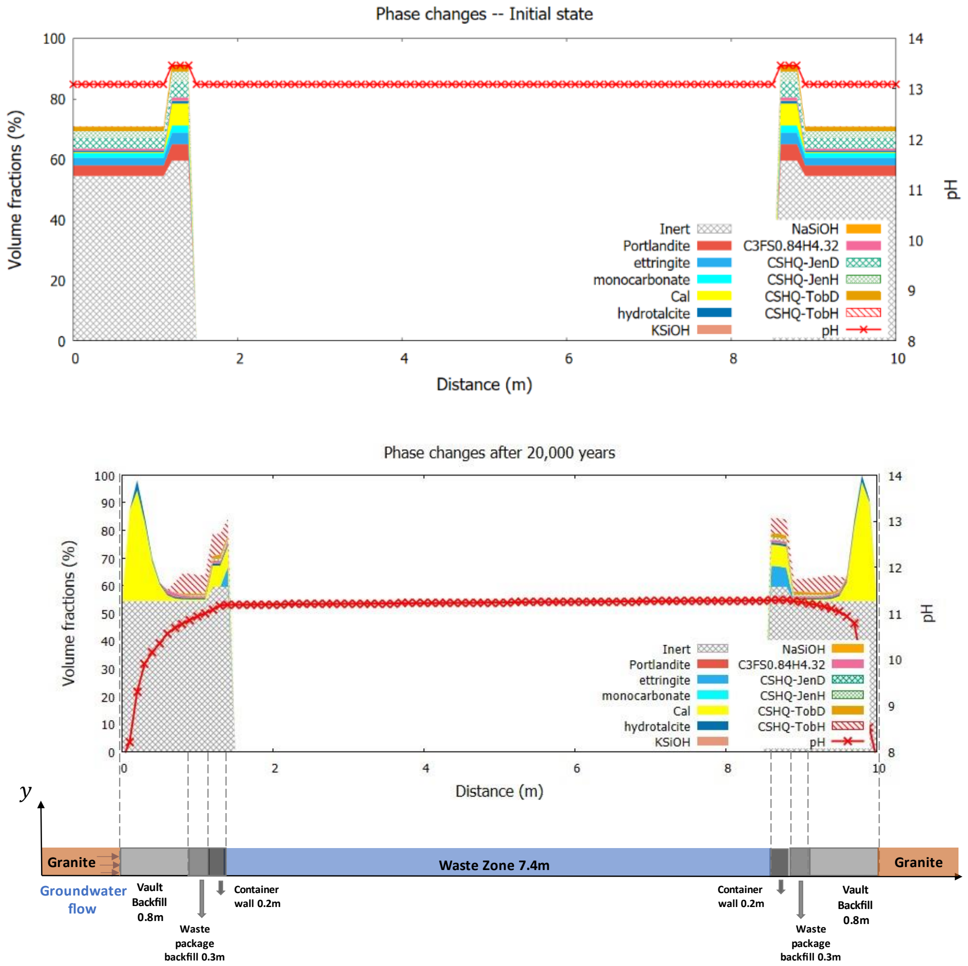

Figure 5-19. Profiles of the mineralogical phases present in the ILW disposal cell at initial state and after being exposed for 20,000 years.

5.3.3.2 Sensitivity analysis case for Finnish repository: Olkiluoto

A case considering the ILW repository in Olkiluoto, Finland is studied, which is composed of the homogenized waste zone, concrete silo walls, and crushed rock backfill. The model with a total length of 23.5 m is based on the repository layout applied in previous calculations (Vieno et al. 1991) and is presented in *Figure 5-20*. Keeping in line with the case reported in subsection 5.3.1.5, the chemical reactions in bedrock are neglected and the model system applies the element size of $\Delta x = 0.1$ m with 235 elements. The initial mineral composition of the cementitious material (Vieno et al. 1991) is provided in *Table 5-6*. The compositions of groundwater referring to the reference sample OL-KR4_81_1 (Hellä et al. 2014), which is representative of the depth of the repository, and concrete pore water (Höglund et al 2018) are given in *Table 5-7*. It is assumed that any void space, approximately 24 % of the total volume, inside the ILW silo is filled with water before closure either naturally from the surrounding bedrock or manually, so the initial water content in the model waste zone is considered as a mixture of cementitious pore water and groundwater in a 5:8 ratio. Groundwater flow is set from left to right according to *Figure 5-20* and is driven by a hydraulic gradient of 0.005 m/m, which is a conservative value for the Olkiluoto granite, set as a boundary condition on the granite/backfill boundaries. The transport parameters used in the simulations (Alcorn et al. 1991, Vieno et al. 1991, T4.24 D2.16) are provided in *Table 5-8*.

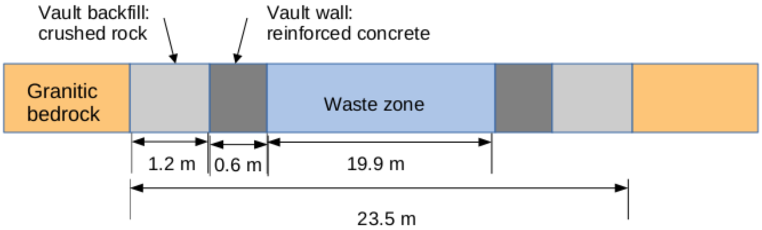

Figure 5-20. 1D representation of the model system considered in the Finnish repository case.

Table 5-6. Composition of groundwater from the reference sample OL-KR4_81_1 (Hellä et al. 2014) and cementitious pore water used in the Finnish repository case (Höglund et al 2018)

Species [mol/l]	Groundwater / backfill	Silo wall
pH	7.8	12.99
pe	-	-8.836
DIC	4.87E-3	2.3E-5
SO4	9.58E-4	3.3E-4
Cl	9.9E-3	5.9E-5
Na	1.31E-2	3.0E-2
K	2.48E-4	9.8E-2
Ca	1.35E-3	3.3E-3
Mg	7.4E-4	2.2E-9
Sr	5.71E-6	-
SiO2	2.00E-4	1.3E-5
Mn	3.46E-6	-
Fe	8.06E-6	3.1E-7
S^{2-}	3.12E-7	-
F	3.16E-5	-
Br	1.75E-5	-
NH4	4.16E-5	-
PO4	1.68E-6	-
B	2.68E-5	-
Al	-	2.70E-5

Table 5-7. Initial mineral composition in cementitious materials (Vieno et al. 1991).

Mineral [mol/kg water]	Silo wall
14 Å tobermorite	0.8130
ettringite	0.0545
Fe-ettringite	0.1380
Hydrogarnet	0.2053
Portlandite	10.0155
NaOH	0.0788
KOH	0.0343
Gypsum	0.4970

*Table 5-8. Transport properties for rock and cementitious materials (Alcorn et al. 1991, Vieno et al. 1991, *scaled linearly as a function of porosity from the base case T4.24 D2.16).*

Material	Backfill	Silo wall	Waste zone
Porosity	0.3	0.15	0.39
D [m²/s]	3.0E-10	1.0E-13	3.86E-10 *
K [m/s]	1.0E-5	1.0E-14	4.09E-7

Figure 5-21 shows the initial mineralogical phases in the ILW disposal cell with the system pH on the right-hand side axis and their evolution up to 50,000 years post-closure. The system exhibits similar behaviour to the reference case starting with portlandite dissolution at the edges of the cementitious material region and related phenomena. However, the degradation of cementitious materials extends further into the waste zone, which is to be expected due to differences in the backfill material. The calculation stopped approximately at 60,000 years when the precipitation of calcite at the outer silo walls decreased porosity toward 0, thus blocking transport pathways. *Figure 5-22* shows the evolution of pH, solute species Ca, Na and K, and porosity in the disposal cell, which are in line with the findings in the reference case.

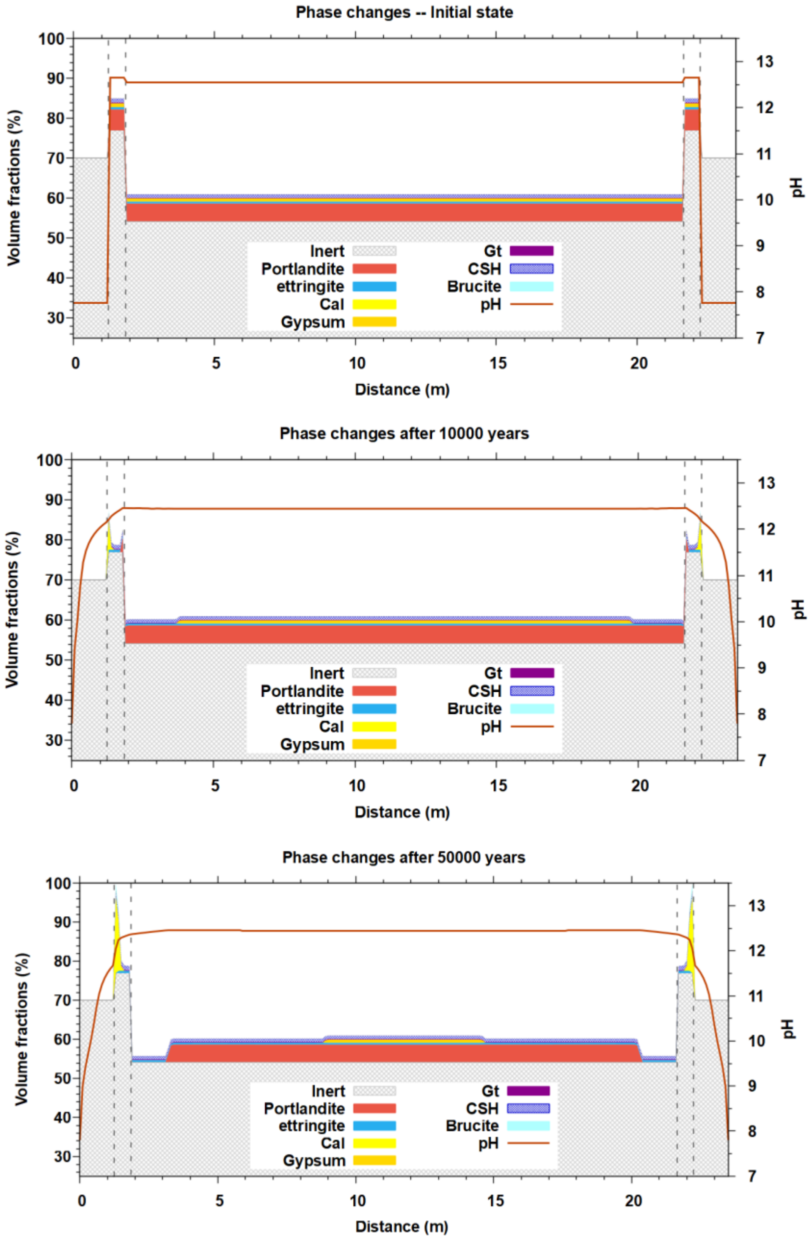

Figure 5-21. The modelled mineralogical evolution of the cementitious materials from the initial state to 50,000 years after closure. CSH includes the six end-members from the CSHQ model. The vertical dashed lines represent the silo walls.

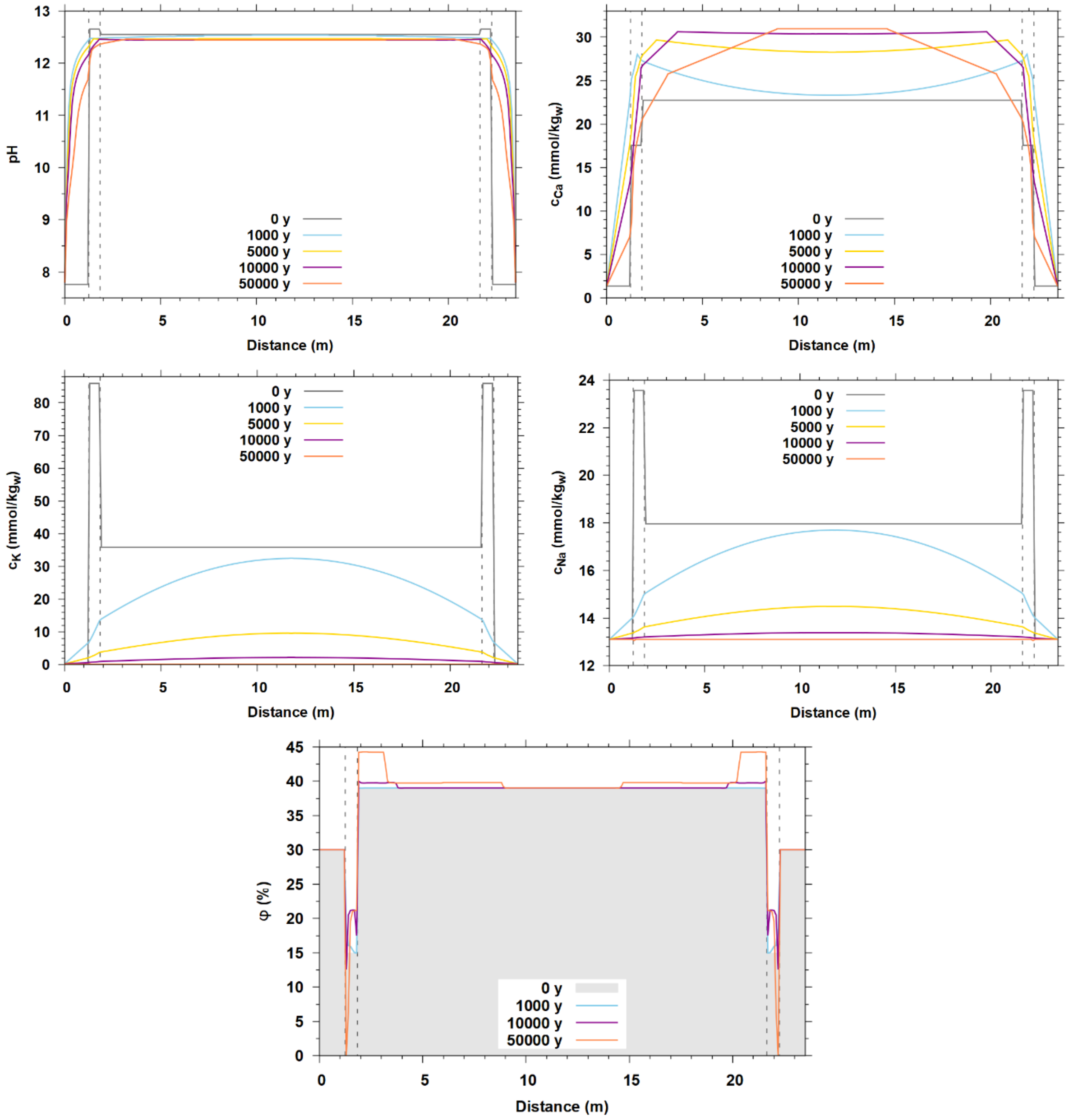

Figure 5-22. The evolution of pH (top left), distribution of dissolved species Ca (top right), K (middle left) and Na (middle right) and porosity (bottom) in the ILW cell in the Finnish case. The initial porosity in the last graph is plotted as a grey area. The vertical dashed lines represent the silo walls.

5.3.3.3 Sensitivity of the predictions to the groundwater flow rate

One of the sensitivity cases analysed in WP2 ACED is water flow rate effect on chemical evolution in the ILW disposal cell in granite. This sensitivity case was constructed to simulate the situation when the groundwater flow is very slow, and the dominant transfer mechanism is diffusion. As an extreme case, the 2D model described in Section 5.3.1.4 was modified assuming no flow conditions around the modelled domain with fixed solution concentration corresponding to granitic host rock pore water composition on the boundaries.

The changes in pH in the modelled region at the certain time steps when transfer only by diffusion is considered are presented in *Figure 5-23*.

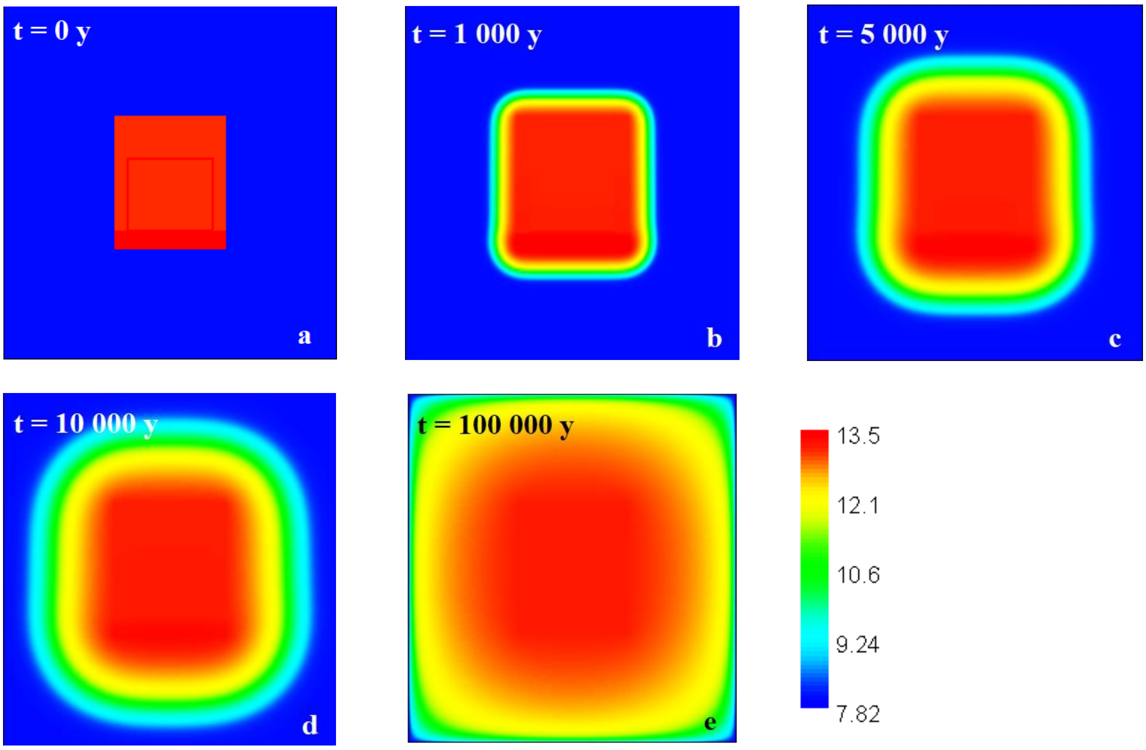

Figure 5-23. pH plots at different time steps for diffusion case: a – 0 years, b – 1,000 years, c – 5,000 years, d – 10,000 years and e – 100,000 years (spatial dimensions: horizontal – 30 meters, vertical – 32 meters).

It can be seen from *Figure 5-23* that propagation of the pH front proceeds almost symmetrically in all directions. Only slightly increased propagation in the bottom part of the tunnel can be observed at the earlier time steps, what is related with the presence of the functional concrete here. In about 100,000 years the pH in the larger part of the modelled region is about 13 or higher.

pH changes in time at the observation points located on the horizontal cross section line in the middle of the waste zone (see position of these points on 1D model in Figure 5-5) are presented in *Figure 5-24*(a). It can be seen from the figure that the pH values at these points located at the same distance from the vertical middle line have the same pH value. Comparison of the pH profile simulated taking into account diffusion and advection transfers with diffusion only case is presented in *Figure 5-24* (b). It is clearly seen from the plot that after 1,000 years the pH front propagates deeper into granite on the right side from the granite-vault backfill boundary when advection is taken into account. However, on the left side the profile is different: when water flow is not taken into account, pH changes are observed further from the tunnel. The same tendency can also be seen for the time step of 100,000 years.

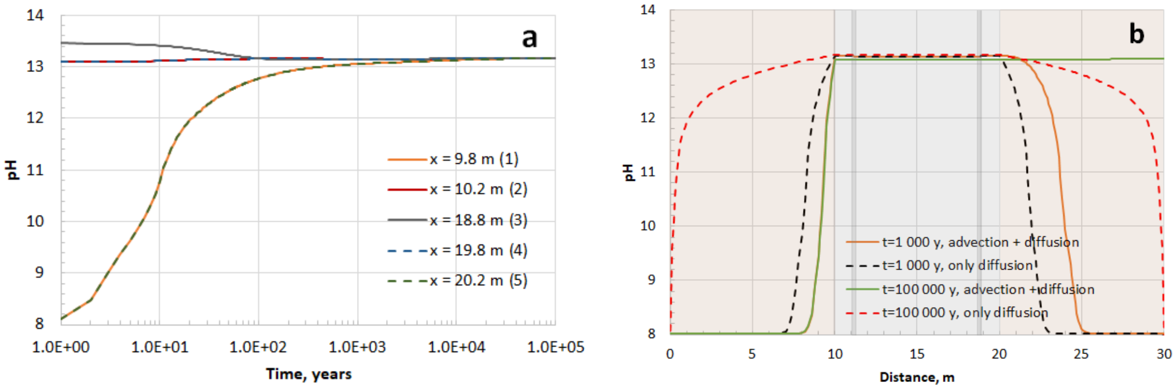

Figure 5-24. pH changes in time at the observation points (a) and comparison of diffusion only case with advection and diffusion case (b).

For investigation of changes in pore water composition, K and Cl concentrations are presented in *Figure 5-25*. In case of K, its concentration in the cement region remains higher when water flow is not taken into account. On the other hand, Cl in diffusion only case penetrates into cement region slower and after 100,000 years its concentration is lower than in the case with advection and diffusion by about one order of magnitude.

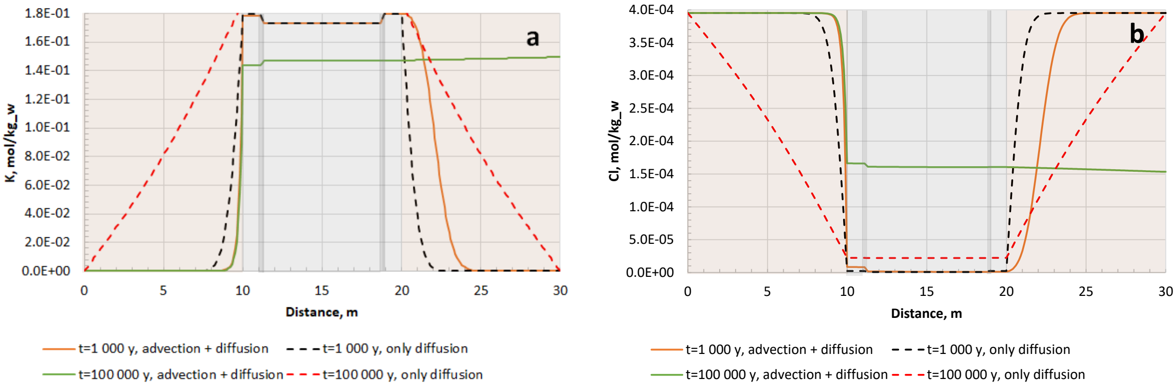

Figure 5-25. Comparison of K (a) and Cl (b) concentration profiles at time steps 1,000 years and 100,000 years depending on water flow consideration.

The changes in the mineralogical composition in the whole modelled domain for the considered time frame were insignificant in the simulation when transfer was assumed to be by diffusion only, therefore no plots are provided.

The comparison of the modelling results taking into account diffusion and advection transfers with diffusion only case indicated that groundwater flow rate could significantly affect the chemical evolution in the analysed disposal cell. The differences are observed not only in the output parameter values, but also in the general nature of their evolution.

5.3.4 Conclusion

A number of lower fidelity (abstracted) models were developed to assess potential chemical evolution of barrier material in the intermediate level waste disposal cell constructed in granitic host rock. The model abstraction included homogenization of the waste zone, simplified geometry, reduced dimensionality and numerical accuracy. In addition, three sensitivity cases with respect to the representation of the waste zone, system layout and groundwater flow regime were analysed. The models considered the system in an initially fully saturated state and each section as homogeneous porous media.

One 1D abstracted model considered chemical evolution in granite and cementitious materials. Advection and diffusion processes as well as minerals dissolution / precipitation were taken into account. It was found that, as a result of cement leaching, the high pH front propagates into granite. The upstream propagation was observed only for a few meters due to competing processes of diffusion and advection, while downstream propagation proceeds much faster and in 5,000 years the pH increases slightly above 13 in the whole modelled granite region downstream from the tunnel. The pH changes in the modelled domain strongly correlates with alkalis leaching. Dissolution and/or formation of minerals in the analysed disposal cell proceeds very slowly. During the modelled period of time, very low dissolution of portlandite and CSH phases as well as formation of calcite were observed. The change of initial mineral concentration in 100,000 years was about 5% or lower. This slow minerals dissolution / precipitation presumably is due to formation of the high pH buffer zone near the granite and vault backfill mortar interface.

Another 1D abstracted model with simplified internal geometry ignored the granitic host rock assuming that the groundwater in granite is unlimited and not altered by the leaching of cementitious barrier. The chemical assessment focused on the cementitious barriers in the model. The porosity and permeability feedback induced by chemical reactions were considered in simulations. Due to the ingress of groundwater and the concentration gradient of elements in pore solutions at the interface among host rock, mortar, and concrete, chemical reactions were initiated leading to chemical gradients. The transformation of portlandite into calcite was found the main degradation phenomenon occurring in cementitious material, which was followed by the decalcification of C-S-H and the formation of calcite. After being exposed for 5,000 years, all portlandite included in vault backfill and waste package backfill were dissolved and the degradation almost reached the container wall. In the meantime, a large amount of calcite was observed accumulated near the border of the considered system reducing the porosity. The mortar degradation extended to the waste zone that was initially filled with backfill mortar over time. The diffusion process was found dominant rather than the advection process, since a relatively higher kinetics of the leaching of species out from cementitious material was observed, compared to the ingress rate of groundwater. This can be further confirmed by the symmetrical mineral profiles in the disposal cell. However, a low hydraulic gradient was applied to simulate the advection process since a very low flow rate of groundwater (2.33E-13 m/s) was considered in the reference case.

The comparison of the two above mentioned 1D abstracted models indicates that the main degradation phenomenon in the cementitious material is dissolution of portlandite, decalcification of C-S-H phases, and the formation of calcite. However, the cementitious barriers degradation rate is considerably slower when granitic host rock is explicitly included in the model as formation of the high pH zone at granite-vault backfill mortar interface plays a significant role. On the other hand, the variant when granitic host rock properties are implemented through the boundary conditions with incorporation of porosity-permeability feedback could be treated as a conservative approach.

In a sensitivity analysis case, the effect of dimensionality was investigated. The differences between the 1D and 2D models were analysed by developing an abstracted 2D model consistent with the abstracted 1D homogenized waste zone model and comparing the results. The highest difference was observed for the components' concentration in the pore water (varying from several per cents to one order of magnitude). The discrepancies in the pH and minerals concentration were less than 15 %. Taking into account that comparison of 1D and 2D model results for such a complex system is not straightforward, there is a sufficiently good agreement between the results. The 2D model can better represent the analysed system as it allows to identify non-homogenous propagation of the high pH front and component transport. However, depending on the modelling purpose, 1D model could be sufficient.

The analysis of the spatial and time-step grid size effect on modelling results indicated that for the analysed system the pH can be sufficiently well modelled with the coarser spatial and time-step grid, therefore saving computational resources. The highest difference between the cases was observed for the components' concentrations in the pore water. In any case, the final selection of the grid size should be consistent with the modelling purpose and tasks.

Sensitivity analyses on the property of the waste zone were performed, where the waste zone was considered as an empty space filled with the pore water of backfill mortar. The degradation kinetics in this case were found faster compared to the case where cementitious material was included in the waste zone. The calculation was stopped soon after being exposed for 20,000 years since the porosity of the area close to the border was approaching 0 and no space was available for transporting the solution. This indicates the importance of placing cementitious material in the waste packages.

In addition, a case considering the ILW repository in Olkiluoto, Finland was studied, the layout of which is composed of waste zone, concrete silo walls, and crushed rock backfill. The system exhibited similar behaviour to other cases starting with portlandite dissolution at the edges of the cementitious material region and related phenomena. However, the degradation of cementitious materials extended further into the waste zone, which was to be expected due to differences in the backfill material.

One more sensitivity case was developed to study the water flow rate effect on chemical evolution in the disposal cell in granite. As an extreme case, a 2D model was constructed assuming no flow conditions allowing only transfer by diffusion. The comparison of the modelling results taking into account diffusion and advection transfers with diffusion only case indicated that groundwater flow rate could significantly affect the chemical evolution in the analysed disposal cell. The differences are observed not only in the output parameter values, but also in the general nature of their evolution.

5.4 Surrogate models

5.4.1 Introduction and scope

In this part we investigate whether we can accelerate reactive transport (RT) simulation by replacing the geochemical solver in the RT code by a surrogate model or emulator, considering either a trained deep neural network (DNN) or a k-nearest neighbor (kNN) regressor, for the abstracted model described in sectin 5.3.

5.4.2 Geochemical systems

The geochemical systems investigated in this study are based on those found in a generic intermediate-level waste disposal cell situated within a granitic host rock, a system also explored in simulations detailed in section 5.3. The repository materials include a cement-based vault backfill mortar, low-porous functional concrete, and the waste zone, which shares the same composition as the mortar. These materials are emplaced within a granitic host rock. Initial mineral phases and pore solution compositions are sourced from D2.16 and are presented again in *Table 5-1*and *Table 5-2*. However, this system exhibits significant complexity, involving primary elements such as C, Ca, Si, Al, Cl, K, Na, Mg, and S. Consequently, in this study, we incrementally increase the complexity by commencing with simpler cement and boundary water chemistry in two distinct test cases.

To begin, a cementitious system comprising only Ca and Si is examined. Primary minerals, namely portlandite and calcium silica hydrate (C-S-H), are included in this system. The calcium silica hydrate is treated as an ideal solid solution with four end members (CSHQ-JenD, CSHQ-JenH, CSHQ-TobD, CSHQ-TobH). This system is brought into contact with a basic pH 8 solution (test case 1). In this scenario, the primary outcome is the leaching of Ca and Si from the backfill without the formation of additional mineral phases.

In the subsequent test case (test case 2), the formation of a calcite precipitate is introduced into the system. Here, the cement system interacts with a solution in equilibrium with calcite, containing a significant concentration of Ca^{2+} and CO_3^{2-}. Consequently, sharp calcite precipitation fronts develop near the interface.

The reactive transport model employed in this study is a 1D diffusive variant inspired on the model described in section 5.3.1.5. Notably, the granitic host rock is not explicitly represented in the model. Instead, a boundary condition of granitic porewater is applied at the interface with the vault backfill. As advection is neglected, modeling only half of the domain is necessary. The thermodynamic database CEMDATA18 (Lothenbach et al. 2019) is used with the Davies equation for the aqueous activity correction factors.

5.4.3 Emulation strategy and implementation

The coupled reactive transport model for leaching of hardened cement paste is implemented in the HP1x (Jacques et al., 2018) code that couples the Hydrus (Simunek et al., 2013) flow simulator with the PHREEQC (Parkhurst and Appelo, 2013) geochemical solver using a sequential non-iterative approach. Transport is calculated for each chemical component, i.e. in terms of total aqueous concentration of the given element. After the independent transport calculations in each time step, geochemical calculations with PHREEQC are done for each grid node to calculate the equilibrium solid phase and aqueous composition. As stated earlier, we test replacing the PHREEQC geochemical solver of HPx by a trained nonlinear regressor which we refer to as an emulator (also called commonly metamodel, surrogate model or proxy model). This follows the approach presented by Laloy and Jacques (2022). For each time step and grid node of a given reactive transport simulation, we emulate the components' aqueous concentrations from the total components' amounts and then re-calculate the components' solid amounts by subtracting for each component the new aqueous concentration from the total amount. The total mass before and after a reactive transport step in a single cell is therefore fully conserved, although because of the emulation error it can be wrongly distributed between solid and aqueous phases.

Our emulators are Python-based and a call to the Python language is introduced within the C/C++ written HPx code. We refer to the resulting HPx variant as HPx_{Py}. When benchmarking against HPx, we consider both the open-mp version where the PHREEQC calculations are parallelized over the physical cores of the computer (in our case 4 cores), that we refer to as four-core HPx or HPx_{4C}, and single-threaded or single-core HPx that we call HPx_{1C}. Regarding terminology, we refer to the HPx-simulated data as ``original" data and the simulated data by $HPx_{Py}$-DNN and $HPx_{Py}$-kNN as emulated data. Importantly, for the problems considered herein transport calculations roughly represent 10 % to 20 % of the total reactive transport simulation time with $HPx_{4C}$. Defining speedup as ``number of times faster", this means that the corresponding maximum possible speedup, which would be obtained if the PHREEQC-based geochemical computations would incur no computational cost at all, ranges between 5 and 10. If HPx_{1C} is used, that is, if all of reactive transport computations are achieved on a single thread, then the runtime fraction associated with transport decreases to between approximately 3 % and 5.5 %, while the associated maximum possible speedup increases to between 18 and 33.

The emulation techniques investigated in this study are k-nearest neighbors (kNN, e.g., Hastie, 2009) and deep neural networks (DNN, e.g., Goodfellow, 2016). The main reason for this choice is that these techniques are very fast while a large prediction speed is needed for the emulator to compete against geochemical solvers such as PHREEQC, which for the considered cement systems and hardware performs about 1000 calculations per second on a single thread (Intel i7 2.70GHz CPU). Furthermore, we deal herein with multi-output regression and both kNN and DNN attempt to honour, in their own distinctive ways, the relationships between the different output targets. That makes kNN and DNN attractive compared to emulation approaches that require training a separate regressor for each output target, which (i) does not leverage any possible relation between targets and (ii) is likely to be slower than multi-output emulators. As further detailed later on, for our cement system 1 (2 inputs - 4 outputs) and 2 (3 inputs - 5 outputs) both kNN and DNN are found to be about 1000 times faster than single-threaded PHREEQC for performing 10,000 calculations. This when both kNN and DNN are ran on a NVIDIA Quadro P6000 GPU.

The kNN technique basically finds a number of similar instances to a presented example within a training base using a given distance measure, and then interpolate between them. Our used kNN regressor for the considered cement system 1 is the the GPU-powered FAISS package for kNN search, using an approximate search method (see Johnson et al., 2017, for algorithmic details). We search for the 5 closest neighbours with respect to the Euclidean distance and perform an inverse-distance weighted interpolation.

Neural networks (NN) basically define the (possibly complex) relationships existing between input, $\mathbf{x}$, and output, $\mathbf{y}$, data vectors by using combinations of computational units that are called neurons. A neuron is an operator of the form

$$h(\mathbf{x}) = f(\langle \mathbf{x}, \mathbf{w} \rangle + b) \qquad [5\text{-}1]$$

where $h(\cdot)$ is the scalar output of the neuron, $f(\cdot)$ is a nonlinear a function that is called the “activation function”, $\langle \cdot,\cdot \rangle$ signifies the scalar product, $\mathbf{w} = [w_1, \dots, w_N]$ is a set of weights of same dimension, N as $\mathbf{x}$ and b represents the bias associated with the neuron. For a given task, the values for $\mathbf{w}$ and b associated with each neuron must be optimized or “learned” such that the resulting neural network performs as well as possible. When $f(\cdot)$ is differentiable, $\mathbf{w}$ and b can be learned by gradient descent. There many possibilities for $f(\cdot)$, common ones include the rectified linear unit (ReLU), sigmoid function and hyperbolic tangent function.

When there is no directed loops or cycles across neurons or combinations thereof, the network is said to be feedforward (FFN). In the FFN architecture, the neurons are organized in layers. In addition, when every neuron of a given layer is connected to every neuron of the preceding layer, the network is referred to as „fully-connected“. In this work, all used NNs are fully-connected FFNs.

A standard fully-connected FFN layer is given by

$$\mathbf{h}(\mathbf{x}) = f(\mathbf{W}\mathbf{x} + \mathbf{b}) \qquad [5\text{-}2]$$

where $\mathbf{W}$ and $\mathbf{b}$ are now a matrix of weights and a vector of biases, respectively. The name multilayer perceptron (MLP) designates a fully-connected FFN with more than one layer. A most typical network is the 2-layer MLP, which consists of two layers with the outputs of the first-layer neurons becoming inputs to the second-layer neurons

$$\mathbf{y} = \mathbf{g}[\mathbf{h}(\mathbf{x})] = f_2\,[\mathbf{W}_2 f_1(\mathbf{W}_1\mathbf{x} + \mathbf{b}_1) + \mathbf{b}_2] \qquad [5\text{-}3]$$

where $\mathbf{g}(\cdot)$ and $\mathbf{h}(\cdot)$ are referred to as output layer and hidden layer, respectively. In theory, the two layer MLP described above is a universal approximator as it can approximate any underlying process between $\mathbf{x}$ and $\mathbf{y}$ (Cybenko, 1989; Hornik, 1991). However, this only works if the dimension of $\mathbf{h}(\cdot)$ is (potentially many orders of magnitudes) larger than that of the input $\mathbf{x}$, thereby making learning practically infeasible and the two-layer MLP approximator useless in many cases. Researchers have found that it is often much more efficient to use many hidden layers rather than increasing the size of a single hidden layer (e.g., Goodfellow et al., 2016). When a FFN/MLP has more than one hidden layer it is considered to be deep. Note that deep neural networks (DNN) are not necessarily purely FFN but may mix different aspects of FFN, such as convolutional neural networks (CNN) with recurrent neural networks (RNN) or transformer neural networks (TNN).

Our selected DNN networks basically consist of a 4-layer FC neural network with rectified exponential linear units (RELUs) as activation functions. The size of our hidden FC layers is 64 and the outputs (aqueous amonts) are logged. Our DNNs are implemented within the pytorch framework (Paszke et al., 2017) and training is performed by stochastic gradient descent with the Adam algorithm (Kingma and

Ba, 2015). All GPU calculations were performed on a NVIDIA Quadro P6000 GPU. Running DNNs and kNN on a GPU (or more if available) is significantly faster than running on CPUs.

5.4.4 Training set creation

A key factor for obtaining accurate ML-accelerated RT simulation results is the creation of a sufficiently representative training set used to train the DNN or run the kNN. Indeed, the exact RT geochemical conditions cannot be known in advance and discrepancies between the geochemical train/test sets used to build the considered ML models and the actual geochemical RT conditions are inevitable. In this study we consider two methods to construct the training set.

1) Our first strategy is simply to randomly sample the input parameter space, a process generally known as Monte Carlo (MC) sampling, while simultaneously trying to have the most uniform coverage of the parameter space. We do that with either latin hypercube sampling (LHS) or low-discrepancy Sobol sequences (for details about these sampling techniques, see, for instance, Lemieux 2009).
2) Our second strategy uses so-called virtual titration experiments to guide the creation of the training set. The main objective is to maximize the inclusion of relevant geochemical conditions compared to a randomly generated range of conditions. This is achieved by incrementally introducing small quantities of boundary porewater solution into a single reactive volume or cell of the porous (cementitious) material. The addition of boundary porewater continues until the material reaches a stable composition This process emulates the diffusive leaching of the material by the boundary solution and effectively generates a comprehensive set of geochemical conditions that closely resemble those encountered in actual reactive transport simulations. Nevertheless, due to the diffusion of species from neighboring cells containing unreacted cementitious material, geochemical conditions may emerge that cannot be replicated solely by mixing with the boundary solution. To account for this, we concurrently introduce a controlled amount of pristine cement water, which compensates for the in-diffusing species originating from the “intact” materials. The resulting dataset is then resampled with replacement using a prescribed variance, to generate a controlled variability around the simulated titration curve(s). This resampled dataset then forms the training set.

Classical strategy 1 and our proposed strategy 2 will be compared in the following results’ sections. When creating the training set different oxide minerals of the constituting primary elements are put together with a given initial amount of water. Importantly, the subsequent geochemical reactions might consume or produce water such that the final free water mass after reactions can be different from the initial one, and this final mass cannot be known in advance. However, RT simulation in cementitious materials is often performed in water-saturated conditions with a constant water mass (constant porosity) that is unavoidably different than those of the training data points. To circumvent this issue, before training and using the ML models we process the initial input training as follows. We optimize the water mass associated with each initial input data point such that the water mass after geochemical reactions is equal to the prescribed water mass of the RT simulation. This is done by means of a local, gradient-based optimization algorithm.

5.4.5 Results for the Ca-Si problem – test case 1

We first present the obtained results for the case when the geochemical emulator is a DNN and our proposed titration-guided creation of the training set is used. Figure 5-26 and Figure 5-27 present the original and ML-accelerated simulated concentration series at 4 observations nodes distributed along the one-dimensional grid, for the 10,000-year period of simulation. Figure 5-28 and Figure 5-29 then present the associated vertical aqueous and solid amount profiles at two times of the simulation: 2000 years and 10,000 years. It is observed that the ML-accelerated simulation results are quite accurate. For this relatively simple geochemical problem, using MC sampling instead our titration-based strategy to train the DNN induce relatively similar results (not shown). However, for the MC sampling some prediction errors appear in node II, which is next to the boundary node I. This is illustrated in Figure 5-30.

With respect to kNN, it observed that to match the quality of the results presented in Figure 5-26 - Figure 5-29, a training base of 10^5 samples is necessary as the reduced training base of 10^4 samples leads to somewhat worse results (not shown). Also, with a training base of 10^5 samples the results derived from MC sampling and titration-based sampling are overall similar. The kNN results are presented in Figure 5-31 - Figure 5-34. Compared to the (titration-derived) DNN results, the kNN-based predictions for node II are less accurate (compare Figure 5-26 with Figure 5-31).

With respect to speedup, running on a GPU both HPx_{Py}-DNN and HPx_{Py}-kNN induce a speedup of 5 (20) against HPx_{4C} (HPx_{1C}). For this problem, the DNN and kNN models are relatively small and similar speedups are found when running the trained DNN and kNN on a CPU.

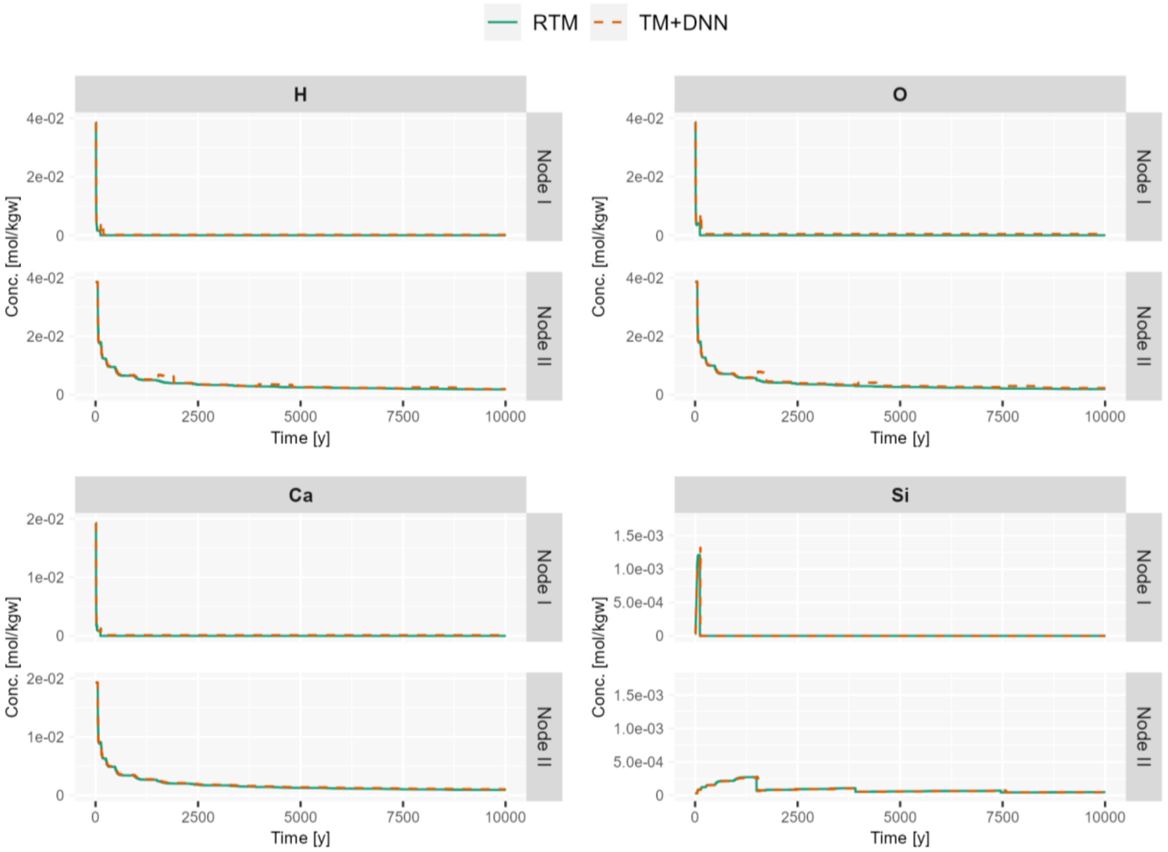

Figure 5-26 *Original (RTM) and DNN-accelerated (TM+DNN) RT simulated concentration time series at 2 observation nodes for test case 1. The observation nodes I and II are the first two nodes (nodes 1 and 2) of the one-dimensional grid and are respectively located at the surface, and depth of 0.025 m in the vault backfill. DNN training was performed using our titration-guided procedure to create the training set, with a total of 1 x 10^5 training samples. Using a reduced training set of of 1 x 10^4 training samples leads to very similar results.*

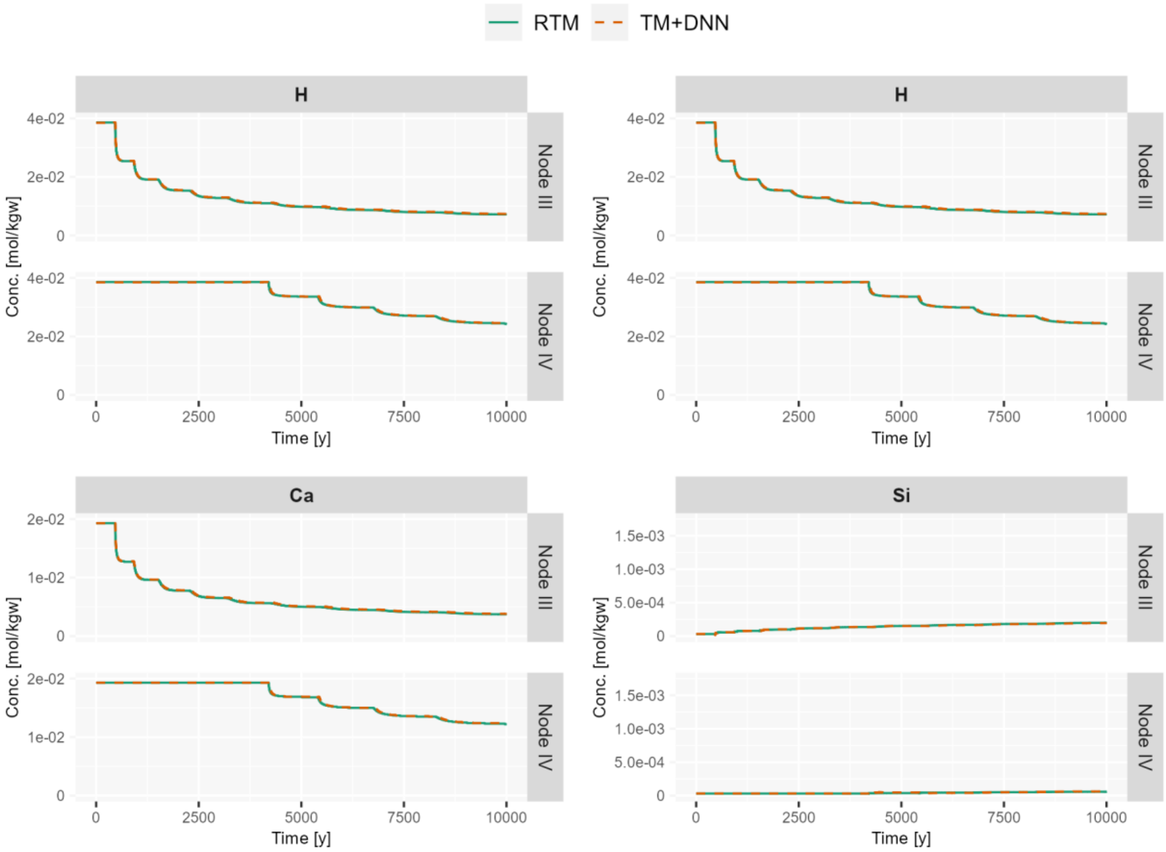

Figure 5-27 *Original (RTM) and DNN-accelerated (TM+DNN) RT simulated concentration time series at 2 observation nodes for test case 1. The observation nodes III and IV are nodes 5 and 10 of the one-dimensional grid and are respectively located at depths of 0.1 m and 0.35 m in the vault backfill. DNN training was performed using our titration-guided procedure, with a total of 1 x 10*^{5} *training samples. Using a reduced training set of of 1 x 10*^{4} *training samples leads to very similar results.*

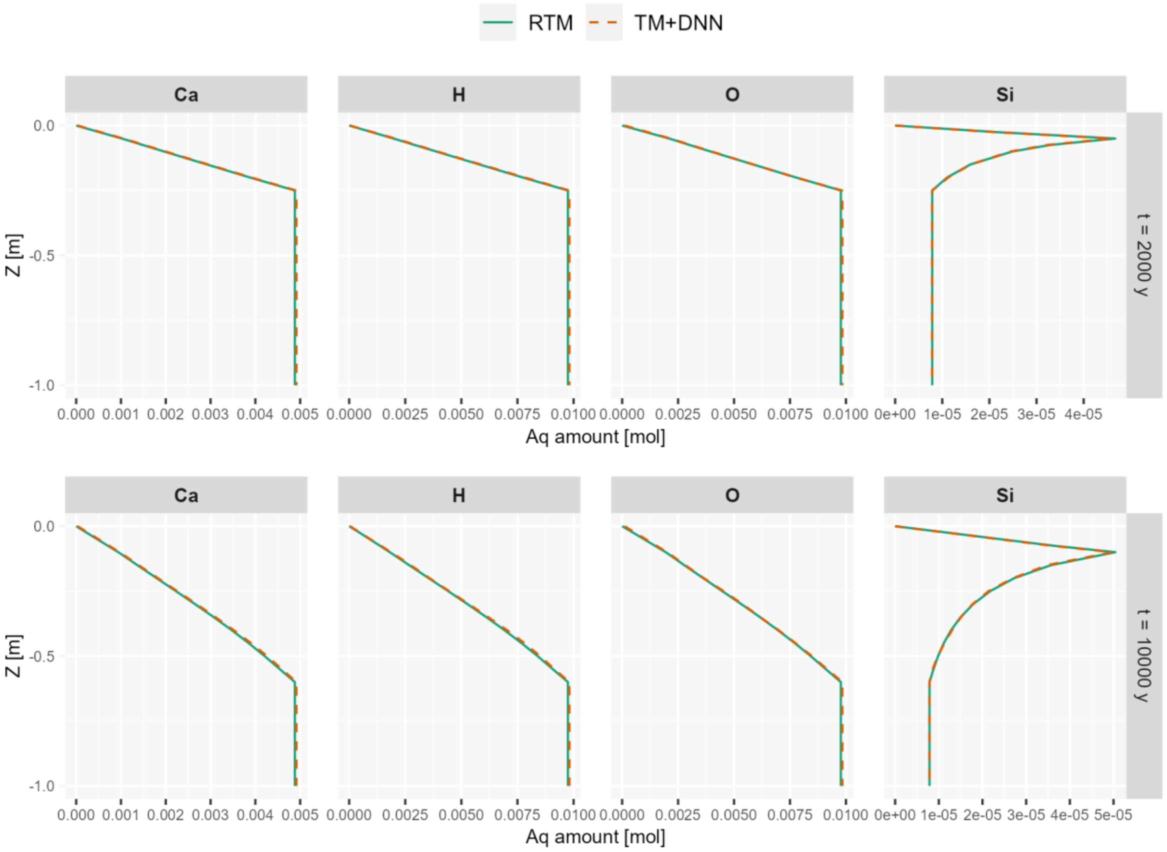

Figure 5-28 *Original (RTM) and DNN-accelerated (TM+DNN) RT simulations of the aqueous amount profiles after 2000 years and 10,000 years, for test case 1. DNN training was performed using our titration-guided procedure, with a total of 1 x 10^5 training samples. Using a reduced training set of 1 x 10^4 training samples leads to very similar results.*

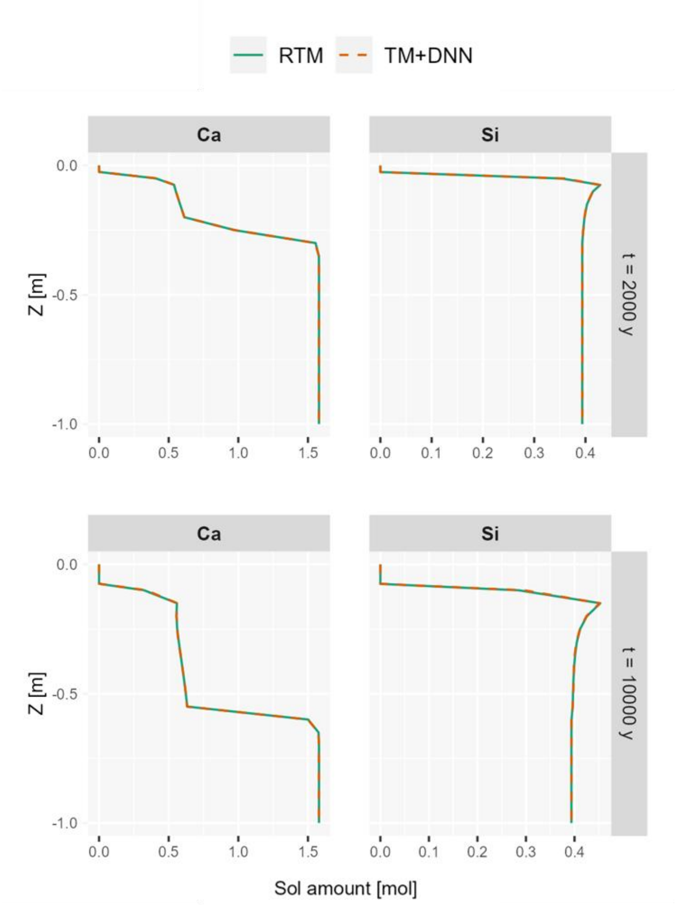

Figure 5-29 *Original (RTM) and DNN-accelerated (TM+DNN) RT simulations of the solid amount profiles after 2000 years and 10,000 years, for test case 1. DNN training was performed using our titration-guided procedure, with a total of 1 x 10^5 training samples. Using a reduced training set of 1 x 10^4 training samples leads to very similar results.*

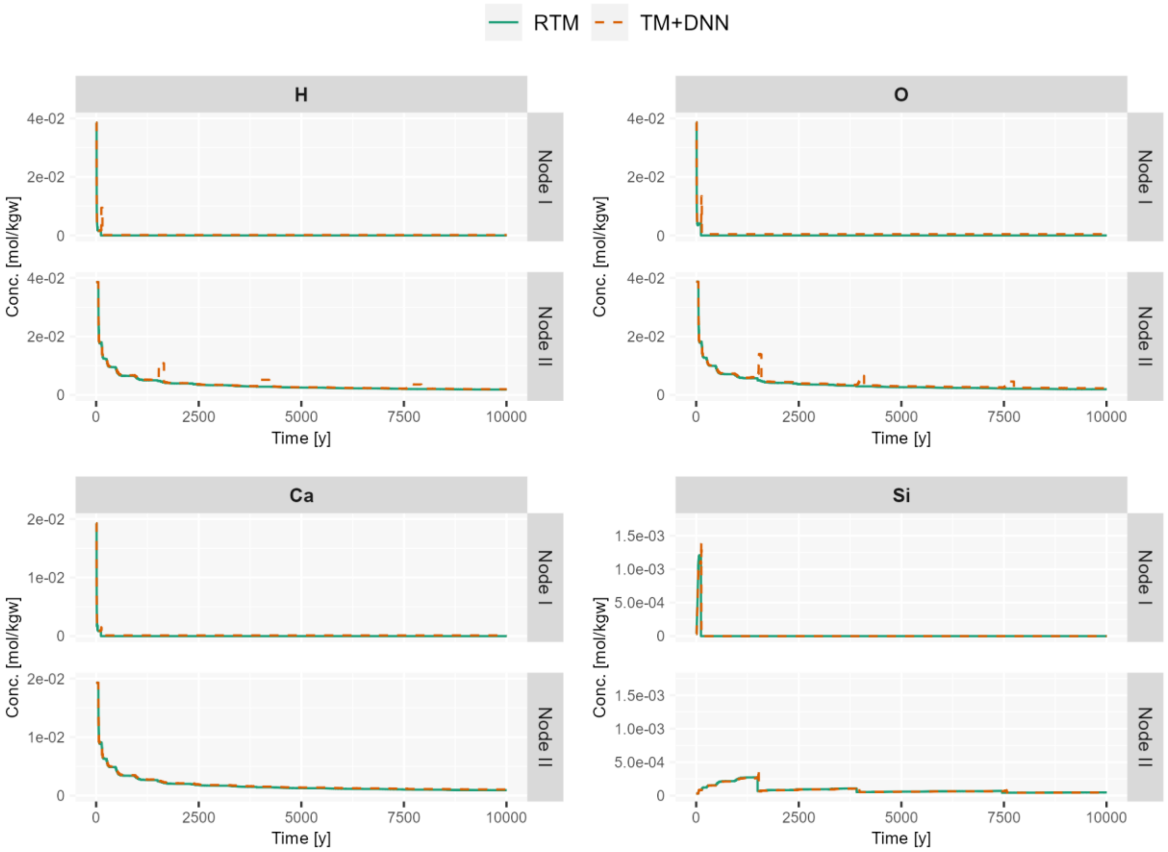

Figure 5-30 *Original (RTM) and DNN-accelerated (TM+DNN) RT simulated concentration time series at 2 observation nodes for test case 1. The observation nodes I and II are the first two nodes (nodes 1 and 2) of the one-dimensional grid and are respectively located at the surface, and depth of 0.025 m in the vault backfill. DNN training was performed using MC sampling (here LHS sampling) to build the training set, with a total of 1 x 10^5 training samples. Using a reduced training set of 1 x 10^4 training samples leads to very similar results.*

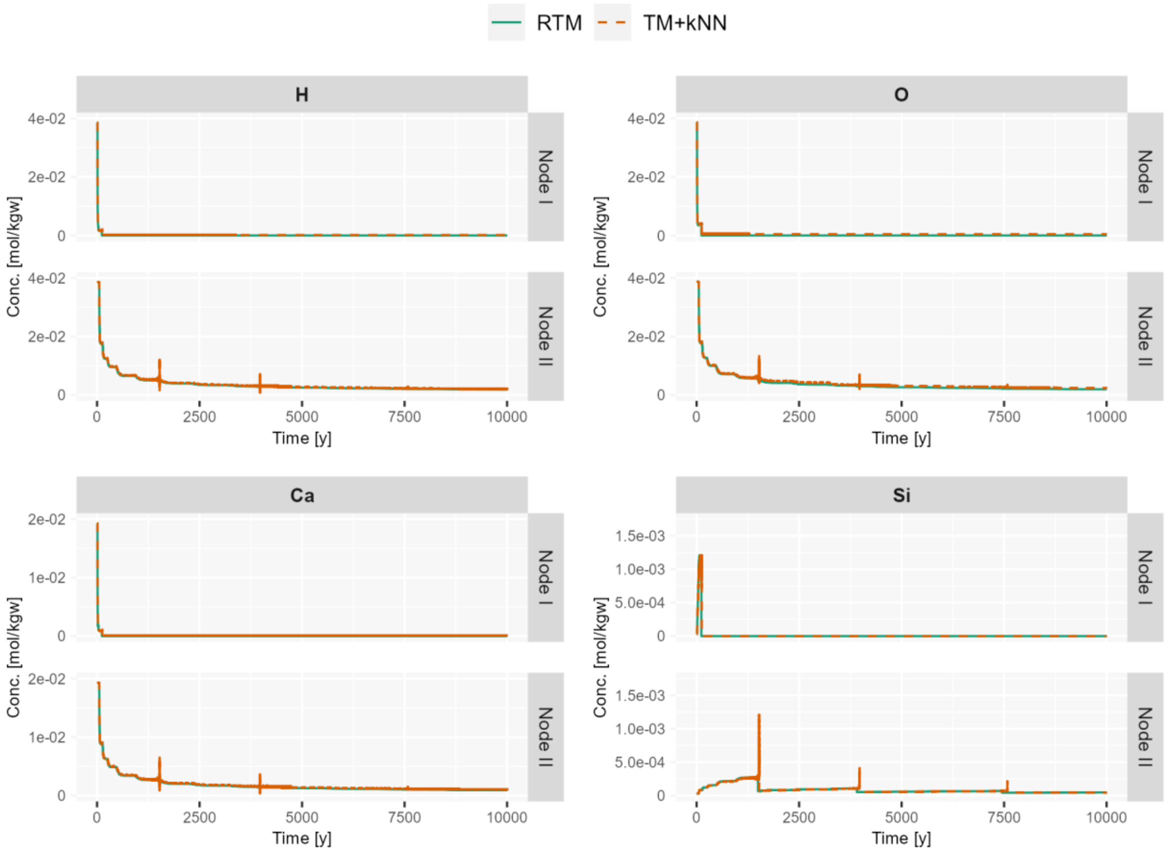

Figure 5-31 *Original (RTM) and kNN-accelerated (TM+kNN) RT simulated concentration time series at 2 observation nodes for test case 1. The observation nodes I and II are the first two nodes (nodes 1 and 2) of the one-dimensional grid and are respectively located at the surface, and depth of 0.025 m in the vault backfill. The kNN training was performed using our titration-guided procedure to create the training set, with a total of 1 x* 10^5 *training samples. Using a reduced training set of 1 x* 10^4 *training samples leads to somewhat worse results.*

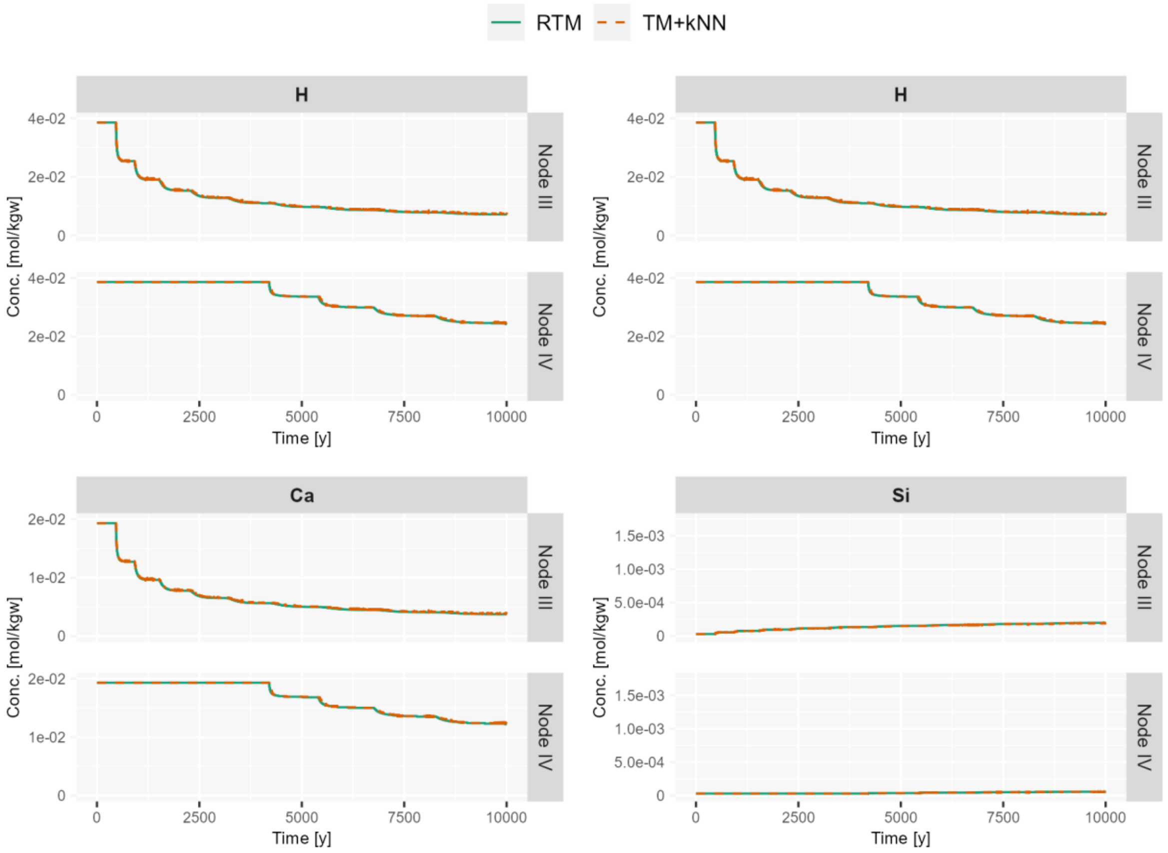

Figure 5-32 *Original (RTM) and kNN-accelerated (TM+kNN) RT simulated concentration time series at 2 observation nodes for test case 1. The observation nodes III and IV are nodes 5 and 10 of the one-dimensional grid and are respectively located at depths of 0.1 m and 0.35 m in the vault backfill. The kNN training was performed using our titration-guided procedure, with a total of 1 x 10^5 training samples. Using a reduced training set of 1 x 10^4 training samples leads to somewhat worse results.*

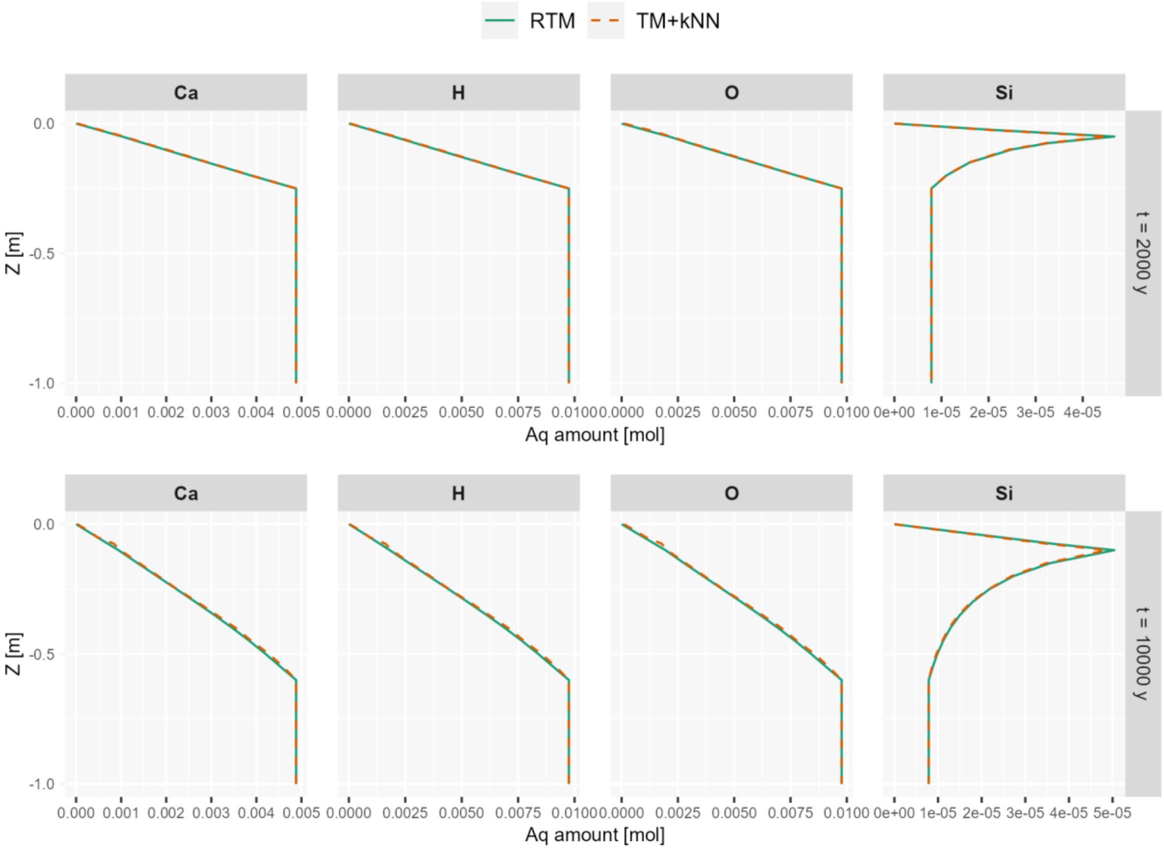

Figure 5-33 *Original (RTM) and kNN-accelerated (TM+kNN) RT simulations of the aqueous amount profiles after 2000 years and 10,000 years, for test case 1. The kNN training was performed using our titration-guided procedure, with a total of 1 x 10^5 training samples. Using a reduced training set of 1 x 10^4 training samples leads to somewhat worse results.*

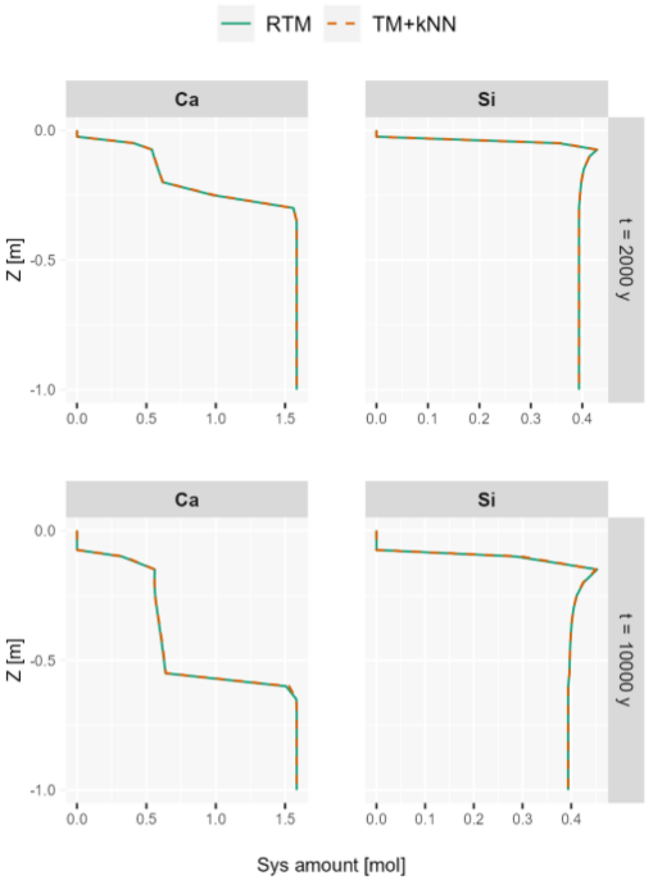

Figure 5-34 *Original (RTM) and kNN-accelerated (TM+kNN) RT simulations of the solid amount profiles after 2000 years and 10,000 years, for test case 1. The kNN training was performed using our titration-guided procedure, with a total of 1 x 10^5 training samples. Using a reduced training set of 1 x 10^4 training samples leads to somewhat worse results.*

5.4.6 Results for the C-Ca-Si problem – test case 2

For this second case study, we tested training our emulators with two training set sizes: 100,000 samples (or “TR100k”) and 2,000,000 samples (or “”TR2000k”). In addition, for the MC-based creation of the training base (strategy 1), we used a Sobol low-discrepancy sequence which offers a more uniform sampling of the hypercube than LHS. With respect to titration-guided strategy (strategy 2), a total of 9 different mixtures of boundary water and pristine cement water (spanning a range from a 90% - 10% mix to a 100% - 90% mix) were used to form the complete training set.

The titration-guided dataset creation leads to overall good results for DNN, especially for the C Ca and Si components, of which the aqueous and solid amount evolutions over time are well reproduced (Figure 5-35 - Figure 5-39). Furthermore, both dissolution (portlandite and CSH) and precipitation (calcite) fronts are perfectly captured (Figure 5-38). Note that the sharp calcite precipitation front near the granite interface is also produced in the simulation with a more detailed chemistry (see Figure 5-11).

Regarding training set size, emulation results do not visually improve much when going from using the TR100k training set to the TR2000k training set (not shown). Therefore, it appears that, for strategy 2, our titration-based TR100k dataset basically contains the same information as our titration-based TR2000k dataset. Still for DNN, somewhat poorer results are obtained when using MC sampling to generate the training base (in the current case a Sobol low-discrepancy scheme), see Figure 5-40 - Figure 5-44. This remains the case even when comparing strategy 1 with TR2000k (not shown) against strategy 2 with TR100k. That said for strategy 1 too, not much difference is noted between TR100k and

TR2000k. This finding is somewhat unexpected as for strategy 1 (that is, in the MC sampling case, whatever the used MC sampling variant), TR2000k offers a better coverage of the hypercube than TR100k. Hence, it may be that the additional points in TR2000k compared to TR100k do not help reproducing well the RTM behavior for the specific RT conditions associated to test case 2. Interestingly, it is seen that with strategy 1 the C and Ca solid amount profiles at the end of the simulation period (Figure 5-43) are not as closely reproduced as with strategy 2 (Figure 5-38). This illustrates the advantage of strategy 2 over the classical strategy 1.

Regarding kNN, we also tested with strategies 1 and 2 and TR100k and TR2000k. Moreover, two algorithm variants were used. A more accurate but slowest search variant for tr100k and less accurate but faster search variant for TR2000k. With these settings, the tr100k and tr2000k based searches incurred approximately the same computational cost and offered a globally similar accuracy. In contrast, combining the more accurate but slowest variant with tr2000k led to more accurate results (not shown) but provided no computational gain at all compared to simply running the original RTM.

Overall and even more than for DNN, combining kNN with strategy 2 (kNN-2) appears to be a better option than combining kNN with strategy 1 (kNN-1). This can be seen by comparing Figure 5-45 - Figure 5-49 on the one hand (strategy 2), and Figure 5-50 - Figure 5-54 on the other hand (strategy 1). More specifically, it is observed that kNN-1 misses the solid amount peaks in the upper part of the profile for Ca and C (Figure 5-53) while kNN-2 is able to grasp them to some extent (Figure 5-48).

Overall, for this case study and the considered DNN and kNN parameterizations, DNN-2 appears to work better than DNN-1, kNN-1 and kNN-2 for jointly emulating the 5 outputs, KNN-2 being the runner-up. With respect to speedup, running the ML-accelerated RT simulation on a GPU, HPx_{Py}-DNN induces a speedup of about 5.5 (22) against HPx_{4C} (HPx_{1C}) while for this case study HPx_{Py}-kNN is a bit slower with a speedup of about 4 (16) against HPx_{4C} (HPx_{1C}).

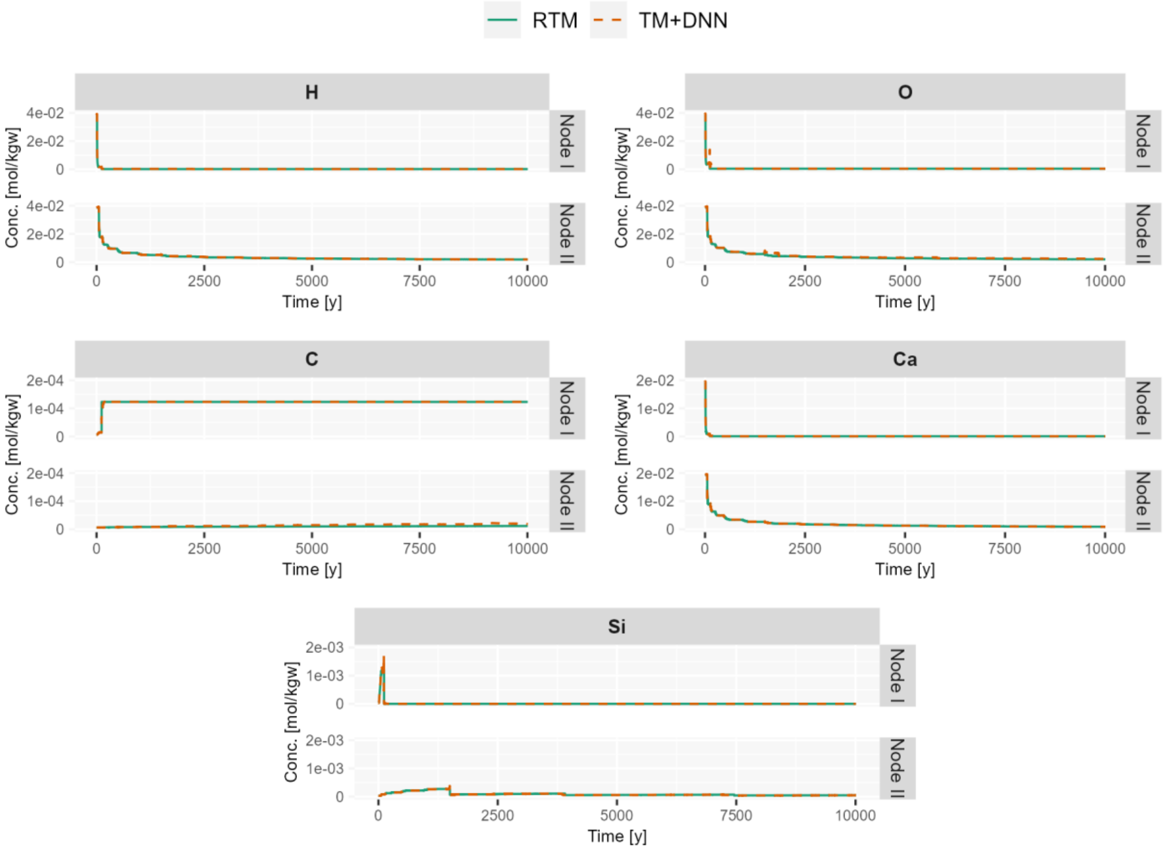

Figure 5-35 *Original (RTM) and DNN-accelerated (TM+DNN) RT simulated concentration time series at 2 (out of the considered 6) observation nodes for test case 2. The observation nodes I and II are the first two nodes of the one-dimensional grid (nodes 1 and 2) and are respectively located at the surface and depth of 0.025 m in the vault backfill. The DNN training base was built using our titration-guided procedure using a total of 1 x 10^5 training samples.*

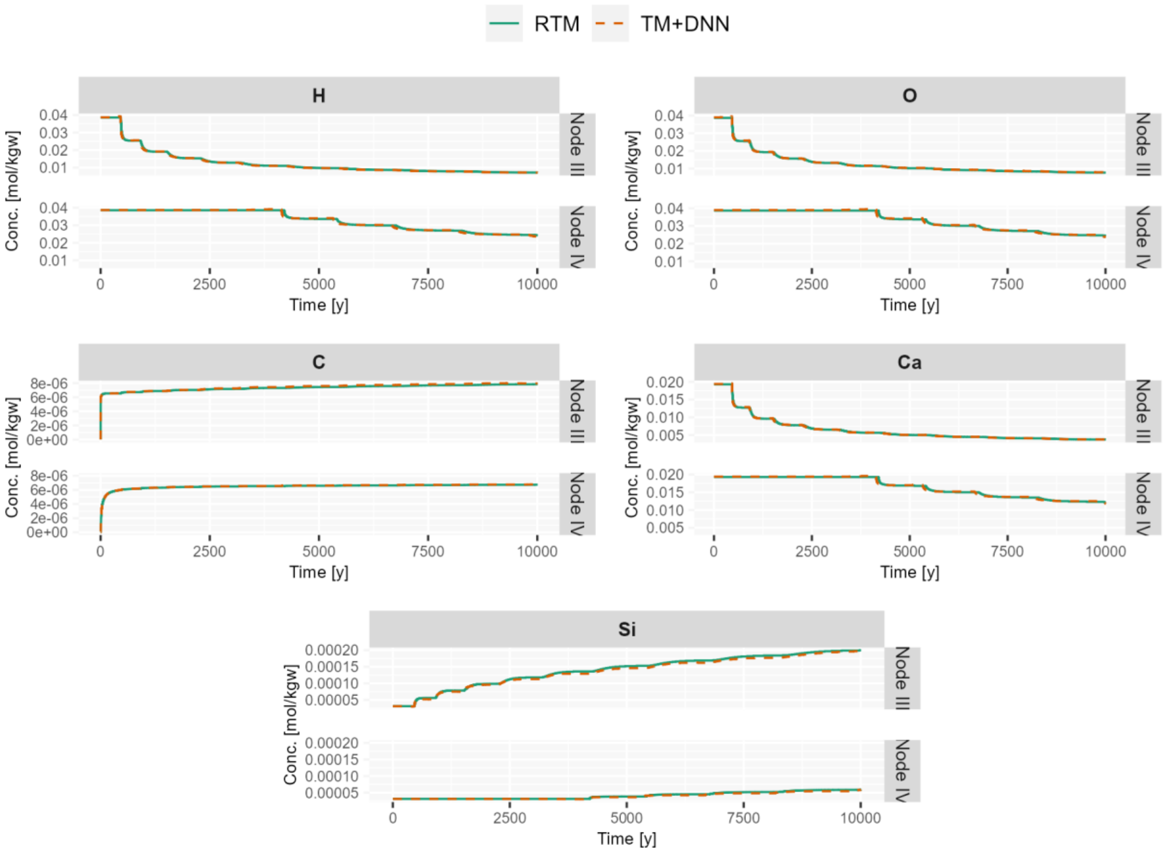

Figure 5-36 *Original (RTM) and DNN-accelerated (TM+DNN) RT simulated concentration time series at 2 (out of the considered 6) observation nodes for test case 2. The observation nodes III and IV are nodes 5 and 10 of the one-dimensional grid and are respectively located at depths of 0.1 m and 0.35 m in the vault backfill. The DNN training base was built using our titration-guided procedure using a total of 1 x 10^5 training samples.*

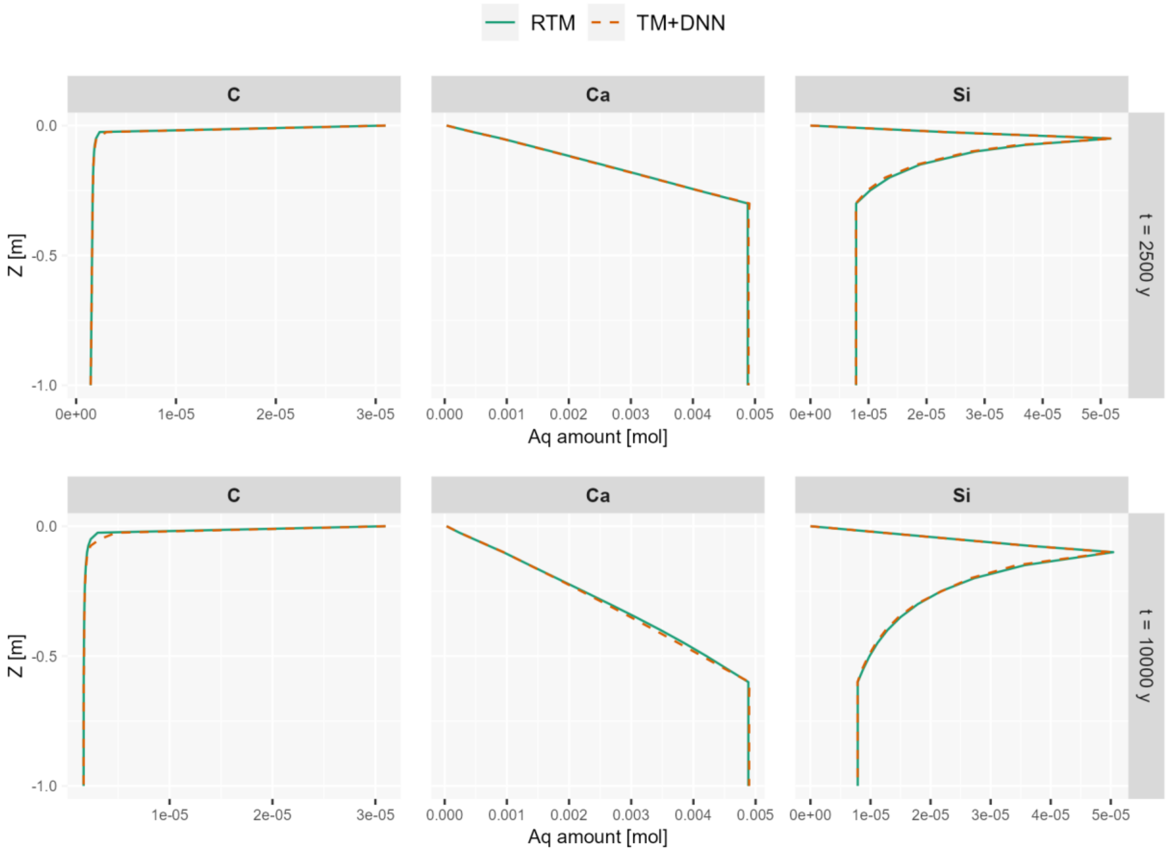

Figure 5-37 *Original (RTM) and DNN-accelerated (TM+DNN) RT simulations of the C, Ca and Si aqueous amount profiles after 2500 years and 10,000 years, for test case 2. The DNN training base was built using our titration-guided procedure using a total of 1 x 10^5 training samples.*

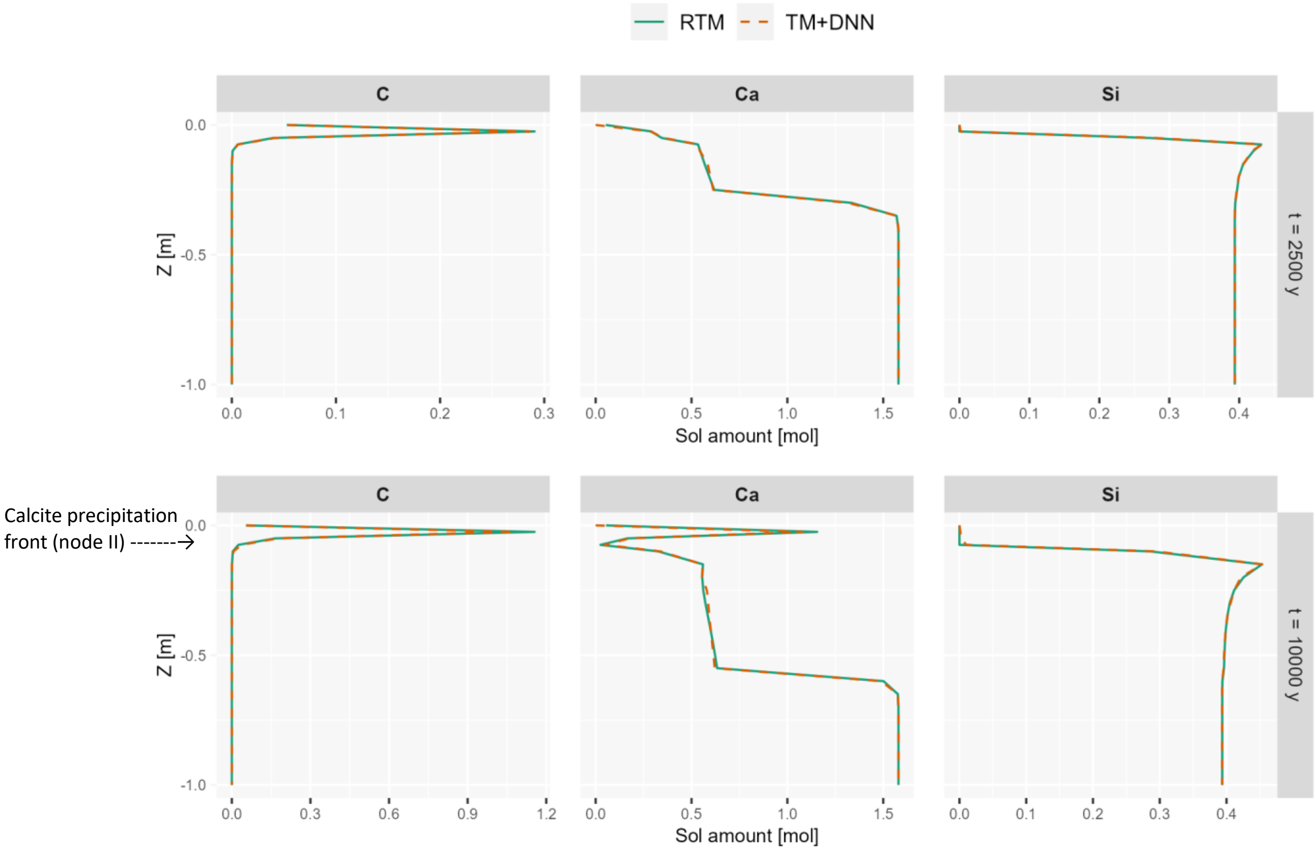

Figure 5-38 *Original (RTM) and DNN-accelerated (TM+DNN) RT simulations of the C, Ca and Si solid amount profiles after 2500 years and 10,000 years, for test case 2. The DNN training base was built using our titration-guided procedure using a total of 1 x 10^5 training samples.*

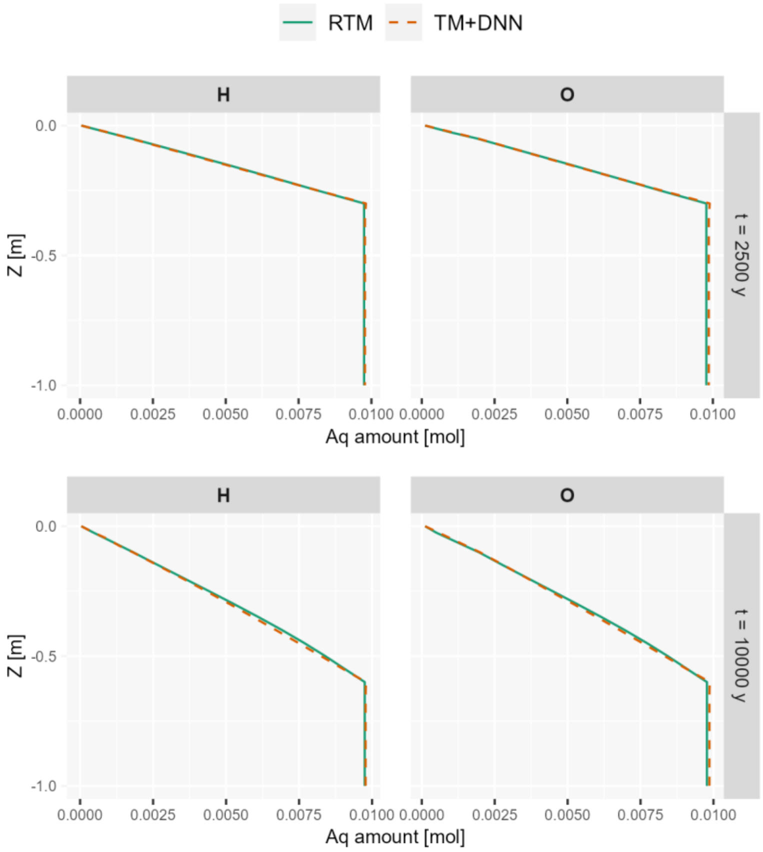

Figure 5-39 *Original (RTM) and DNN-accelerated (TM+DNN) RT simulations of the H and O aqueous amount profiles after 2500 years and 10,000 years, for test case 2. The DNN training base was built using our titration-guided procedure using a total of 1 x* 10^5 *training samples.*

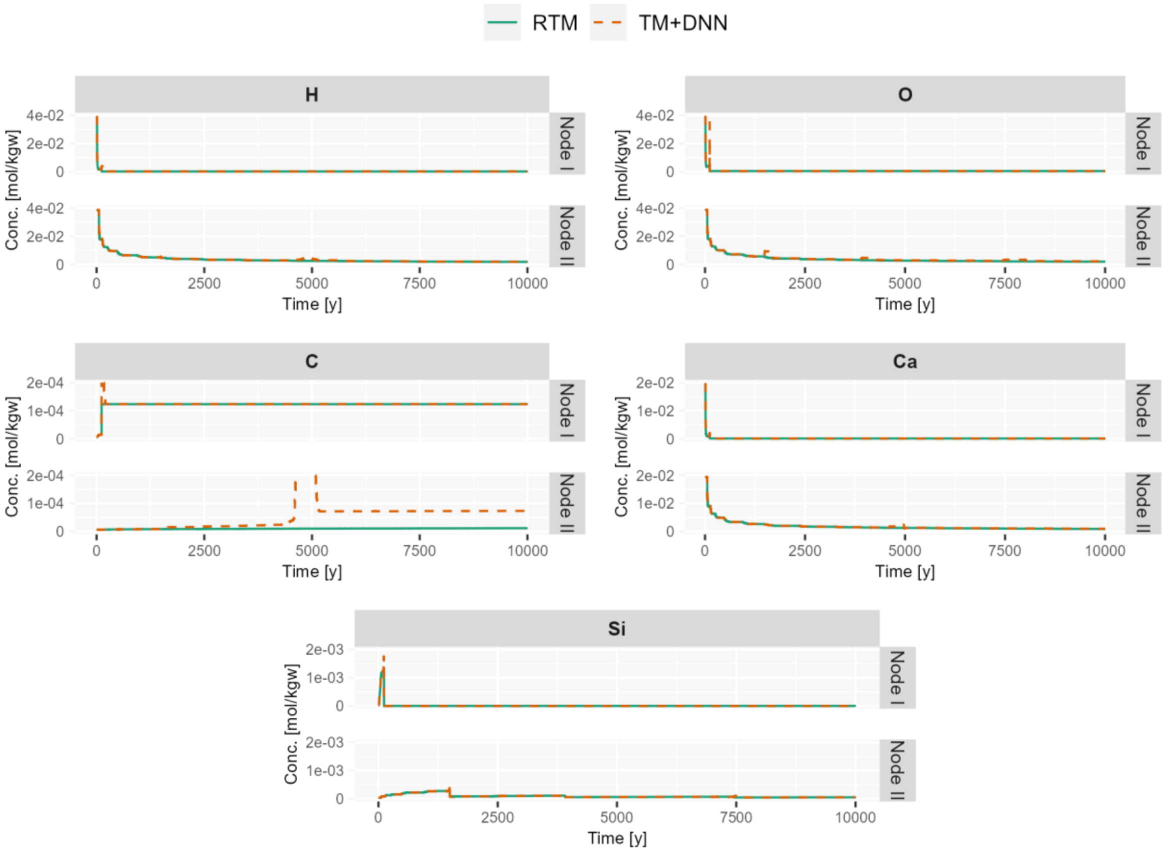

Figure 5-40 *Original (RTM) and DNN-accelerated (TM+DNN) RT simulated concentration time series at observation nodes I and II for test case 2. The observation nodes I and II are the two first nodes of the one-dimensional grid (nodes 1 and 2) and are respectively located at the surface and depth of 0.025 m in the vault backfill. The DNN training base was built using a Sobol low-discrepancy sequence of 1 x 10^5 training samples.*

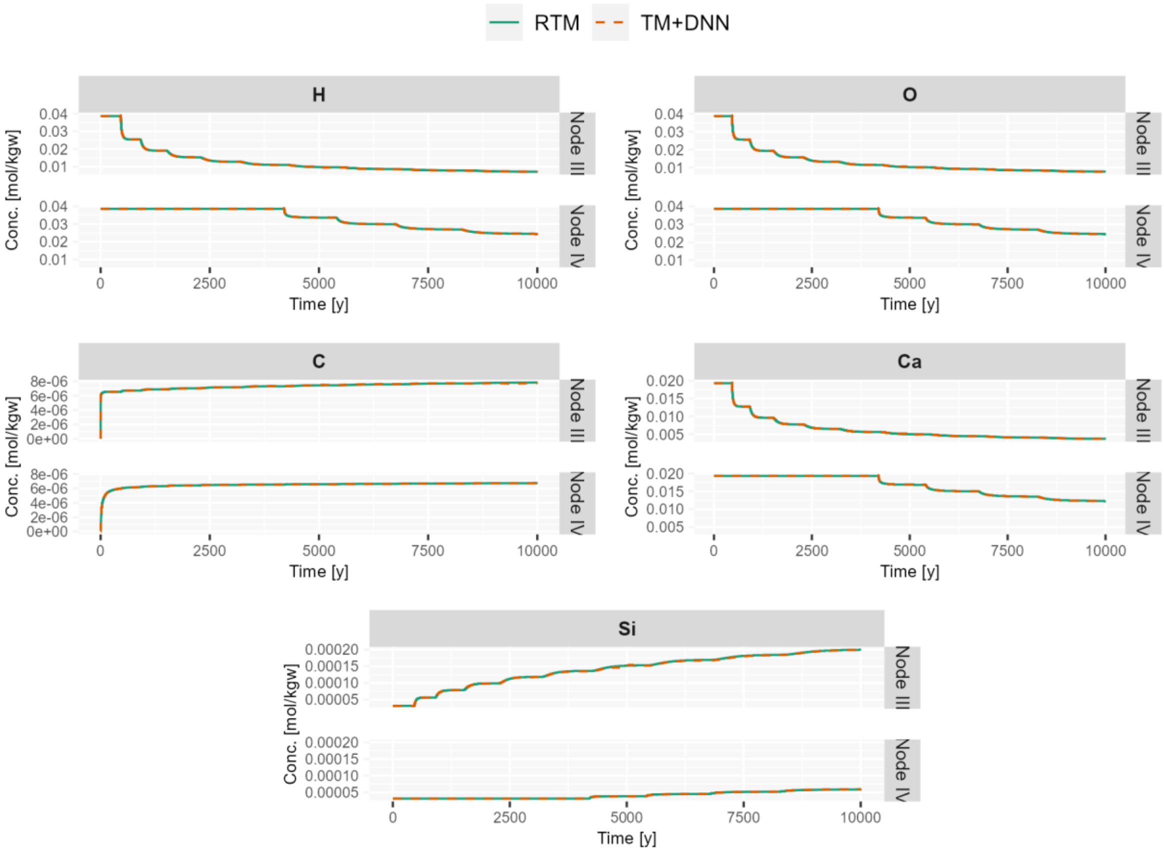

Figure 5-41 *Original (RTM) and DNN-accelerated (TM+DNN) RT simulated concentration time series at 2 (out of the considered 6) observation nodes for test case 2. The observation nodes III and IV are respectively located at depths of 0.1 m and 0.35 m in the vault backfill. The DNN training base was built using a Sobol low-discrepancy sequence of 1 x 10^5 training samples.*

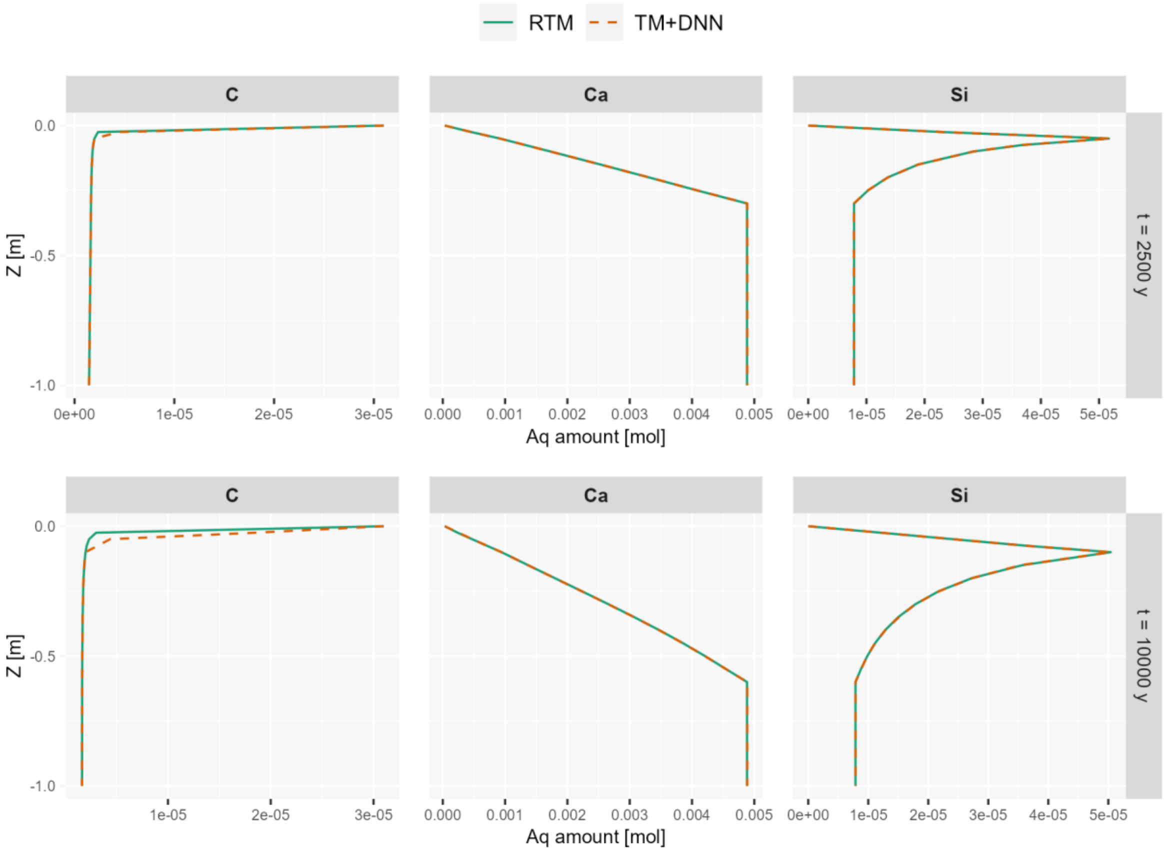

Figure 5-42 *Original (RTM) and DNN-accelerated (TM+DNN) RT simulations of the C, Ca and Si aqueous amount profiles after 2500 years and 10,000 years, for test case 2. The DNN training base was built using a Sobol low-discrepancy sequence of 1 x 10^5 training samples.*

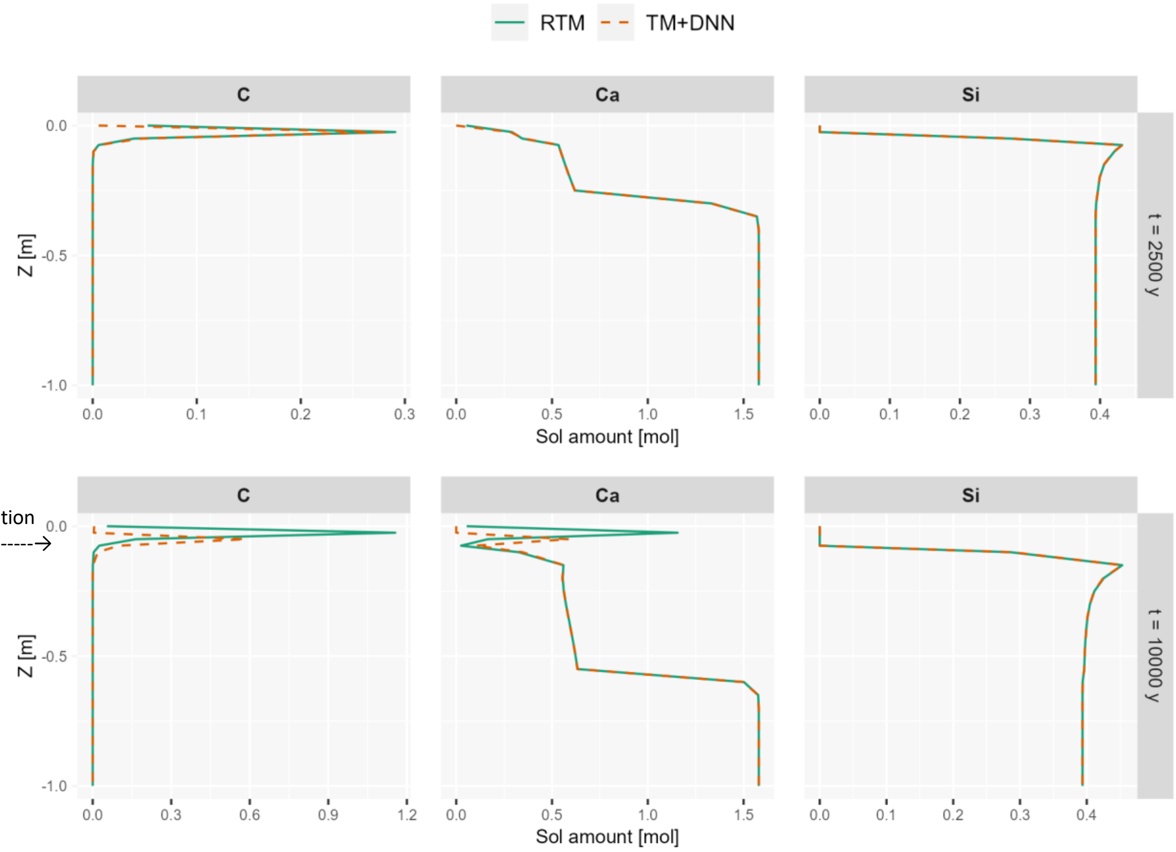

Calcite precipitation front (node II) -------→

Figure 5-43 *Original (RTM) and DNN-accelerated (TM+DNN) RT simulations of the C, Ca and Si solid amount profiles after 2500 years and 10,000 years, for test case 2. The DNN training base was built using a Sobol low-discrepancy sequence of 1 x 10^5 training samples.*

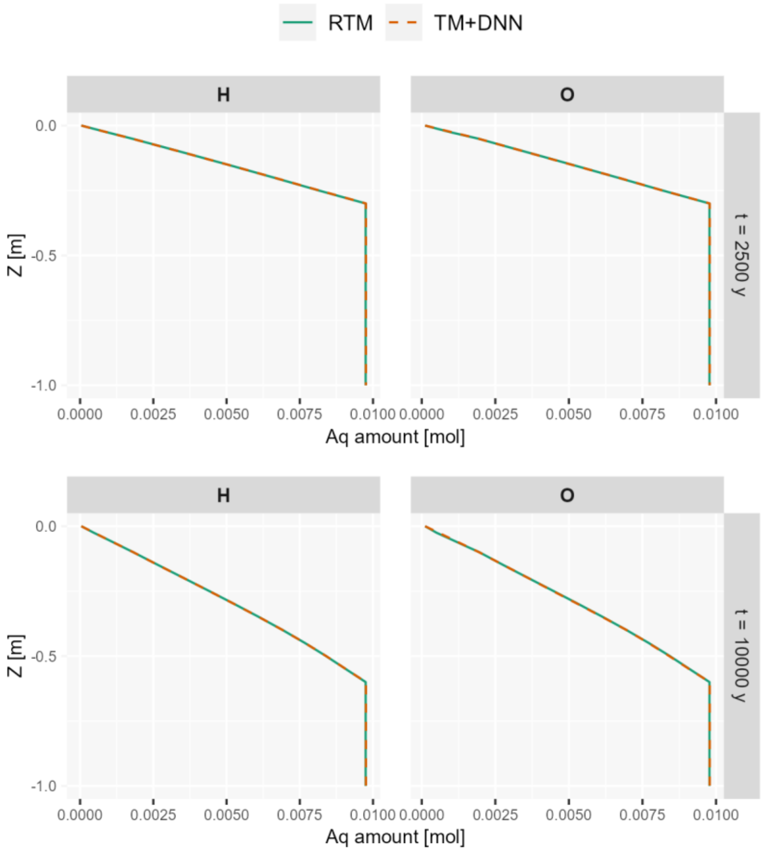

Figure 5-44 *Original (RTM) and DNN-accelerated (TM+DNN) RT simulations of the H and O aqueous amount profiles after 2500 years and 10,000 years, for test case 2. The DNN training base was built using a Sobol low-discrepancy sequence of 1 x* 10^5 *training samples.*

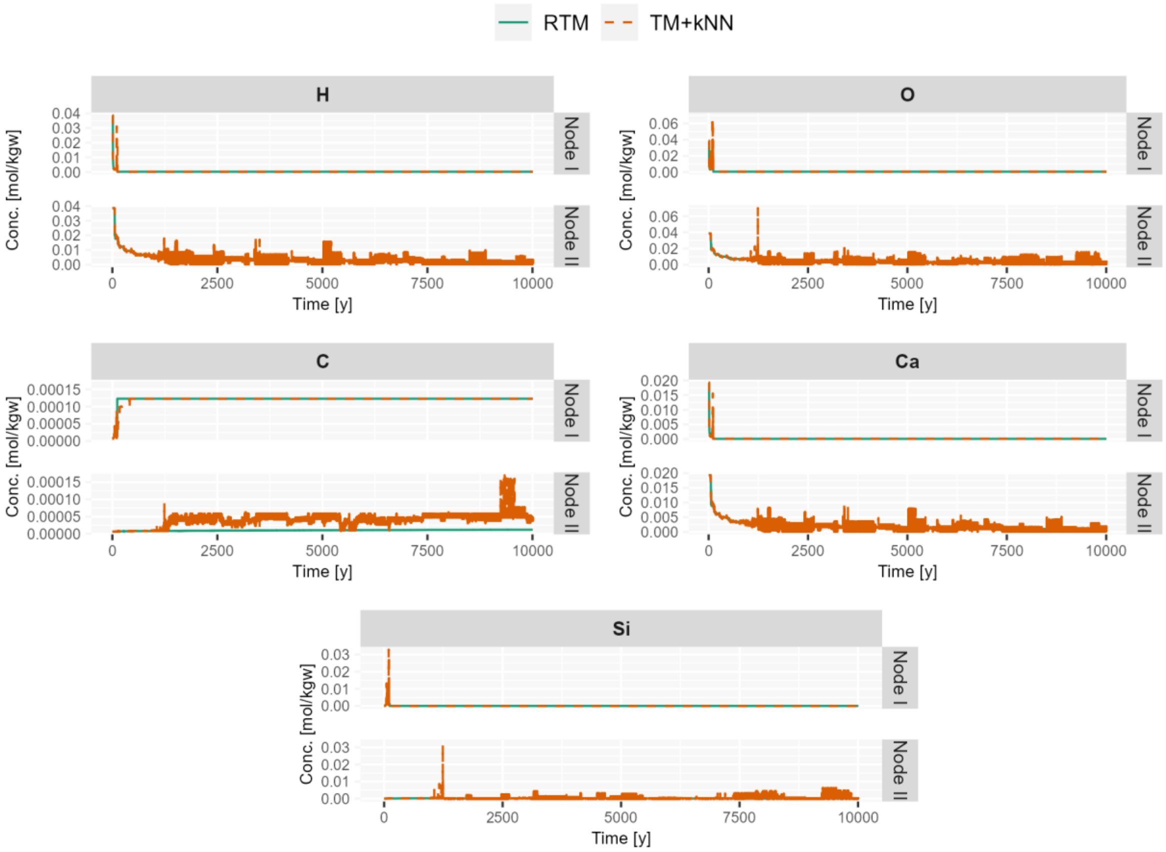

Figure 5-45 *Original (RTM) and kNN-accelerated (TM+kNN) RT simulated concentration time series at observation nodes I and II. The observation nodes I and II are the first two nodes of the one-dimensional grid (nodes 1 and 2) and are respectively located at the surface and depth of 0.025 m in the vault backfill. The kNN training base was built using our titration-guided procedure. using a total of 1 x 10*^{5} *training samples.*

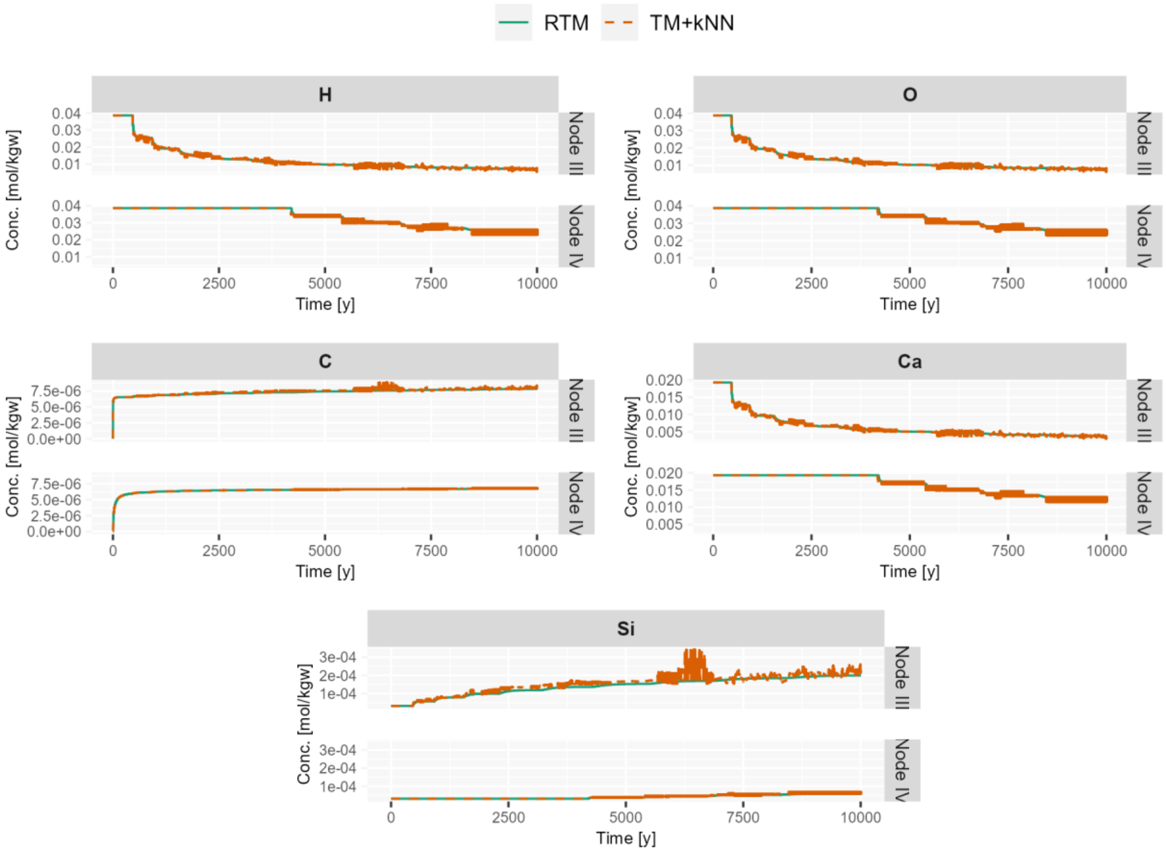

Figure 5-46 *Original (RTM) and kNN-accelerated (TM+kNN) RT simulated concentration time series at 2 (out of the considered 6) observation nodes for test case 2. The observation nodes III and IV are nodes 5 and 10 of the one-dimensional grid and are respectively located at depths of 0.1 m and 0.35 m in the vault backfill. The kNN training base was built using our titration-guided procedure. using a total of 1 x 10^5 training samples.*

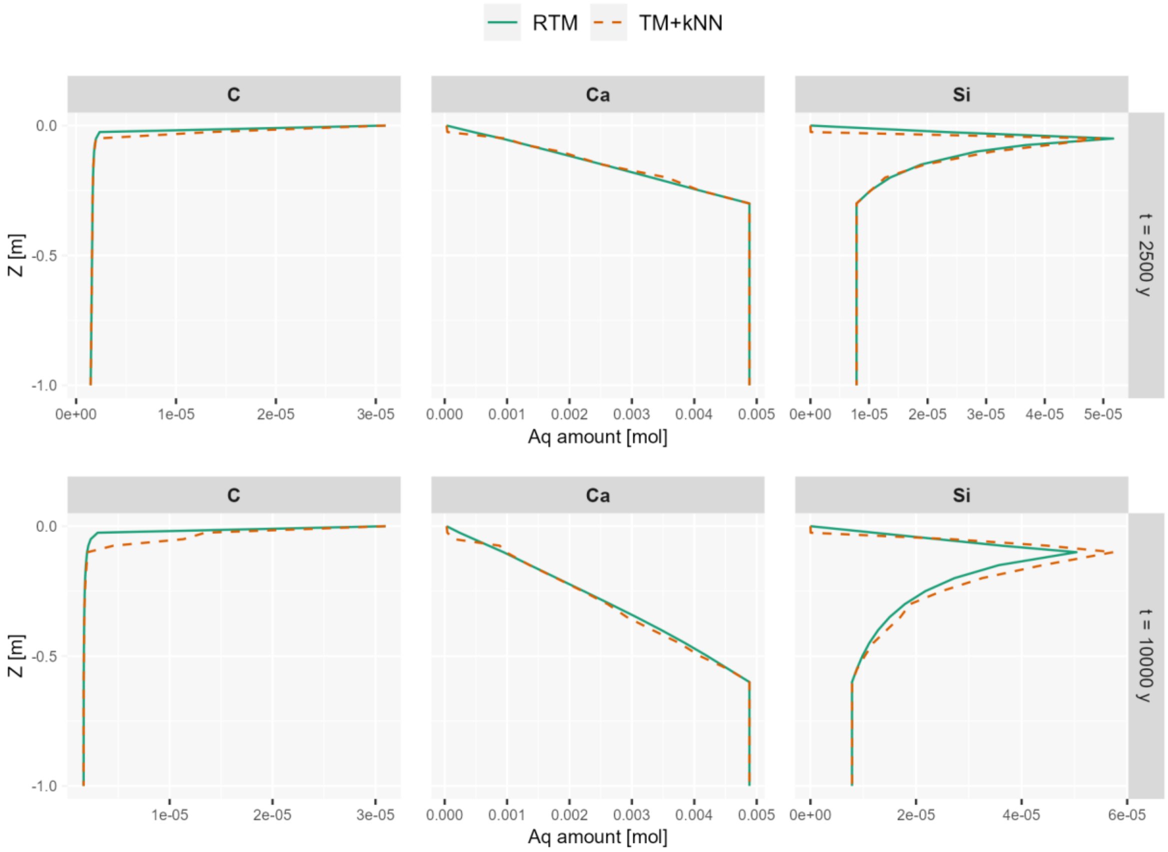

Figure 5-47 *Original (RTM) and kNN-accelerated (TM+kNN) RT simulations of the C, Ca and Si aqueous amount profiles after 2500 years and 10,000 years, for test case 2. The kNN training base was built using our titration-guided procedure. using a total of 1 x 10*^{5} *training samples.*

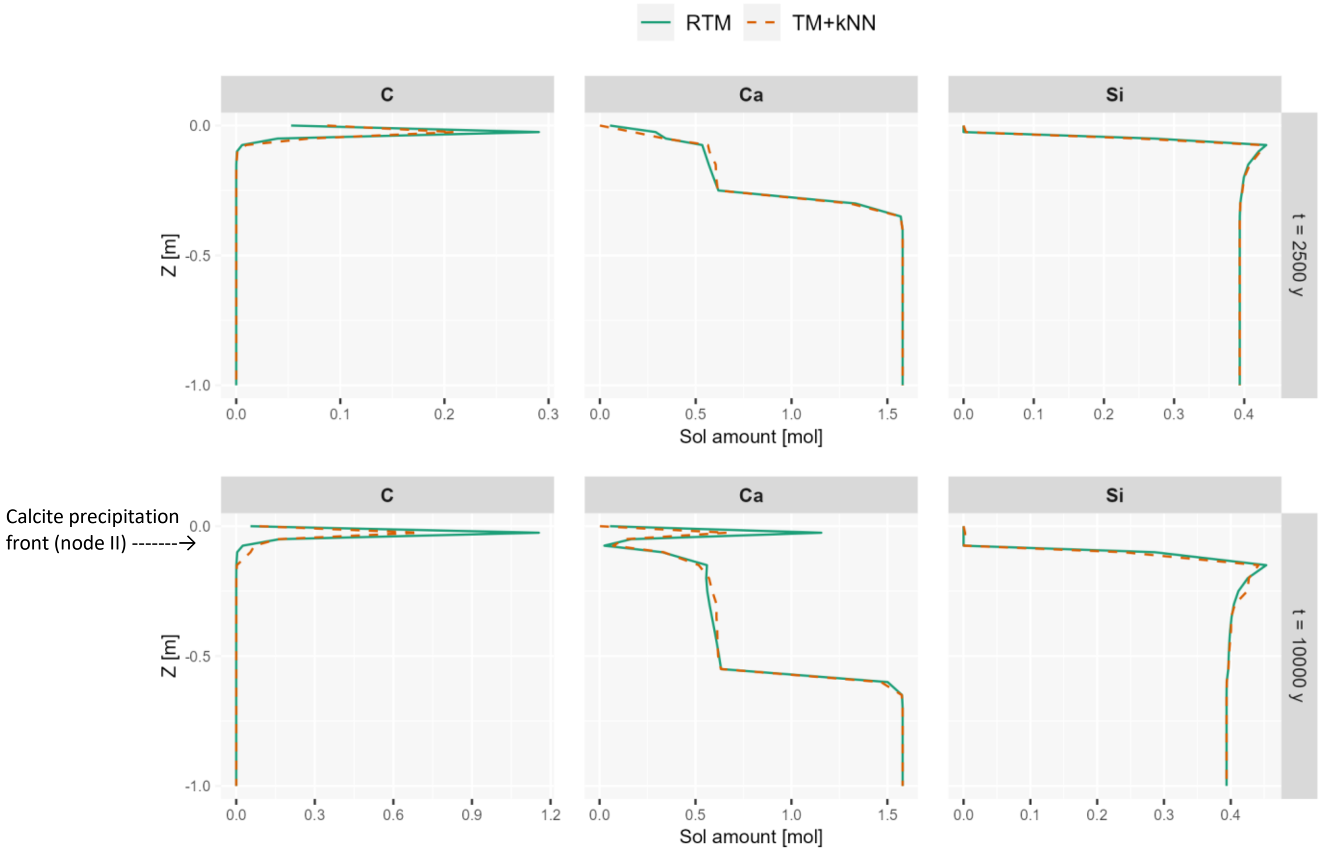
Calcite precipitation front (node II) ------->

Figure 5-48 *Original (RTM) and kNN-accelerated (TM+kNN) RT simulations of the C, Ca and Si solid amount profiles after 2500 years and 10,000 years, for test case 2 The kNN training base was built using our titration-guided procedure. using a total of 1 x 10^5 training samples.*

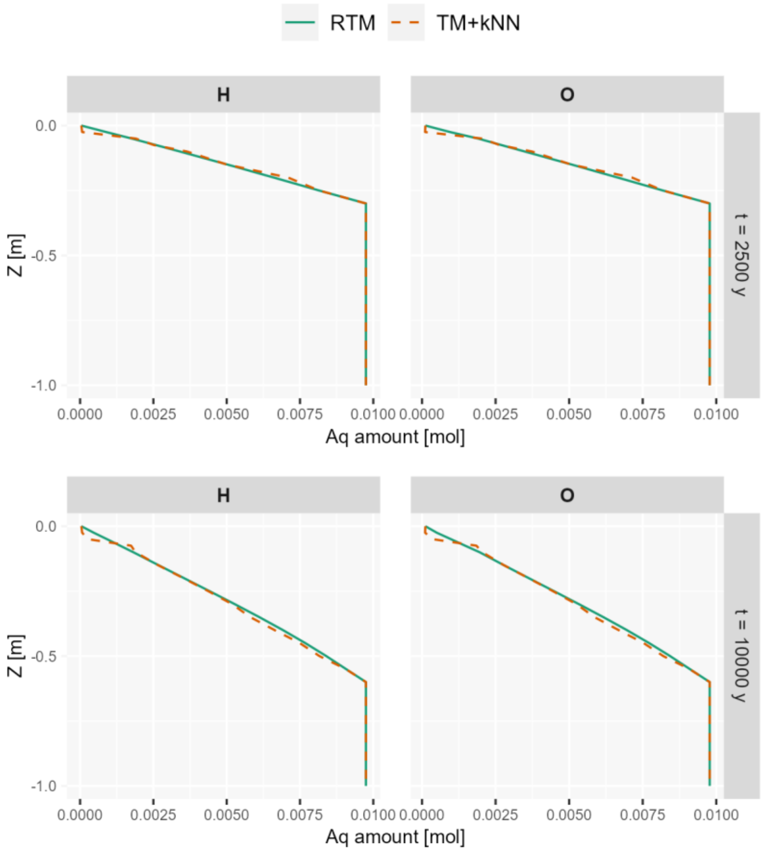

Figure 5-49 *Original (RTM) and kNN-accelerated (TM+kNN) RT simulations of the H and O aqueous amount profiles after 2500 years and 10,000 years, for test case 2. The kNN training base was built using our titration-guided procedure. using a total of 1 x* 10^5 *training samples.*

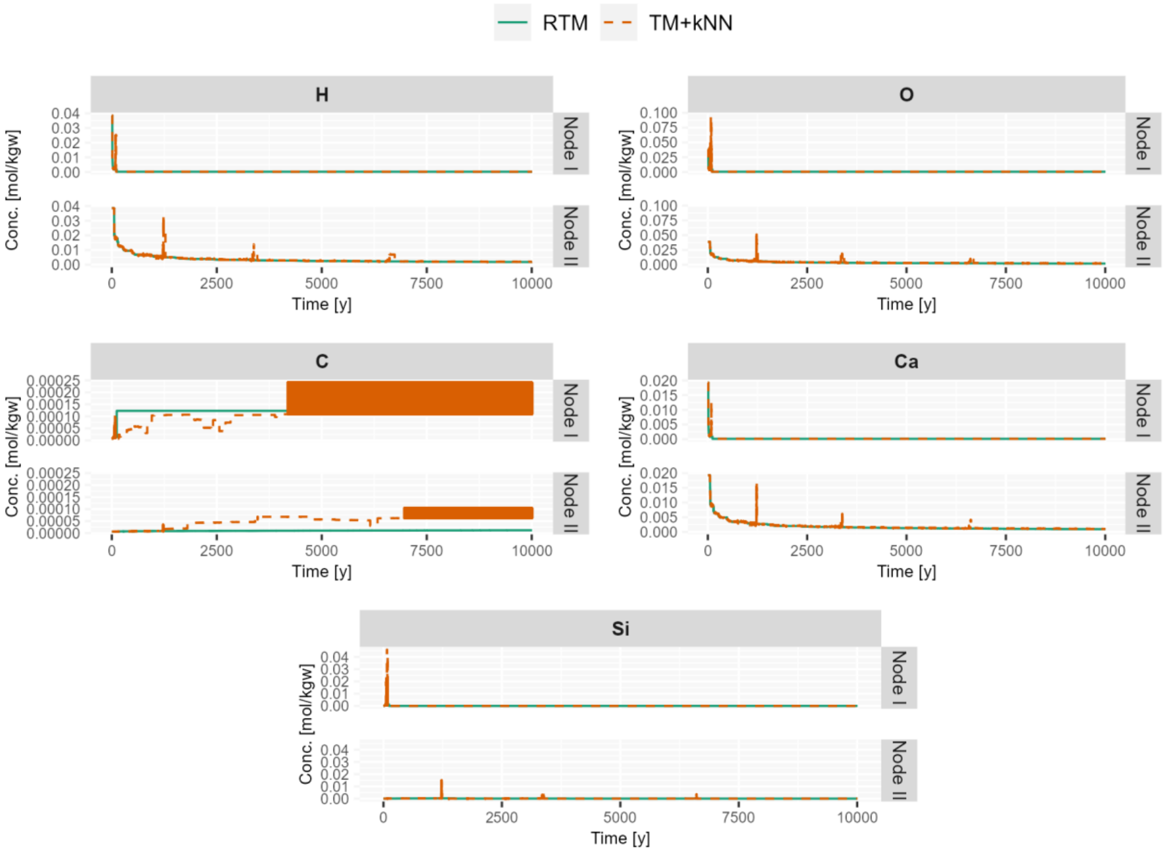

Figure 5-50 *Original (RTM) and DNN-accelerated (TM+kNN) RT simulated concentration time series at 2 (out of the considered 6) observation nodes for test case 2. The observation nodes I and II are the first two nodes of the one-dimensional grid and are respectively located at the surface and depth of 0.025 m in the vault backfill. The kNN training base was built using a Sobol low-discrepancy sequence of 1 x 10^5 training samples.*

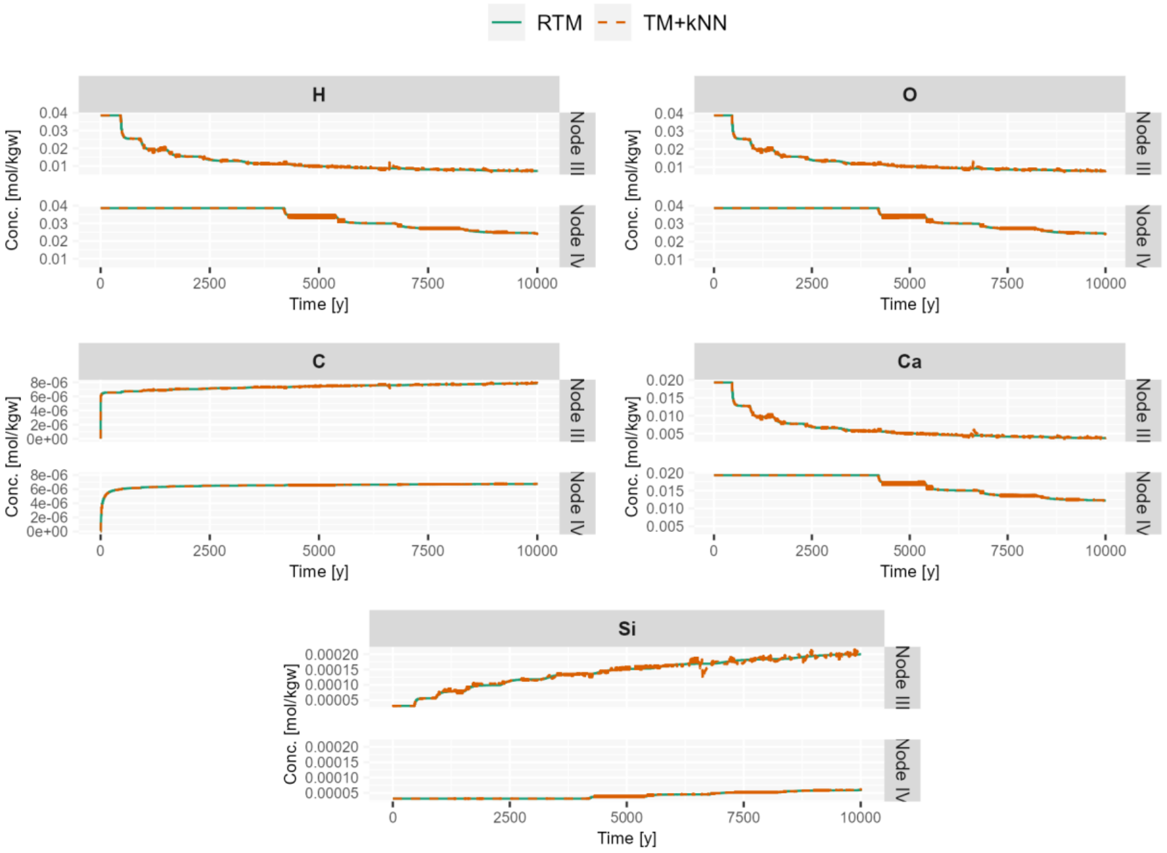

Figure 5-51 *Original (RTM) and kNN-accelerated (TM+kNN) RT simulated concentration time series at 2 (out of the considered 6) observation nodes for test case 2. The observation nodes III and IV are respectively located at depths of 0.1 m and 0.35 m in the vault backfill. The kNN training base was built using a Sobol low-discrepancy sequence of 1 x 10^5 training samples.*

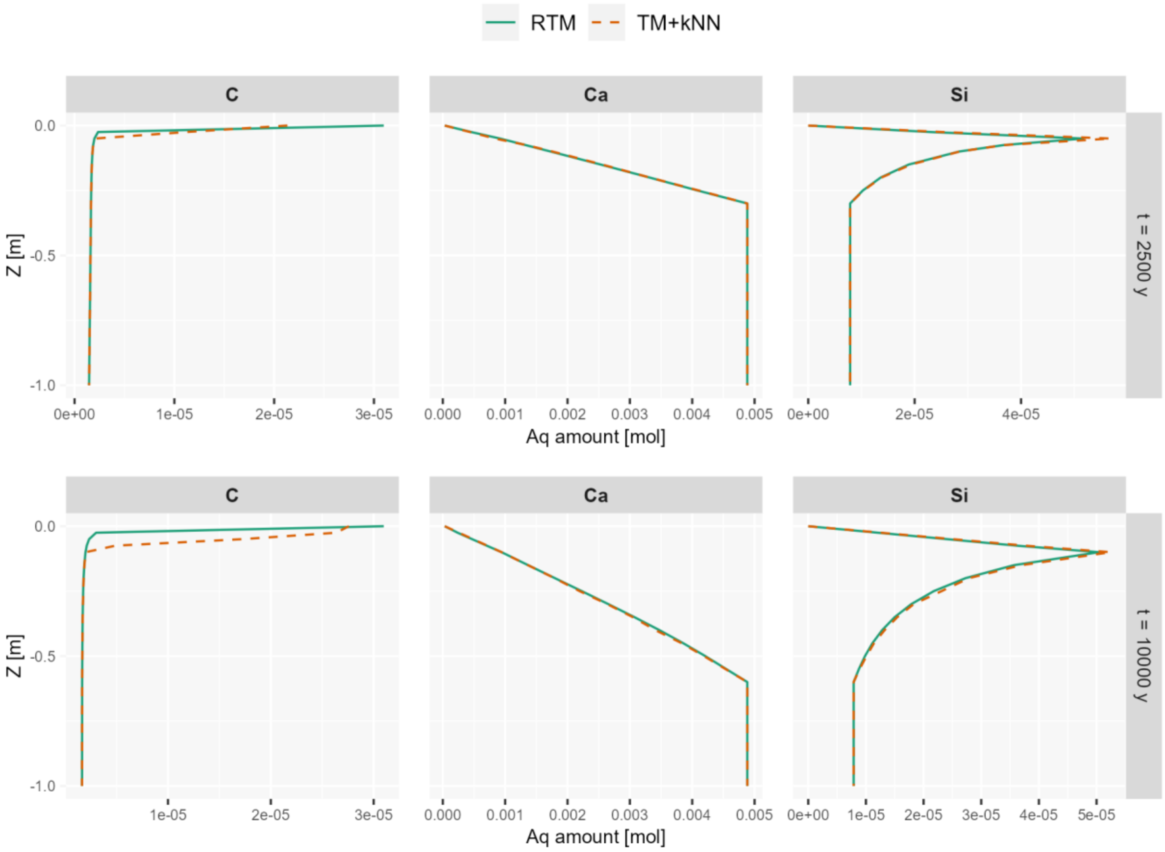

Figure 5-52 *Original (RTM) and kNN-accelerated (TM+kNN) RT simulations of the C, Ca and Si aqueous amount profiles after 2500 years and 10,000 years, for test case 2. The kNN training base was built using a Sobol low-discrepancy sequence of 1 x 10^5 training samples.*

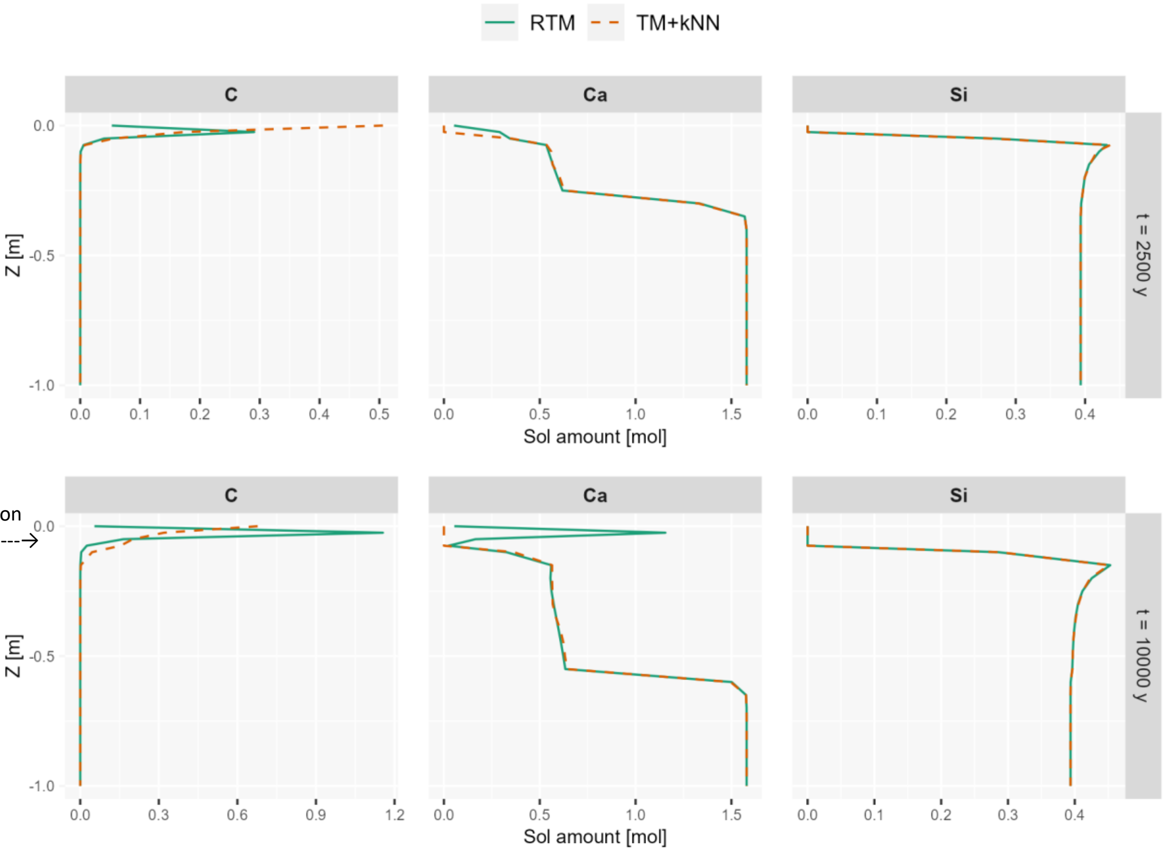

Calcite precipitation front (node II) -------→

Figure 5-53 *Original (RTM) and kNN-accelerated (TM+kNN) RT simulations of the C, Ca and Si solid amount profiles after 2500 years and 10,000 years, for test case 2. The kNN training base was built using using a Sobol low-discrepancy sequence of 1 x 10^5 training samples.*

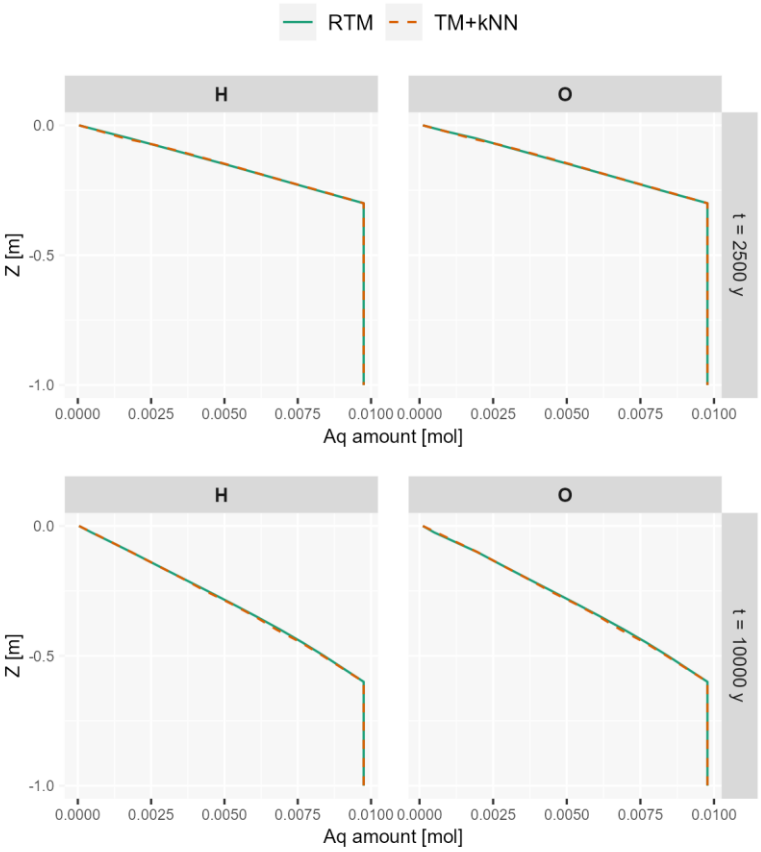

Figure 5-54 *Original (RTM) and kNN-accelerated (TM+kNN) RT simulations of the H and O aqueous amount profiles after 2500 years and 10,000 years, for test case 2. The kNN training base was built using using a Sobol low-discrepancy sequence of 1 x 10^5 training samples.*

5.4.7 Results for the C-Ca-Si-Al-Cl-K-Na-Mg-S problem – test case 3

This arguably complex case study is ongoing and at the time of writing this report, no mature results are ready to be shown. Yet we would like to stress the challenge of constructing a sufficiently informative training set for this test case. We did train for a DNN using a MC-based (again a Sobol low-discrepancy sequence) training set that comprises 2,000,000 training samples (TR2000k). It is observed that although the trained DNN performance evaluates against an independent MC-based test set may seem relatively good (green points in Figure 5-55), the actual DNN performance in an actual RT simulation is quite bad (blue points in Figure 5-55 and Figure 5-56). This highlights again the importance of deriving high-quality training samples.

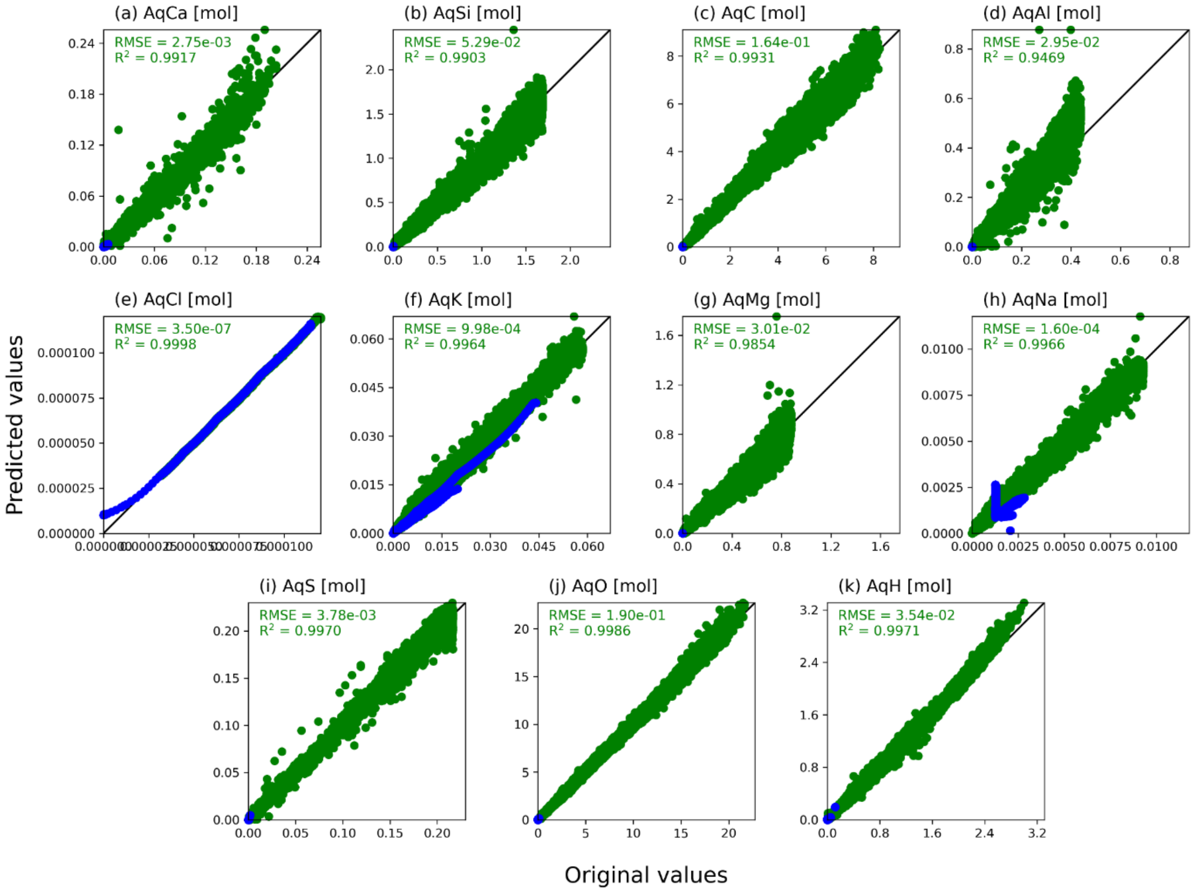

Figure 5-55 *Performance of the trained DNN (TR2000k MC-based training set) for an independent MC-based test set (green points) and in RT mode (blue points), for test case 3. Here the axes of the subplots span the range of the MC-based training and test datasets. The actual RT conditions (blue points) occupy a rather small fraction of this space.*

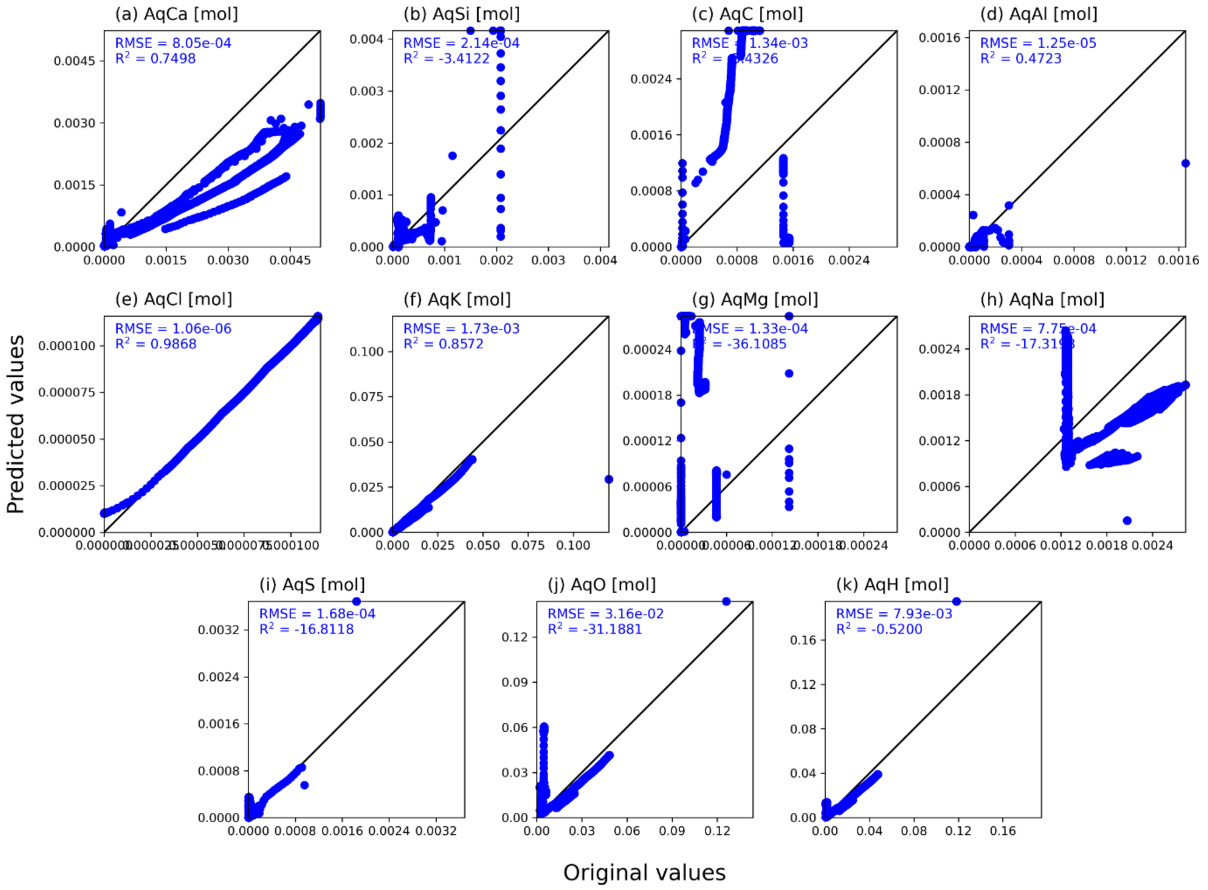

Figure 5-56 *Performance of the trained DNN (TR2000k MC-based training set) in RT mode (blue points) with a zoom on the actual RT conditions, for test case 3.*

5.4.8 Conclusion and Outlook

Results for our cement system [C,Ca,Si,O,H] (test case 2) show for the first time that DNN can substantially speed up reactive transport simulation in cement systems while accurately capturing both dissolution (portlandite and CSH) and precipitation (calcite). This when compared against the HPx code and for a relatively small computational grid of 112 nodes. We expect this gain to increase for larger grids. Nevertheless, it is important to note that not all geochemical solvers have the same speed. Therefore, it might be that the DNN-enabled speedup becomes significantly smaller, if not zero, compared to a reactive transport simulation performed by a RT code that relies on a faster geochemical solver than PHREEQC. The Orchestra geochemical solver (Meeussen, 2003), for instance, can become quite fast in RT mode thanks to its “warm initialization” strategy where the initial solution at a given node and time step consists of the final solution of the previous time step, when solving the geochemical equations (Meeussen, 2023). The speed gain offered by a DNN-based geochemical surrogate model when compared to a RT model of which the geochemical solver is equipped with such warm initialization remains to be explored. Our preliminary results for our cement system [C,Ca,Si,Al,Cl,K,Na,Mg,S,O,H] (test case 3) might be seen as showing the limits of offline training of black-box surrogate geochemical models for accelerating RT simulation in cement systems. We envision four potential way forwards. First, we will definitely thoroughly investigate the use of titration-based training set creation for this test case. Second, we will also verify whether creating the training set based on a “cheap” full RT simulation (coarser grid and shorter period) can be helpful (similarly as already proposed in Laloy and Jacques, 2022). Finding the right balance between computational effort and representativeness of this full RT simulation might not be an easy task though (if at all possible). Third, some physics constraints could be included in the (necessary) offline training of the DNN, such as in the physics-informed neural networks (PINNs) framework. This would however probably require modifications of the geochemical solver code such that derivatives of output quantities with respect to input quantities can be computed efficiently (for instance, using autodifferentiation). A final potentially interesting approach would be to implement an accept/reject mechanism of the kNN-predicted solution. In case of rejection a full geochemical calculation would be done and added to the kNN training base. This is possible because kNN does not require actual offline training. Defining this mechanism is however not straightforward. Future research effort will be devoted to these options.

6. References

Aguila, J.F., Samper, J., Mon, A., Montenegro, L., 2020. Dynamic update of flow and transport parameters in reactive transport simulations of radioactive waste repositories. Appl. Geochem. 117, 104585 https://doi.org/10.1016/j.apgeochem.2020.104585.

Alcorn, S. R., Christian-Frear, T. L. and Wallace, M. G. 1991. Degradation modelling for the concrete silo in TVO’s VLJ repository, Report, YJT-91-09.

Craeye, B., De Schutter, G., Van Humbeeck, H., Van Cotthem, A. (2009). Early age behaviour of concrete supercontainers for radioactive waste disposal. Nuclear Engineering and Design 239, 23–35.

Cybenko G. Approximations by superpositions of sigmoidal functions. Mathematics of Control, Signals, and Systems. 1989:2(4);303--314. https://doi.org/10.1007/BF02551274.

De Windt, L., Badreddine, R., Lagneau, V. (2007). Long-term reactive transport modelling of stabilised/solidified waste: from dynamic leaching tests to disposal scenarios. Journal of Hazardous Materials 139, 529-536.

De Windt, L., Samper, J., Cochepin, B., García, E., Mon, A., Montenegro, L., Samper, A., Veilly, E. (2023). Integrated reactive transport models for assessing the chemical evolution at the disposal cell scale, deliverable D2.17 of the HORIZON 2020 project EURAD. EC Grant agreement no: 847593.

ENRESA, 2000. Full-scale engineered barriers experiment for a deep geological repository in crystalline host rock FEBEX Project. In: EUR 19147 EN. European Commission.

Giffaut, E., Grivé, M., Blanc, P., Vieillard, P., Colàs, E., Gailhanou, H., Gaboreau, S., Marty, N., Madé, B., Duro, L. (2014). Andra thermodynamic database for performance assessment: ThermoChimie. Applied Geochemistry 49, 225–236.

Goodfellow, I., Bengio, Y., Courville, A. Deep learning. MIT Press; 2016. http://www.deeplearningbook.org.

Hastie, T. Tibshirani, R., Friedman, J. 2009. The Elements of Statistical Learning: Data Mining, Inference, and Prediction. Second edition. Springer. ISBN: 978-0-387-84858-7.

Hellä, P., Pitkänen, P., Löfman, J., Partamies, S., Vuorinen, U., Wersin, P. (2014). Safety case for the disposal of spent nuclear fuel at Olkiluoto - Definition of reference and bounding groundwater, buffer and backfill porewaters. Posiva Working report, 2014-04.

Höglund, L. O., Sidborn, M., Crawford, J., Keith-Roach, M. (2018). Modelling of Chemical Influences from Posiva’s Low and Intermediate Level Waste Repository on the Spent Nuclear Fuel Repository. Posiva working report, 2017-03.

Hornik K. Approximation capabilities of multilayer feedforward networks. Neural Networks. 1991:4(2), 251--257. https://doi.org/10.1016/0893-6080(91)90009-T.

Huang, Yonghui and Shao, Haibing and Wieland, Erich and Kolditz, Olaf and Kosakowski, Georg (2021), Two-phase transport in a cemented waste package considering spatio-temporal evolution of chemical conditions, npj Materials Degradation 5 1–4. https://doi.org/10.1038/s41529-021-00150-z

Jacques, D., Simunek, J. Mallants, D., van Genuchten., M.T. 2018. The HPx software for multicomponent reactive transport during variably-saturated flow: Recent developments and applications, Journal of Hydrology and Hydromechanics. 66(2), 211–226. https://doi.org/10.1515/johh2017-0049.

Johnson, J., Douze, M., Jégou, H. 2017. Billion-scale similarity search with GPUs. arXiv preprint arXiv:1702.08734.

Kingma, DP, Ba JL. Adam: a Method for Stochastic Optimization. The International Conference on Learning Representations (ICLR), San Diego; 2015. arXiv preprint arXiv: arXiv:1412.6980v9.

Kulik, D.A (2011). Improving the structural consistency of C-S-H solid solution thermodynamic models. Cement and Concrete Research 41, 477–495.

Kulik, D. A., Wagner, T., Dmytrieva, S. V., Kosakowski, G., Hingerl, F. F., Chudnenko, K. V., Berner, U. R. (2013). GEM-Selektor geochemical modeling package: revised algorithm and GEMS3K numerical kernel for coupled simulation codes. Computational Geosciences, 17(1), 1-24.

Laloy E, Jacques D (2022) Speeding Up Reactive Transport Simulations in Cement Systems by Surrogate Geochemical Modeling: Deep Neural Networks and k-Nearest Neighbors. Transp Porous Media 143:433–462. https://doi.org/10.1007/s11242-022-01779-3.

Lemieux, 2009. Monte Carlo and Quasi-Monte Carlo Sampling. Springer Series in Statistics. Springer-Verlag. https://doi.org/10.1007/978-0-387-78165-5.

Leupin, O., Zeyer, J., Cloet, V., Smith, P., Bernier-Latmani, R., Marschall, P., Papafotiou, A., Schwyn, B., Stroes-Gascoyne, S. (2016) An assessment of the possible fate of gas generated on a repository for low and intermediate level waste, Nagra Technical Report NTB 16-05, Nagra, Wettingen, Switzerland.

Lothenbach, B., D.A. Kulik, T. Matschei, M. Balonis, L. Baquerizo, B. Dilnesa, G. D. Miron, R.J. Myers, Cemdata18: a chemical thermodynamic database for hydrated Portland cements and alkali-activated materials, Cement Concr. Res. 115 (2019) 472–506, https://doi.org/10.1016/j.cemconres.2018.04.018.

Meeussen, J.C.L. 2003. ORCHESTRA: An object-oriented framework for implementing chemical equilibrium models Environmental science & technology 37 (6), 1175-1182.

Meeussen, J.C.L. 2023. Development and evaluation of a fast geochemical solver module for coupling with THMC models. Joint ACED/DONUT EURAD workshop - Assessing the long-term evolution of engineered barrier systems. of waste disposal systems. 2023/11/08. Mechelen, Belgium

Nagra (2016) Waste Management Programme of the Waste Producers. Nagra Technical Report NTB 16-01E, Nagra, Wettingen, Switzerland.

Parkhurst D. L., Kipp K. L., Charlton S. R. (2010). PHAST version 2: a program for simulating ground-water flow, solute transport, and multicomponent geochemical reactions. Techniques and Methods 6–A35, U.S. Geological Survey, Denver, Colorado.

Parkhurst, D.L., Appelo, C.A.J. (2013). Description of input and examples for PHREEQC version 3: a computer program for speciation, batch-reaction, one-dimensional transport, and inverse geochemical calculations: U.S. Geological Survey Techniques and Methods, book 6, chap. A43, 497 p.

Paszke, A., Gross, S., Chintala, S., Chanan, G., Yang, E., DeVito, Z., Lin, Z., Desmaison, A., Antiga, L., Lerer, A. Automatic differentiation in PyTorch. The Annual Conference on Neural Information Processing Systems 31 (NIPS), 2017.

Perko, J., Mayer, K.U., Kosakowski, G., De Windt, L., Govaerts, J., Jacques, D., Su, D., Meeussen J.C.L. (2015). Decalcification of cracked cement structures. Computational Geosciences 19, 673–693.

Prasianakis N, D Mašín, J Samper, K Černochová, A Gens, D Jacques, D Kulik, A Mon, L Montenegro, J Svoboda, C Tournassat, M V Villar, F Claret. 2023. Report describing the benchmarks to be carried out during the WP DONUT. Deliverable 4.4 of EURAD Joint Program. (available at Projectplace https://service.projectplace.com/#direct/document/3971065)

Prasianakis, N.I., E. Laloy, D. Jacques, J.C.L. Meeussen, C. Tournassat, G.D. Miron, D. A. Kulik, A. Idiart, E. Demirer, E. Coene, B. Cochepin, M. Leconte, M. Savino, J. Samper II, M. De Lucia, S. V. Churakov, O. Kolditz, C. Yang, J. Samper, F. Claret, 2024, Geochemistry and Machine Learning: review of methods and benchmarking, Environmental Geosciences (to be submitted).

Samper, J., Lu, C., Montenegro, L., 2008. Coupled hydrogeochemical calculations of the interactions of corrosion products and bentonite. Phys. Chem. Earth 33, S306–S316. https://doi.org/10.1016/j.pce.2008.10.009.

Samper, J., Naves, A., Montenegro, L., Mon, A., 2016. Reactive transport modelling of the long-term interactions of corrosion products and compacted bentonite in a HLW repository in granite: uncertainties and relevance for performance assessment. Appl. Geochem. 67, 42–51.

Samper, J., Montenegro, L., De Windt, L., Montoya, V., Garibay-Rodríguez, J., Grigaliuniene, D., Narkuniene, A., Poskas, P., (2021): Conceptual model formulation for a mechanistic based model implementing the initial SOTA knowledge (models and parameters) in existing numerical tools. Deliverable D2.16 of the HORIZON 2020 project EURAD. EC Grant agreement no: 847593.

Seetharam, S., Jacques, D. (2015). Potential Degradation Processes of the Cementitious EBS Components, their Potential Implications on Safety Functions and Conceptual Models for Quantitative Assessment, report OPERA-PU-SCK514, Netherlands.

Simunek, J., Sejna, M., Saito, H., Sakai, K., van Genuchten, M. T. 2013. The Hydrus-1D Software Package for Simulating the Movement of Water, Heat, and Multiple Solutes in Variably Saturated Media, Version 4.17. Department of Environmental Sciences, University of California Riverside, Riverside, California, USA.

Van der Lee, J., De Windt, L., Lagneau, Goblet, P., 2003. Module-oriented modeling of reactive transport with HYTEC. Computers and Geosciences 29, 265–275.

Vieno, T. and Nordman, H. 1991 VLJ-luolan turvallisuusanalyysi (Safety analysis of the VLJ repository), Report YJT-91-12. (in Finnish).

Wieland, E., Kosakowski, G., Lothenbach, B., Kulik, D. A., Cloet, V. (2018) Preliminary Assessment of the Temporal Evolution of Waste Packages in the near Field of the L/ILW Repository, Nagra Arbeitsbericht NAB 18-05, Nagra, Wettingen, Switzerland.

Wieland, E., Kosakowski, G., Lothenbach, B., Kulik, D. A. (2020) Geochemical modelling of the effect of waste degradation processes on the long-term performance of waste forms. 115, 104539 https://doi.org/10.1016/j.apgeochem

Appendix A. Definition of the metrics used in Section 2.4

This appendix presents the definition of the metrics used in Section 2.4 for quantifying the predictions of the metamodel. These metrics were used taken from Prasianakis et al. (2023; 2024) who used them for benchmarking machine learning methods for two chemical systems.

MAE is the Mean Absolute Error which is defined as

$$MAE = \frac{1}{N}\sum_{i=1}^{N}|y_i - \hat{y}_i|$$

where N is the number of samples, y_i is the true value and $\hat{y}_i$ is the ML model prediction. Similarly, MSE is the Mean Square Error, defined as

$$MSE = \frac{1}{N}\sum_{i=1}^{N}(y_i - \hat{y}_i)^2$$

The Root Mean Square Error RMSE is the square root of MSE. The coefficient of determination R^2 is given by:

$$R^2 = 1 - \frac{\sum_{i=1}^{N}(y_i - \hat{y}_i)^2}{\sum_{i=1}^{N}(y_i - \bar{y})^2}$$

where $\bar{y}$ is the mean value of the true values. Normalized metrics include the Normalized Mean Absolute error NMAE:

$$NMAE = \frac{1}{N}\sum_{i=1}^{N}\frac{|y_i - \hat{y}_i|}{y_{max} - y_{min}}$$

where y_{max} and y_{min} are the maximum and minimum values of the true data. The Normalized Root Mean Square Error NRMSE is given by

$$NRMSE = \frac{RMSE}{y_{max} - y_{min}}$$

The Normalized sup norm Normsupnorm is given by:

$$Normsupnorm = \max_{1 \le i \le N}\frac{|y_i - \hat{y}_i|}{y_{max} - y_{min}}$$

Many geochemical variables are lognormally distributed. For this reason, the metrics are also defined in terms of logarithms of the variables. MAElog and RMSElog are metrics similar to the MAE and RMSE. If both the true and the predicted values are greater than 0, then MAElog and RMSElog are given by:

$$MAElog = \frac{1}{N}\sum_{i=1}^{N}|\log y_i - \log \hat{y}_i| = \frac{1}{N}\sum_{i=1}^{N}\left|\log\frac{y_i}{\hat{y}_i}\right|$$

$$RMSElog = \sqrt{\frac{1}{N}\sum_{i=1}^{N}(\log y_i - \log \hat{y}_i)^2} = \sqrt{\frac{1}{N}\sum_{i=1}^{N}\left(\log\frac{y_i}{\hat{y}_i}\right)^2}$$

RMSLE is the Root Mean Square Logarithmic Error defined as:

$$RMSELE = \sqrt{\frac{1}{N}\sum_{i=1}^{N}(\log(y_i+1)-\log(\hat{y}_i+1))^2} = \sqrt{\frac{1}{N}\sum_{i=1}^{N}\left(\log\frac{y_i+1}{\hat{y}_i+1}\right)^2}$$

It should be noticed that MAE_{log} is the geometric mean of the absolute values of the quotients GMAQ (Geometric Mean of Absolute Quotients) of y and $\hat{y}$:

$$GMAQ = \left(\prod_{i=1}^{N}\frac{\hat{y}_i}{y_i}\right)^{\frac{1}{N}}$$

Instead of the simple quotient of the true and predicted values y and $\hat{y}$, one can define a relative error α_i as:

$$\alpha_i = \begin{cases} \frac{y_i - \hat{y}_i}{y_i} & \text{if } y_i, \hat{y}_i \neq 0 \\ 1 & \text{if } y_i = 0 \text{ and } \hat{y}_i \neq 0 \\ 0 & \text{if } y_i = 0 \text{ and } \hat{y}_i = 0 \end{cases}$$

The Mean Absolute Percentage Error MAPE and the Relative RMSE (RRMSE) are given by:

$$\text{MAPE} = \frac{100\%}{N}\sum|\alpha_i|$$

$$\text{RRMSE} = \sqrt{\frac{1}{N}\sum(\alpha_i)^2}$$

It should be noticed that MAPE and RRMSE might not be appropriate for the estimate of accuracy for minerals that take zero values (Prasianakis et al., 2024).